

AD-A271 734



①

# GPS Based Spacecraft Attitude Determination

Final Report for  
October 1992- September 1993

to the Naval Research Laboratory



Prepared by

Penina Axelrad  
Bruce C. Chesley  
Lisa M. Ward

September 30, 1993

Co-Principal Investigators - Penina Axelrad  
George H. Born  
Peter F. MacDoran

Colorado Center for Astrodynamics Research  
University of Colorado, CB 431  
Boulder, CO 80309

This document has been approved  
for public release and sale; its  
distribution is unlimited

93-25468



82 PG

93 10 21 065

## Table of Contents

Abstract .....	1
1. Background .....	2
2. Objectives and Benefits .....	4
3. GPS Attitude Determination Overview .....	5
3.1 GPS Signal and Observables.....	5
3.2 Relating Observables to Attitude .....	6
3.3 Reference Frames.....	6
3.4 Attitude Solution Methods .....	7
4. Spacecraft Attitude and Orbit Determination .....	8
4.1 Orbit Dynamics .....	8
4.2 GPS Orbit Observations.....	9
4.3 Attitude Kinematics .....	10
4.4 Attitude Dynamics .....	12
4.5 GPS Attitude Observations .....	14
4.6 Attitude Point Solution Methods.....	16
4.7 Attitude Filters .....	21
4.8 Navigation Filter .....	24
4.9 Simulation .....	25
4.10 Results and Discussion.....	28
5. Algorithms and Ground Testing .....	41
5.1 Attitude Receiver Comparison.....	41
5.2 Least Squares Solution.....	43
5.3 Baseline Survey.....	45
5.4 Integer Ambiguity Resolution.....	47
5.5 Ground Testing Configuration .....	49
5.6 Phase Measurement Quality.....	54
5.7 Baseline Survey Test.....	64
5.8 Relative Pitch Accuracy Test.....	66
5.9 Absolute Heading Accuracy Test .....	67
5.10 Degraded Test Structure.....	70
5.11 Dynamic Tests.....	72
6. Future Work .....	73
References.....	75
Appendices.....	78
A. Calculating a Transformation Matrix from Quaternions and Euler angles.....	78
B. Dynamics Matrices.....	79

Accession For	
NWIS - ORAD	<input checked="" type="checkbox"/>
Diss. Fee	<input type="checkbox"/>
Unpublished	<input type="checkbox"/>
Justification .....	
By .....	
Distribution/ .....	
Availability codes	
Dist A-	Avail and/or Special

## Abstract

This report summarizes the FY'92-93 research activity at the Colorado Center for Astrodynamics Research (CCAR) on the application of GPS based attitude determination techniques to near-Earth spacecraft. The areas addressed include solution algorithms, simulation of the spacecraft and environment, and ground testing of a state-of-the-art attitude receiver.

The simulation includes models of a gravity gradient stabilized gyrostat in a near-Earth,  $J_2$  perturbed orbit. GPS pseudorange measurements for navigation, and phase difference measurements for attitude determination, were modeled including error sources such as Selective Availability (SA) and multipath. A Kalman Filter was designed to estimate the position and velocity of the vehicle in an Earth Centered Inertial coordinate frame. With the simplified models used, positioning accuracy was found to be about 2 meters RMS without SA and 30 m RMS when SA was included. For attitude determination, the antenna baselines were considered to be 1 meter long in an optimal orthogonal configuration. The nominal performance of the point (or instantaneous) attitude solution was found to be 0.1 deg RMS. A linearized Kalman Filter algorithm parameterized by Euler angles produced better performance at the level of 0.03 deg RMS. An extended Kalman filter implemented using a quaternion state representation gave comparable performance when the spacecraft was within 1 degree of local level, and unlike the Euler angle version, was able to perform equally well in other spacecraft orientations. The slowly varying multipath errors had a severe effect on the filtered solutions, degrading the accuracy to the level of about 0.1 deg RMS.

Ground experiments were performed with a state-of-the-art GPS attitude receiver, the Vector, manufactured by Trimble Navigation. This receiver has six parallel hardware channels, which multiplex among four antennas (1 master and 3 slaves) to produce absolute range measurements to the master and differential phase measurements between the master and each of the slaves. The antennas were mounted to one of four test structures to evaluate the measurement quality and the attitude determination performance. The differential phase precision was found to range from better than 2 mm  $1-\sigma$  to as much as 1 cm  $1-\sigma$  in a particularly noisy multipath environment. The Vector implements a least squares algorithm which solves for vehicle pitch, roll, and heading angles. The solution performance was evaluated in static tests with the structure aligned in a known orientation. The pointing accuracy was found to be 0.2 deg for a 1 m baseline structure. We also investigated an off-line self-survey algorithm which establishes the baseline vectors in the body fixed frame and determines the antenna/receiver line biases.

The next step in this project is to test the algorithms on some experimental data which we recently received, collected from the Air Force RADCAL satellite. In the future we hope to further validate and improve our algorithms with other on-orbit data to improve performance, reliability, and robustness under varying conditions. Our plans for future ground test are also geared toward these goals.

## 1. Background

GPS is currently being described as an "all-purpose" sensor for aircraft and spacecraft applications. The navigation performance of GPS has been widely demonstrated on land, marine, and airborne vehicles, and to a limited degree on near-Earth spacecraft. More conventional spacecraft attitude sensors include conical Earth scanners, magnetometers, sun sensors, attitude reference units (ARU), and star trackers. The highest performance is obtained through a combination of star tracker and ARU, providing attitude determination accuracy better than 0.01 degrees, 3- $\sigma$  [Levenson, et al., 1992]. Horizon sensors are more coarse, with accuracies at the level of 0.05-0.1 degrees [Larson and Wertz, 1992]. Instantaneous GPS solution accuracy is expected to be in the range of 0.1-0.5 degrees, depending on the vehicle configuration. With dynamic modeling and measurement filtering, further improvement is expected.

In the last two years, several near Earth spacecraft have been launched which make use of GPS in some capacity. TOPEX/Poseidon is a joint project between the U.S. and France to study the dynamics of the Earth's oceans. The primary instruments are two altimeters designed to measure the height of the spacecraft above the ocean surface. In addition, TOPEX carries a 6 channel Motorola GPS Demonstration Receiver (GPSDR). This is a dual frequency P-code and carrier tracking receiver. Crude position solutions are available on board the satellite; however, the primary function of the receiver is to collect raw data for orbit post processing by the Jet Propulsion Laboratory (JPL). A recent paper by Bertiger, et al. [1993] describes the orbit accuracies of 3 cm RMS radial and 10 cm along track and cross track which are currently being achieved using the TOPEX data together with a network of ground based GPS receivers.

The Extreme Ultraviolet Explorer (EUVE) is also currently operating an experimental receiver in a 500 km altitude orbit. The EUVE receiver is the engineering prototype of the one to be flown on TOPEX. Gold, et al. [1993] recently reported on orbit determination results generated using GIPSY-OASIS II in both post-processed mode (with ground station augmentation) and in a pseudo real time mode. Unlike the TOPEX receiver, the EUVE version only tracks L1 C/A code and carrier signals. Six satellites are tracked at a time from one of two antennas mounted to the spacecraft body. Their results showed potential for on board performance at the several meter level even in the presence of Selective Availability.

We are aware of only two tests of both orbit and attitude determination on orbit. The US Air Force RADCAL satellite is currently flying a Trimble Quadrex receiver which collects differential phase data from four antennas. Initial attitude solutions have been reported by Cohen and Lightsey [1993]. They have had some difficulty in processing the solutions because of unreliable ground calibration of the baselines and the severe multipath environment on this spacecraft. However, they are continuing to work with

this data.<sup>1</sup> An additional test with the Trimble Quadrex was recently performed on Shuttle Flight STS-51 [Saunders, 1993]. The receiver and four antennas were carried in the crew compartment and attached to the orbiter forward window panels. Results from this experiment are also expected within the next several months.

Many upcoming satellite missions have plans to employ GPS for orbit and in some cases attitude determination, including Gravity Probe B [Axelrad and Parkinson, 1989], Seastar, Hermes Columbus [Munjal, et al., 1992], the U.S. Space Shuttle [Madden, 1992], and the Orbital Sciences mobile communications satellites, Orbcomm.

The use of GPS for attitude determination on land, sea, and air is somewhat further developed. There are currently several commercially available attitude determination receivers (or systems of receivers) including those made by Trimble [Cohen, 1992; Trimble 1992], Texas Instruments [Brown, 1990], Ashtech [Ferguson, 1991], and Adroit Systems [Diefes, 1993]. Many of these were reported on or demonstrated at the ION GPS-93 Meeting held in Salt Lake City, September 22-24, 1993.

GPS attitude determination systems have grown out of the successes of GPS kinematic survey, wherein carrier interferometry is used over baselines of 10 km or more to precisely determine baseline vectors from a reference site to some type of mobile surveyor on land, sea, or air. Kinematic survey has the potential to achieve accuracies of better than 10 cm; however, it is limited by multipath and range decorrelation effects of the ionosphere, troposphere, and satellite orbit errors. The fundamental observation for kinematic survey is a double difference of carrier measurements made by the two receivers to two satellites. The double difference eliminates both satellite specific errors and receiver clock errors. However, in order to use these observations, an integer wavelength ambiguity must be solved for each satellite pair. This generally requires extra satellites and sometimes may take tens of minutes to complete.

In several ways, attitude determination is simpler than kinematic survey. First, in some attitude receivers, a common oscillator is used to make the measurements on all antennas, thus, there is no need to difference between satellites to remove the receiver clock error. This reduces the number of measurements required to form a solution. Second, the ambiguity resolution problem is made easier because the baseline lengths and relative orientations in the body frame are fixed and known. The baselines are also shorter, thus limiting the number of possible carrier cycle ambiguities which must be considered. Finally, the small separation between the antennas effectively eliminates concerns about ionospheric and tropospheric range decorrelation. The remaining accuracy limitations are multipath reflections, antenna phase center migration, antenna crosstalk, and structural flexure.

---

<sup>1</sup> Glenn Lightsey has provided us with what he believes is the best 5 hour data set from RADCAL. We will begin work on this within the next several weeks.

## 2. Objectives and Benefits

The goal of our work is to develop algorithms and investigate the potential for GPS based attitude determination in near-Earth spacecraft applications. Past and current work indicates that GPS has tremendous potential for providing real time orbit and attitude information directly to the vehicle. This is of interest for two reasons - this data is required to both interpret data from on board sensors, and as feedback to a control system to achieve the desired spacecraft orbit and orientation. Before GPS can be used "in-the-loop", accuracy, reliability, and robustness of the onboard solutions must be further investigated and improved.

The first year's efforts on this project were focused on establishing a reliable simulation of the near-Earth attitude determination performance and conducting ground experiments for evaluation of the basic performance of GPS. The algorithms derived in both the ground tests and simulations will soon be put to an important test in processing data collected on orbit from the RADCAL mission.

In the simulation area, it was our objective to set up and validate a computer model of the spacecraft environment including both navigation and attitude determination functions. We would then implement and compare various algorithms, both single point and filtered solutions, for real time attitude determination. The simulation results have shown the type of performance that was expected under nominal conditions and with measurements corrupted by Selective Availability (for navigation) and multipath. In particular, we implemented a quaternion based estimation filter which is able to perform under a wide range of spacecraft configurations.

In the test area, we wanted to gain experience with state-of-the-art GPS attitude determination hardware and real time solution algorithms, and to characterize both measurement and solution quality. This is an important step towards being able to process GPS measurements in real time on orbit.

We hope that this work will provide important information for designing attitude determination and control systems for future Navy satellite missions. We expect to be able to suggest improvements and enhancements of the GPS based algorithms which should lead to more accurate, reliable, and robust on-orbit performance.

The following section reviews the theory of GPS based attitude determination. Section 4 describes the models of the spacecraft dynamics, estimation algorithms, and simulated performance. Section 5 covers the algorithms used for ground testing and the experimental results. Section 6 concludes the report with a discussion of our plans for future work.

### 3. GPS Attitude Determination Overview

Lisa M. Ward

GPS based attitude determination is based on observations of the differential phase between carrier signals received at two or more antennas. This section discusses the observable quantities, how they are obtained from GPS receivers, and gives an overview of several attitude solution methods.

#### 3.1 GPS Signal and Observables

The GPS signal of interest for this study is the L1 frequency centered on 1575.42 MHz. Each GPS satellite modulates this carrier with a unique pseudo-random noise code known as the C/A code, at 1.023 MHz chipping rate. The C/A code identifies the satellite, and enables the receiver to measure the transit time of the signal from the satellite to the receiver. This observed range based on transit time, known as pseudorange, is used to solve for the position of the observer [c.f. Milliken and Zoller, 1980].

The principal observable for GPS attitude determination is the carrier phase difference between a master antenna and one or more slave antennas. Figure 3.1 shows the incident carrier wave received by a single master and slave antenna pair. The difference in the received phase,  $\Delta\phi$ , between the master and the slave is the actual measurement observable. The phase difference,  $\Delta\phi$ , is related to the range difference,  $\Delta r$ , (both expressed in cycles) as follows,

$$\Delta r = \Delta\phi + k - \beta + \nu \quad (3.1)$$

where  $k$  is the integer number of carrier cycles in the differential range,  $\beta$  is the constant fractional cycle hardware delay between the two antennas, and  $\nu$  is the random measurement noise.

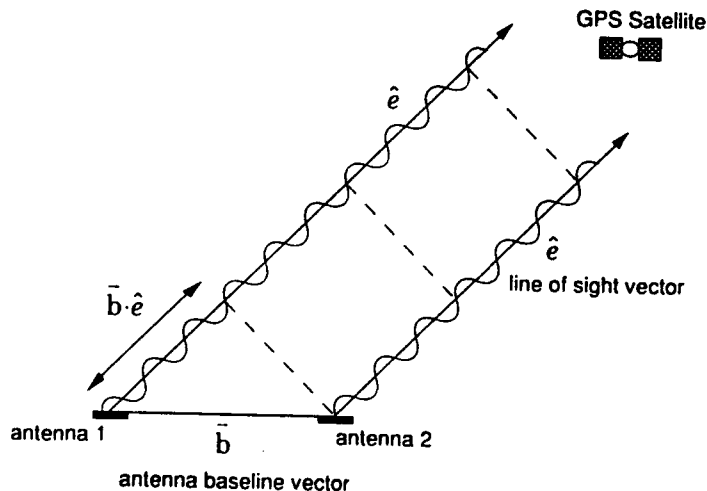


Figure 3.1 GPS Differential Phase Geometry

### 3.2 Relating Observables to Attitude

As can be seen in Figure 3.1, the range difference is just the projection of the baseline vector,  $\mathbf{b}$  (directed from the master to the slave), onto the user-to-GPS line of sight vector,  $\mathbf{e}$ , which gives

$$\Delta r = \mathbf{b} \cdot \mathbf{e}. \quad (3.2)$$

If we assume that baseline vector is known in the vehicle or body fixed frame, and the line of sight vector is known in an inertial (or Earth Fixed) reference frame, the differential range can be written as a function of the inertial to body transformation matrix  ${}^B C^I$ , as follows,

$$\Delta r = (\mathbf{b}^B)^T {}^B C^I \mathbf{e}^I \quad (3.3)$$

One representation of the attitude is the transformation matrix  ${}^B C^I$  between the I and B frames.

### 3.3 Reference Frames

For this study three reference frames are defined as shown in Figure 3.2. The first is the inertial frame, I. Here,  $\mathbf{k}^I$  is aligned with the spin axis of the Earth,  $\mathbf{i}^I$  is in the equatorial plane and points toward the first point of Aries, and  $\mathbf{j}^I$ , also in the equatorial plane is perpendicular to  $\mathbf{i}^I$ . The next frame is the orbit local frame, L. The  $\mathbf{i}^L$  vector points in the satellite zenith or radial direction,  $\mathbf{k}^L$  is aligned with the angular momentum vector of the satellite, and  $\mathbf{j}^L = \mathbf{k}^L \times \mathbf{i}^L$  completing the orthogonal set. Finally, the body frame, B, axes coincide with the principal axes of the satellite, and are nominally aligned with the local frame.

The transformation matrix  ${}^L C^I$  which describes the rotation from the inertial to the local frame is derived from the satellite position. The  ${}^B C^L$  transformation matrix describing the rotation from the local to the body frame is derived from the Euler angles: yaw, roll, and pitch. Here pitch is the first rotation about the  $\mathbf{k}^B$ -axis, roll is the second rotation about the  $\mathbf{j}^B$ -axis, and yaw is the third rotation about the  $\mathbf{i}^B$ -axis. The total rotation from the inertial to the body frame is described by the transformation matrix  ${}^B C^I = {}^B C^L {}^L C^I$ . Instead of using Euler angles or a transformation matrix, quaternions can also be used to describe the rotation from between frames. The relationship between these three attitude representations can be found in Appendix A.

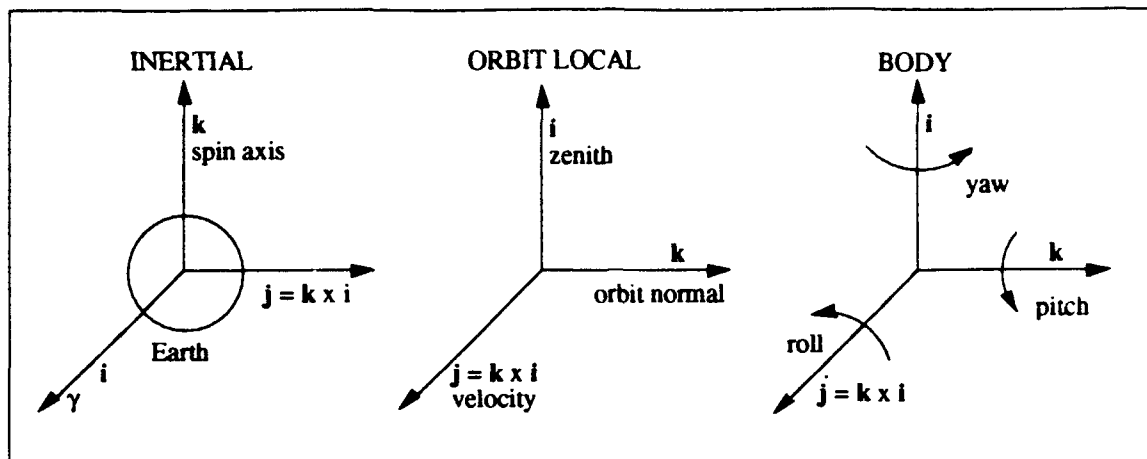


Figure 3.2 Inertial, Orbit Local, and Body Fixed Reference Frames

### 3.4 Attitude Solution Methods

Deterministic attitude determination is possible given a minimum number of observations, for example 3 baselines observing 2 satellites. However, there are usually more measurements available enabling us to optimize the solution in some way. An iterative nonlinear least squares method is one possibility. Markley [1988] describes a fast least squares method using singular value decomposition to find the optimal attitude matrix. Kalman filters are yet another way to solve for attitude by incorporating information about the dynamics into the least squares process. An in depth discussion of these methods will be presented in Section 4.

## 4. Spacecraft Attitude and Orbit Determination

Lisa M. Ward

A simulation was developed to evaluate the performance of the various attitude solution methods using GPS. The true user satellite orbit and attitude dynamics are modeled as well as the orbit dynamics of the GPS satellites. Measurements observed by the GPS receiver are constructed. The position and velocity of the user are estimated with the navigation model. Finally, the attitude of the vehicle is estimated using one of the solution methods. A description of the simulation models and algorithms are presented in Sections 4.1-4.8. Section 4.9 provides specifics on the computer simulation, and 4.10 discusses the various cases considered and the results obtained. The FORTRAN code implementing the simulation is available upon request.

### 4.1 Orbit Dynamics

In this work, the primary interest is in attitude determination; however, since the orbit local frame as well as the gravity gradient torque depend on the position of the satellite, a model of the orbital dynamics must be included as well. A two-body orbit with oblate Earth perturbations was selected to describe the true motion of the user satellite. These equations of motion are,

$$\begin{aligned}\ddot{x} &= \frac{-\mu x}{r^3} \left[ 1 - \frac{3}{2} J_2 \left( \frac{R_e}{r} \right)^2 \left( 5 \frac{z^2}{r^2} - 1 \right) \right] \\ \ddot{y} &= \frac{-\mu y}{r^3} \left[ 1 - \frac{3}{2} J_2 \left( \frac{R_e}{r} \right)^2 \left( 5 \frac{z^2}{r^2} - 1 \right) \right] \\ \ddot{z} &= \frac{-\mu z}{r^3} \left[ 1 - \frac{3}{2} J_2 \left( \frac{R_e}{r} \right)^2 \left( 5 \frac{z^2}{r^2} - 3 \right) \right]\end{aligned}\tag{4.1}$$

where  $r = \sqrt{x^2 + y^2 + z^2}$

and where  $x$ ,  $y$ , and  $z$  are the satellite position coordinates,  $\mu$  is the Earth's gravitational constant,  $J_2$  is the Earth's 2nd zonal harmonic coefficient, and  $R_e$  is the radius of the Earth. The position and velocity of the user satellite are calculated by numerically integrating Equations 4.1.

The position and velocity of the GPS satellites are calculated analytically using a simpler model which includes only two-body effects. The orbital elements for the 24 satellite "primary" satellite constellation reported by Green, et al. [1989] were used.

## 4.2 GPS Orbit Observations

Once the positions of the user and GPS satellite are established, the distance,  $D$ , between them can be computed. The quantity that is actually measured by a GPS receiver is the pseudorange,  $\rho$ . The pseudorange is equal to the distance plus clock bias and noise errors due to the receiver ( $b_R$  and  $v_\rho$ ), bias errors due the satellite ( $-b_S$ ), delay through the ionosphere ( $\epsilon_I$ ), and Selective Availability ( $s$ ), as follows,

$$D = \sqrt{(x_{gps} - x)^2 + (y_{gps} - y)^2 + (z_{gps} - z)^2} \quad (4.2)$$

$$\rho = D + b_R - b_S + \epsilon_I + s + v_\rho$$

where  $x_{gps}$ ,  $y_{gps}$ , and  $z_{gps}$  are the position coordinates of the GPS satellite. The receiver clock bias is not modeled in our work. Normally it is solved for in the navigation filter and does not affect the performance. We also ignored the bias errors due to the satellite clock, orbit, and ionosphere.

Similarly, the range rate,  $\dot{D}$ , can be computed as projection of the relative velocity onto the line of sight.  $\dot{D}$  and the related pseudorange rate,  $\dot{\rho}$ , are given by,

$$\dot{D} = \left[ (\dot{x}_{gps} - \dot{x})(x_{gps} - x) + (\dot{y}_{gps} - \dot{y})(y_{gps} - y) + (\dot{z}_{gps} - \dot{z})(z_{gps} - z) \right] / D \quad (4.3)$$

$$\dot{\rho} = \dot{D} + f_R - f_S + \dot{s} + v_{\dot{\rho}}$$

where the receiver clock drift ( $f_R$ ) and satellite clock drift ( $f_S$ ) will be ignored.

As a simple approximation, the measurement errors for both the range ( $v_\rho$ ) and range rate ( $v_{\dot{\rho}}$ ) were modeled as Gaussian processes with zero mean and standard deviations  $\sigma_\rho$  and  $\sigma_{\dot{\rho}}$ , respectively.

This type of modeling, however, does not account for Selective Availability (SA). Since SA is the largest error source for non-differential users it is important to include this effect. A second order ARIMA model described by Lear [1992] is used to more accurately describe the range measurement noise. For each GPS satellite a selective availability error is generated using

$$s_k = a_1 s_{k-1} + a_2 s_{k-2} + b_1 w_k + b_2 w_{k-1} \quad (4.4)$$

where  $s_k$  is the measurement error due to selective availability at time  $t_k$  and  $w_k$  is the white noise (with zero mean and unity standard deviation) at time  $t_k$ .  $a_i$  and  $b_i$  are the model coefficients for a 1 second time interval and are given by

$$\begin{aligned}
 a_1 &= 1.993960846 \\
 a_2 &= -0.9940230677 \\
 b_1 &= 0.998209455 \\
 b_2 &= -0.974835034
 \end{aligned}
 \tag{4.5}$$

Figure 4.2 shows a plot of the typical selective availability for one GPS satellite.

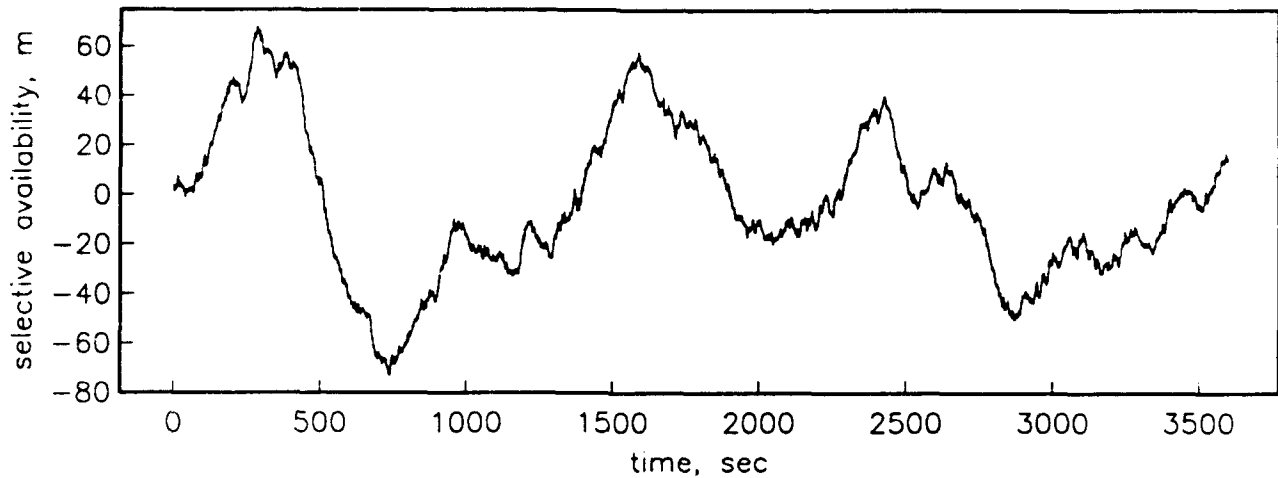


Figure 4.2. Example of Selective Availability

The corresponding range rate measurement noise,  $\dot{s}_k$ , is computed by approximating the derivative of the selective availability with

$$\dot{s}_k = (s_k - s_{k-1}) / \Delta t
 \tag{4.6}$$

where  $\Delta t$  is time interval between measurements.

### 4.3 Attitude Kinematics

The time derivative of the inertial to body attitude matrix defines the inertial angular velocity vector of the body,  $\omega$ .

$${}^B\dot{C}^I = \omega^\times {}^B C^I
 \tag{4.7}$$

where  $\omega^\times$  is the cross product matrix,

$$\omega^x = \begin{bmatrix} 0 & \omega_3 & -\omega_2 \\ -\omega_3 & 0 & \omega_1 \\ \omega_2 & -\omega_1 & 0 \end{bmatrix} \quad (4.8)$$

and where  $\omega = \omega_1 \mathbf{i}^B + \omega_2 \mathbf{j}^B + \omega_3 \mathbf{k}^B$ .

Rewriting this equation in terms of Euler angles where  $\theta_3$  is the first rotation about 3-axis,  $\theta_2$  is the second rotation about the 2-axis, and  $\theta_1$  is the third rotation about the 1-axis gives

$$\begin{aligned} \dot{\theta}_1 &= \omega_1 + (\omega_2 \sin \theta_1 + \omega_3 \cos \theta_1) \tan \theta_2 \\ \dot{\theta}_2 &= \omega_2 \cos \theta_1 - \omega_3 \sin \theta_1 \\ \dot{\theta}_3 &= (\omega_2 \sin \theta_1 + \omega_3 \cos \theta_1) / \cos \theta_2. \end{aligned} \quad (4.9)$$

To formulate these equations in terms of yaw, roll, and pitch which characterize the local to body rotation, the orbital motion of the satellite must be removed. This is done as shown in Melvin [1991] by setting  $\theta_1$  equal to yaw,  $\theta_2$  equal to roll, and  $\theta_3$  equal to pitch plus the argument of latitude,  $u$ .

In addition to matrices and Euler angles, quaternions can also be used describe the attitude of a body. Recall that the quaternion  $\mathbf{q}$  is defined as

$$\mathbf{q} = \begin{bmatrix} q_1 \\ q_2 \\ q_3 \\ q_4 \end{bmatrix} \quad (4.10)$$

where  $\bar{q} = \begin{bmatrix} q_1 \\ q_2 \\ q_3 \end{bmatrix} = \hat{\lambda} \sin\left(\frac{\alpha}{2}\right)$  and  $q_4 = \cos\left(\frac{\alpha}{2}\right)$ .

$\alpha$  is the rotation angle about the axis of rotation  $\hat{\lambda}$ . The rate of change of the quaternion is given by

$$\dot{\mathbf{q}} = \frac{1}{2} \mathbf{Q} \omega \quad (4.11)$$

where 
$$\mathbf{Q} = \begin{bmatrix} q_4 & -q_3 & q_2 \\ q_3 & q_4 & -q_1 \\ -q_2 & q_1 & q_4 \\ -q_1 & -q_2 & -q_3 \end{bmatrix}.$$

In order for  $\mathbf{q}$  to represent the local to body rotation, the  $\omega$  vector in Equation 4.11 must be the angular velocity of the body with respect to the local frame,  ${}_B\omega_L$ . Since generally the inertial angular velocity  ${}_B\omega_I$  is needed for the dynamical equations below, the angular velocity of the of the local frame in inertial space  ${}_L\omega_I$  must be removed as follows:

$${}_B\omega_L^B = {}_B\omega_I^B - {}_L\omega_I^B \quad (4.12)$$

where 
$${}_L\omega_I^B = {}^B\mathbf{C}^L {}_L\omega_I^L$$

and 
$${}_L\omega_I^L = [0 \quad 0 \quad \dot{u}]^T.$$

The superscripts denote the coordinate frame in which the vector is expressed.

#### 4.4 Attitude Dynamics

The general attitude motion of a satellite is given by Euler's equation:

$$\frac{d}{dt}\mathbf{h}^B + \omega^B \times \mathbf{h}^B = \mathbf{N}^B \quad (4.13)$$

where  $\mathbf{h}^B$  is the angular momentum vector of the body,  $\omega$  is the inertial angular velocity vector of the body, and  $\mathbf{N}$  is the disturbing torque. If the origin of the body frame coincides with the center of mass of the satellite and the axes are aligned with the principal axes of the satellite then  $\mathbf{h}^B = [I_1\omega_1 \quad I_2\omega_2 \quad I_3\omega_3]^T$  and Equation 4.13 becomes

$$\begin{aligned} I_1\dot{\omega}_1 + \omega_2\omega_3(I_3 - I_2) &= N_1 \\ I_2\dot{\omega}_2 + \omega_1\omega_3(I_1 - I_3) &= N_2 \\ I_3\dot{\omega}_3 + \omega_1\omega_2(I_2 - I_1) &= N_3. \end{aligned} \quad (4.14)$$

Consider a gyrostat containing a momentum wheel which has its spin axis aligned with the  $\mathbf{k}$ -axis of the body and has constant angular momentum  $h_w$ . The total angular

momentum of the satellite becomes  $\mathbf{h}^B = [I_1\omega_1 \quad I_2\omega_2 \quad I_3\omega_3 + h_w]^T$  and Equation 4.13 can be rewritten as follows,

$$\begin{aligned} I_1\dot{\omega}_1 + \omega_2\omega_3(I_3 - I_2) - h_w\omega_2 &= N_1 \\ I_2\dot{\omega}_2 + \omega_1\omega_3(I_1 - I_3) + h_w\omega_1 &= N_2 \\ I_3\dot{\omega}_3 + \omega_1\omega_2(I_2 - I_1) &= N_3. \end{aligned} \quad (4.15)$$

The gravity gradient torque  $\mathbf{N}_{GG}$  as derived by [Shuster, 1989] is given by

$$\mathbf{N}_{GG} = \frac{3\mu}{r^3} \hat{\mathbf{r}} \times (\mathbf{I} \hat{\mathbf{r}}) \quad (4.16)$$

where  $r$  is the satellite orbit radius,  $\hat{\mathbf{r}}$  is the unit vector in the radial direction, and  $\mathbf{I}$  is the moment of inertia tensor. Usually the inertia tensor is known in the body frame. Since  $\hat{\mathbf{r}}$  in the local frame is just  $[1 \ 0 \ 0]^T$ , we can easily convert it to the body frame by writing

$$\hat{\mathbf{r}}^B = \mathbf{B} \mathbf{C}^L \hat{\mathbf{r}}^L = \mathbf{B} \mathbf{C}^L [1 \ 0 \ 0]^T. \quad (4.17)$$

$\mathbf{B} \mathbf{C}^L$  can be expressed in terms of either quaternions or Euler angles. If quaternions are used the gravity gradient torque becomes

$$\mathbf{N}_{GG}^B = \frac{3\mu}{r^3} \begin{bmatrix} 4(I_3 - I_2)(q_2q_1 - q_4q_3)(q_3q_1 + q_4q_2) \\ 2(I_1 - I_3)(q_1^2 - q_2^2 - q_3^2 + q_4^2)(q_3q_1 + q_4q_2) \\ 2(I_2 - I_1)(q_1^2 - q_2^2 - q_3^2 + q_4^2)(q_2q_1 - q_4q_3) \end{bmatrix}. \quad (4.18)$$

To summarize, the quaternion and inertial velocity equations differential equations are

$$\begin{aligned} \dot{q}_1 &= [q_2(\omega_3 + \dot{u}) - q_3\omega_2 + q_4\omega_1] / 2 \\ \dot{q}_2 &= [-q_1(\omega_3 + \dot{u}) + q_3\omega_1 + q_4\omega_2] / 2 \\ \dot{q}_3 &= [q_1\omega_2 - q_2\omega_1 + q_4(\omega_3 - \dot{u})] / 2 \\ \dot{q}_4 &= [-q_1\omega_1 - q_2\omega_2 - q_3(\omega_3 - \dot{u})] / 2 \\ I_1\dot{\omega}_1 &= -(I_3 - I_2)\omega_2\omega_3 + 12\Omega^2(I_3 - I_2)(q_2q_1 - q_4q_3)(q_3q_1 + q_4q_2) - h_w\omega_2 \\ I_2\dot{\omega}_2 &= -(I_1 - I_3)\omega_1\omega_3 + 6\Omega^2(I_1 - I_3)(q_1^2 - q_2^2 - q_3^2 + q_4^2)(q_3q_1 + q_4q_2) + h_w\omega_1 \\ I_3\dot{\omega}_3 &= -(I_2 - I_1)\omega_1\omega_2 + 6\Omega^2(I_2 - I_1)(q_1^2 - q_2^2 - q_3^2 + q_4^2)(q_2q_1 - q_4q_3) \end{aligned} \quad (4.19)$$

where  $\Omega^2 = \mu / r^3$ .

If, on the other hand,  ${}^B C^L$  is written terms of Euler angles, substituting the gravity gradient torque  $N_{GG}(y,r,p)$  into equations (4.15) and neglecting product of angles and eccentricity gives the linearized Euler angle equations of motion derived by Melvin [1991].

$$\begin{aligned} I_1 \ddot{y} &= -[h_w + n(I_3 - I_2)]ny - [h_w - (I_1 + I_2 - I_3)n]\dot{r} \\ I_2 \ddot{r} &= -[h_w + 4n(I_3 - I_2)]nr + [h_w - (I_1 + I_2 - I_3)n]\dot{y} \\ I_3 \ddot{p} &= -3(I_2 - I_1)n^2 p - I_3 \ddot{u} \end{aligned} \quad (4.20)$$

where  $n$  is the mean motion of the satellite. Note that the " $r$ " in Equation 4.20 refers to the roll angle and not to the satellite radius as in other equations.

#### 4.5 GPS Attitude Observations

As mentioned earlier, the GPS receivers measure a phase difference between antennas. If the integer ambiguity,  $k$ , and line bias,  $\beta$ , have been resolved, the corresponding range difference can be computed directly by

$$\Delta r = \Delta \varphi + k - \beta. \quad (4.21)$$

This range difference measurement  $\Delta r$  for a particular GPS satellite and baseline is the projection of the baseline vector  $\mathbf{b}$  onto the user to GPS direction vector  $\mathbf{e}$  plus an unknown error,  $\varepsilon$ , as follows:

$$\Delta r = \mathbf{b} \cdot \mathbf{e} + \varepsilon. \quad (4.22)$$

Since  $\mathbf{e}$  is measured in inertial coordinates, it must be transformed to the body frame with the inertial to body transformation matrix. The range difference is now given as

$$\Delta r = (\mathbf{b}^B)^T {}^B C^I \mathbf{e}^I + \varepsilon \quad (4.23)$$

The error in the range difference measurement for each GPS satellite is modeled as a discrete first order Markov process as follows:

$$\varepsilon_k = a \varepsilon_{k-1} + b w_k \quad (4.24)$$

where  $\epsilon_k$  is the range error at time  $t_k$ , and  $w_k$  is the corresponding element of a discrete white sequence with zero mean and unity standard deviation. The coefficients  $a$  and  $b$  are computed as

$$a = e^{-\beta \Delta t}, b = (1 - a^2)^{1/2} \sigma \quad (4.25)$$

where  $\sigma$  is the steady state standard deviation of  $\epsilon_k$ ,  $\beta$  is the inverse time constant, and  $\Delta t$  is the time interval. At every time step the error is computed for each GPS satellite and baseline pair and is added to the range difference measurements for those satellites which are visible. This type of model can be made to represent slowly varying error components such as multipath, line bias values, or structural bending. An example of a multipath type error is illustrated in Figure 4.3.

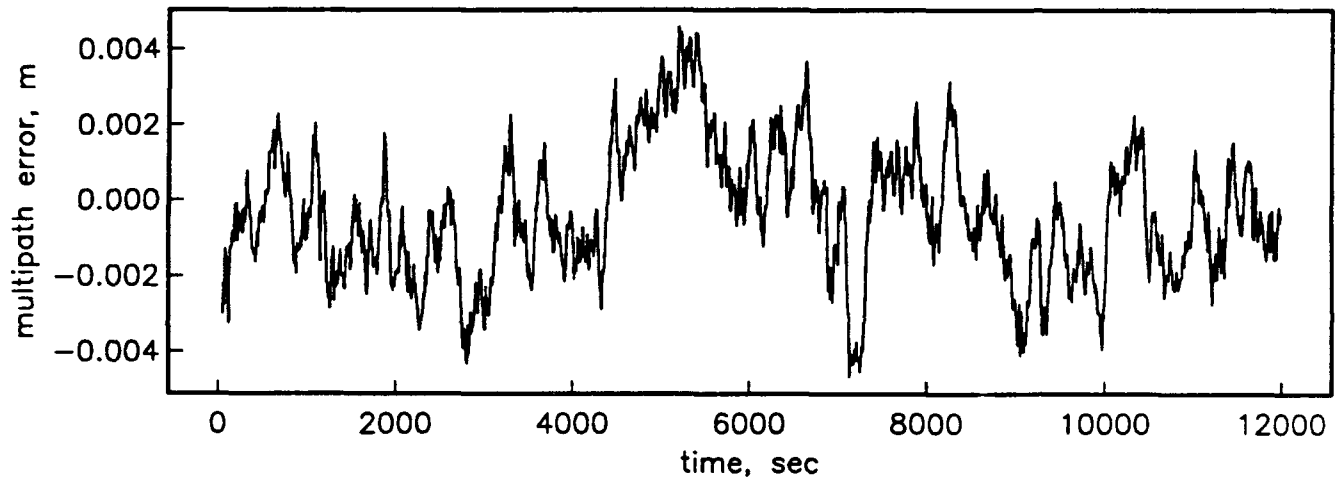


Figure 4.3 Multipath Error Example

A GPS satellite is visible to the user if the cosine of the zenith angle  $\zeta$ , is less than the sine of the mask angle  $\gamma$  or

$$\cos \zeta < \cos(90^\circ - \gamma) = \sin \gamma \quad (4.26)$$

where  $\cos \zeta = \hat{r} \cdot \mathbf{e}$ .

See Figure 4.4 for an illustration of these angles. This situation is ideal in that it assumes that the antennas are omni-directional; signals to the antennas are only blocked by the Earth. Blockage due to the satellite itself is not considered here. A more accurate model would specify a separate mask angle for each antenna and take into account satellite appendages which may block the GPS signal to certain antennas.

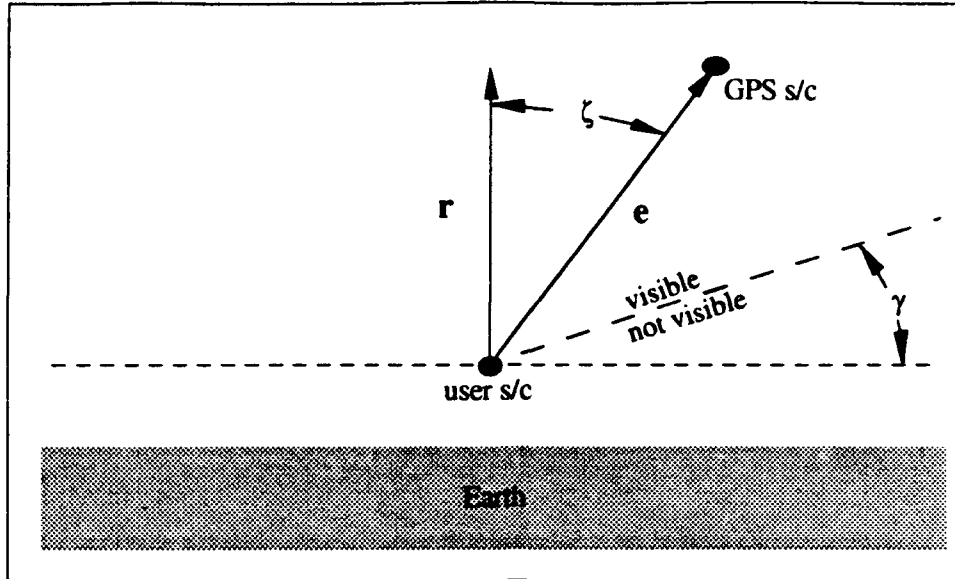


Figure 4.4. GPS Visibility

#### 4.6 Attitude Point Solution Methods

##### Nonlinear Least Squares

Given  $m$  baselines and  $n$  satellites, an optimal attitude solution is obtained by minimizing the following cost function with respect to  ${}^B\hat{C}^I$ :

$$J({}^B\hat{C}^I) = \sum_{i=1}^m \sum_{j=1}^n w_{ij} \left[ \Delta r_{ij} - (\mathbf{b}_i^B)^T ({}^B\hat{C}^I \mathbf{e}_j^I) \right]^2 \quad (4.27)$$

where  $w_{ij}$  is the measurement weighting factor.

Given an initial estimate of the inertial to body transformation matrix,  ${}^B\hat{C}_0^I$ , an iterative approach may be used to solve for the best estimate of  ${}^B\hat{C}^I$ . By linearizing the cost function about the current estimate of the attitude matrix a better estimate can be generated from

$${}^B\hat{C}^I = \delta C {}^B\hat{C}_0^I \equiv (\mathbf{1} + \Theta^x) {}^B\hat{C}_0^I \quad (4.28)$$

where  $\mathbf{1}$  is the identity matrix and  $\Theta^x$  is the cross product matrix associated with  $\delta\theta = [\delta\theta_1 \ \delta\theta_2 \ \delta\theta_3]^T$  as in Equation 4.8.  $\delta\theta_1$ ,  $\delta\theta_2$  and  $\delta\theta_3$  represent small rotations about the estimated body axes. Using

$$\Delta \hat{r}_{ij} = (\mathbf{b}_i^B)^T ({}^B\hat{C}_0^I \mathbf{e}_j^I) \quad (4.29)$$

to predict the range difference, the cost function can be rewritten as

$$J({}^B\hat{C}^I) = \sum_{i=1}^m \sum_{j=1}^n w_{ij} \left[ \delta r_{ij} - (\mathbf{b}_i^B)^T (\Theta^x {}^B\hat{C}_0^I \mathbf{e}_j^I) \right]^2 \quad (4.30)$$

where  $\delta r_{ij} \equiv \Delta r_{ij} - \Delta \hat{r}_{ij}$ . (4.31)

The second term in the cost function can be rearranged as follows

$$(\mathbf{b}_i^B)^T (\Theta^x {}^B\hat{C}_0^I \mathbf{e}_j^I) = ({}^B\hat{C}_0^I \mathbf{e}_j^I)^T \mathbf{B}_i^x \delta \theta \quad (4.32)$$

where  $\mathbf{B}_i^x$  is the cross product matrix associated with baseline vector  $\mathbf{b}_i$ .  
Then the linearized cost function can be written as

$$J(\delta \theta)|_{\hat{C}_0^I} = \sum_{i=1}^m \sum_{j=1}^n w_{ij} \left( \mathbf{H}_{ij} \delta \theta - \delta r_{ij} \right)^2 \quad (4.33)$$

where the measurement gradient,  $\mathbf{H}$ , is formed by

$$\mathbf{H} = \begin{bmatrix} ({}^B\hat{C}_0^I \mathbf{e}_1^I)^T \mathbf{B}_1^x \\ \vdots \\ ({}^B\hat{C}_0^I \mathbf{e}_1^I)^T \mathbf{B}_m^x \\ ({}^B\hat{C}_0^I \mathbf{e}_2^I)^T \mathbf{B}_1^x \\ \vdots \\ ({}^B\hat{C}_0^I \mathbf{e}_n^I)^T \mathbf{B}_m^x \end{bmatrix}. \quad (4.34)$$

Now, to find the best estimate of  ${}^B\hat{C}^I$  solve the system of equations  $\mathbf{H}_{ij} \delta \theta = \delta r_{ij}$  for  $\delta \theta$ .  
Recompute the attitude matrix using Equation 4.28 and repeat until  $\delta \theta$  gets sufficiently small.

The quaternion formulation is similar except the linearized version of the attitude matrix in Equation 4.28 takes on the form

$${}^B\hat{C}^I = (1 + 2Q^x) {}^B\hat{C}_0^I \quad (4.35)$$

where  $Q^x$  is the cross product matrix associated with  $\delta \bar{q} = [\delta q_1 \quad \delta q_2 \quad \delta q_3]^T$ .

### SVD Point Solution

Markley [1988] derives a fast method for solving a similar cost function using singular value decomposition. This cost function, known as Wahba's problem, is given as

$$J({}^B C^I) = \frac{1}{2} \sum_{i=1}^n w_i \left| \hat{s}_i^B - {}^B C^I \hat{s}_i^I \right|^2 \quad (4.36)$$

where the unit vectors  $\hat{s}_i^B$  and  $\hat{s}_i^I$  are the direction vectors to the  $i$ th object in the body frame and inertial frame, respectively. Cohen [1992] shows how the Markley solution can be applied GPS attitude determination. One advantage of this method is that it does not require any prior knowledge of the attitude. Hence, this solution could be used in initializing a Kalman filter.

To derive the SVD solution (following Cohen [1992]) convert the cost function in Equation 4.27 to matrix form

$$J(\hat{C}) = \left\| \mathbf{W}_B^{1/2} (\Delta \mathbf{R} - \mathbf{B}^T \hat{C} \mathbf{E}) \mathbf{W}_E^{1/2} \right\|_F^2 \quad (4.37)$$

where  $\Delta \mathbf{R}$  is the differential range measurements assembled into a  $(m \times n)$  as follows

$$\Delta \mathbf{R} = \begin{bmatrix} \Delta r_{11} & \Delta r_{12} & \cdots & \Delta r_{1n} \\ \Delta r_{21} & \Delta r_{22} & & \vdots \\ \vdots & & \ddots & \\ \Delta r_{m1} & \cdots & & \Delta r_{mn} \end{bmatrix} \quad (4.38)$$

and where  $\hat{C}$  is the estimate of the inertial to body transformation matrix,  $\mathbf{B}$  are the  $m$  baseline vectors in the body frame concatenated into a  $(3 \times m)$  matrix,  $\mathbf{E}$  are the  $n$  user to GPS direction vectors in the inertial frame concatenated into a  $(3 \times n)$  matrix, and  $\mathbf{W}_B$  and  $\mathbf{W}_E$  are weighting matrices for the baseline and direction vectors, respectively. The superscripts have been omitted here for simplicity.

The Frobenius norm for a matrix,  $\mathbf{M}$ , is defined as

$$\|\mathbf{M}\|_F^2 \equiv \text{trace}(\mathbf{M}^T \mathbf{M}). \quad (4.39)$$

Using the trace equivalence of the Frobenius norm, the matrix form of the cost function can be expanded to give

$$\begin{aligned}
 J(\hat{C}) = & \text{trace} \left( \mathbf{W}_E^{1/2} \Delta \mathbf{R}^T \mathbf{W}_B \Delta \mathbf{R} \mathbf{W}_E^{1/2} \right) \\
 & - 2 \text{trace} \left( \mathbf{W}_E^{1/2} \Delta \mathbf{R}^T \mathbf{W}_B \mathbf{B}^T \hat{C} \mathbf{E} \mathbf{W}_E^{1/2} \right) \\
 & + \text{trace} \left( \mathbf{W}_E^{1/2} (\hat{C} \mathbf{E})^T \mathbf{B} \mathbf{W}_B \mathbf{B}^T \hat{C} \mathbf{E} \mathbf{W}_E^{1/2} \right).
 \end{aligned} \tag{4.40}$$

Because the first term is independent of attitude, it drops out when minimizing with respect to the attitude. With the proper choice of  $\mathbf{W}_B$  the last term also becomes independent of attitude and drops out. Choosing  $\mathbf{W}_B$  will be discussed below.

After rearranging the second term, the trace being invariant to cyclic permutations, the problem now is one of *maximizing* the new cost function

$$J'(\hat{C}) = \text{trace}(\hat{C} \mathbf{E} \mathbf{W}_E \Delta \mathbf{R}^T \mathbf{W}_B \mathbf{B}^T) \equiv \text{trace}(\hat{C} \mathbf{G}^T) \tag{4.41}$$

where  $\mathbf{G} \equiv \mathbf{B} \mathbf{W}_B \Delta \mathbf{R} \mathbf{W}_E \mathbf{E}^T$ .

The optimal value of the attitude matrix can be found by taking the singular value decomposition of the matrix  $\mathbf{G}$ . The singular value decomposition is given by

$$\mathbf{G} = \mathbf{U} \mathbf{S} \mathbf{V}^T \tag{4.42}$$

where  $\mathbf{U}$  and  $\mathbf{V}$  are orthogonal matrices and  $\mathbf{S}$  is a diagonal matrix with  $S_{11} \geq S_{22} \geq S_{33} \geq 0$ .

To ensure that the optimal attitude matrix is right-handed, the signs of the third column of  $\mathbf{U}$  and  $\mathbf{V}$  matrices are adjusted so that their determinant is equal to one. These new matrices will be called  $\mathbf{U}_+$  and  $\mathbf{V}_+$ . The sign of the last element in the  $\mathbf{S}$  matrix is also adjusted so that the new matrix,  $\mathbf{S}'$ , will have

$$S'_{33} = \det(\mathbf{U})\det(\mathbf{V})S_{33}. \tag{4.43}$$

Now  $\mathbf{G}$  can be rewritten as

$$\mathbf{G} = \mathbf{U}_+ \mathbf{S}' \mathbf{V}_+^T. \tag{4.44}$$

and the cost function becomes

$$\begin{aligned} J'(\hat{C}) &= \text{trace}(\hat{C} \mathbf{V}_+ \mathbf{S}' \mathbf{U}_+^T) = \text{trace}(\mathbf{S}' \mathbf{U}_+^T \hat{C} \mathbf{V}_+) \\ &= \text{trace}(\mathbf{S}' \mathbf{A}) \end{aligned} \quad (4.45)$$

where  $\mathbf{A} \equiv \mathbf{U}_+^T \hat{C} \mathbf{V}_+$ . (4.46)

Since  $\mathbf{A}$  is an orthogonal matrix, an Euler angle/axis representation can be used to express it as follows,

$$\mathbf{A} = \begin{bmatrix} \cos\alpha + \lambda_1^2(1 - \cos\alpha) & \lambda_3 \sin\alpha + \lambda_1 \lambda_2(1 - \cos\alpha) & -\lambda_2 \sin\alpha + (1 - \cos\alpha)\lambda_1 \lambda_3 \\ -\lambda_3 \sin\alpha + \lambda_2 \lambda_1(1 - \cos\alpha) & \cos\alpha + \lambda_2^2(1 - \cos\alpha) & \lambda_1 \sin\alpha + (1 - \cos\alpha)\lambda_2 \lambda_3 \\ \lambda_2 \sin\alpha + \lambda_3 \lambda_2(1 - \cos\alpha) & -\lambda_1 \sin\alpha + \lambda_3 \lambda_2(1 - \cos\alpha) & \cos\alpha + (1 - \cos\alpha)\lambda_3^2 \end{bmatrix} \quad (4.47)$$

where  $\bar{\lambda} = [\lambda_1 \ \lambda_2 \ \lambda_3]^T$  is the rotation axis and  $\alpha$  is the rotation angle. Substituting this into Equation 4.45 gives

$$\begin{aligned} J'(\hat{C}) &= S'_1[\cos\alpha + \lambda_1^2(1 - \cos\alpha)] \\ &\quad + S'_2[\cos\alpha + \lambda_2^2(1 - \cos\alpha)] \\ &\quad + S'_3[\cos\alpha + \lambda_3^2(1 - \cos\alpha)]. \end{aligned} \quad (4.48)$$

Since  $S'_1, S'_2, S'_3 \geq 0$  and  $\lambda_1^2, \lambda_2^2, \lambda_3^2 \leq 1$ , then  $J'(\hat{C})$  is maximized for  $\alpha = 0$ .  $\mathbf{A}$  then is equal to the identity matrix, and the optimal value of  $\hat{C}$  is given by

$$\hat{C}_{\text{optimal}} = \mathbf{U}_+ \mathbf{V}_+^T. \quad (4.49)$$

Cohen [1992] points out that to realize the full potential of the SVD solution, the baselines should form an orthogonal set.  $\mathbf{W}_B$  is a measure of how much the measurements have to be scaled to transform the baselines into an equivalent orthonormal basis. So  $\mathbf{W}_B$  is chosen such that

$$\mathbf{W}_B = \mathbf{V}_B \mathbf{S}_B^{-2} \mathbf{V}_B^T \quad (4.50)$$

where the singular value decomposition of  $\mathbf{B}$  is given by

$$\mathbf{B} = \mathbf{U}_B \mathbf{S}_B \mathbf{V}_B^T. \quad (4.51)$$

and  $\mathbf{S}^{-2}$  denotes taking the reciprocal squared of each diagonal element. Using this SVD method a new point solution may be formed at each measurement epoch.

#### 4.7 Attitude Filters

Incorporating known dynamics into the attitude determination process will allow us to obtain a better solution than using the solutions presented above. As [Lefferts, 1982] points out, the Kalman filter does this by using a dynamical model to propagate the attitude in time along with a measurement model to obtain the best estimate of the attitude. For this study two versions of a Kalman filter have been implemented to estimate spacecraft attitude. One is an Euler angle formulation, while the other is a quaternion formulation. The general equations for a Kalman filter are presented next followed by the specific equations for each filter.

##### General Kalman Filter Equations

(For background information see, for example Gelb [1984]).

The time update of the Kalman filter is given by

$$\mathbf{x}_k^- = \mathbf{x}_{k-1}^+ + \int_{t_{k-1}}^{t_k} \dot{\mathbf{x}}(t) dt \quad (4.52)$$

$$\mathbf{P}_k^- = \Phi \mathbf{P}_{k-1}^+ \Phi^T + \mathbf{Q}$$

where  $\mathbf{x}_k$  and  $\mathbf{P}_k$  are the state vector and covariance matrix at time  $t_k$ . The superscripts, - and +, denote prior and post measurement update, respectively.  $\Phi$  is the state transition matrix from time  $t_{k-1}$  to time  $t_k$ , and  $\mathbf{Q}$  is the process noise matrix.

The state transition matrix satisfies the equation

$$\dot{\Phi} = \mathbf{F} \Phi, \quad \Phi(t_0) = \mathbf{1}, \quad (4.53)$$

where  $\mathbf{F} = \partial \dot{\mathbf{x}} / \partial \mathbf{x}$  is the linearized dynamics matrix. An approximate solution for  $\Phi$  is given by Melvin [1991]. The result is

$$\Phi_{ij} = F_{ij}^0 + \Delta t \left( F_{ij}^1 + \Delta t \left( \frac{1}{2!} F_{ij}^2 + \Delta t \left( \frac{1}{3!} F_{ij}^3 \right) \right) \right) \quad (4.54)$$

where  $F_{ij}^0$  is the identity matrix and  $\Delta t$  is the filter time increment.

The measurement update equations for the standard Kalman Filter are

$$\begin{aligned} \mathbf{K}_k &= \mathbf{P}_k^- \mathbf{H}_k^T (\mathbf{H}_k \mathbf{P}_k^- \mathbf{H}_k^T + \mathbf{R}_k)^{-1} \\ \mathbf{x}_k^+ &= \mathbf{x}_k^- + \mathbf{K}_k \Delta z_k \\ \mathbf{P}_k^+ &= (\mathbf{1} - \mathbf{K}_k \mathbf{H}_k) \mathbf{P}_k^- \end{aligned} \quad (4.55)$$

where  $\mathbf{K}$  is the Kalman gain,  $\mathbf{R}$  is the variance of the measurement noise, and  $\Delta z$  is the measurement residual.

### Euler Angle Filter

The state vector for the Euler angle filter contains the yaw, roll, pitch, and their rates,  $(y, r, p, \dot{y}, \dot{r}, \dot{p})$ . The linearized equations of motion (4.20) are numerically integrated to advance the state estimate to the current time. The covariance matrix is propagated forward with the state transition matrix. The dynamics matrix used to compute the state transition matrix is derived directly from Equations 4.20 and is shown in Appendix B.

For each measurement taken at the current time the user to GPS direction vectors are converted from the inertial to the local frame (using the position estimated by the navigation filter). Since the Euler angles cannot be simply added together, the filter must always linearize about the local level. Thus, the residual ( $\delta r_{ij}$  - for baseline  $i$  and satellite  $j$ .) used for the measurement update is calculated according to Equation (4.31) with the  $\Delta \hat{r}_{ij}$  given by

$$\Delta \hat{r}_{ij} = (\mathbf{b}_i^B)^T (\mathbf{1} + \Theta^x) \mathbf{e}_j^L \quad (4.56)$$

The  $\delta\theta_1$ ,  $\delta\theta_2$ , and  $\delta\theta_3$  used to form  $\Theta^x$  are the yaw, roll, and pitch angles, respectively. The measurement gradient vector for the angle states,  $\mathbf{H}_{ij}$ , for a single baseline  $i$  and satellite  $j$ , then is

$$\mathbf{H}_{ij} = (\mathbf{e}_j^L)^T \mathbf{B}_i^x. \quad (4.57)$$

and the elements corresponding to the rate states are zero. The measurement update takes the form shown in Equation 4.55.

One disadvantage to this formulation is that deviations from the local level must remain small for the filter to converge since we are linearizing about the local frame. Moving to a quaternion filter, however, alleviates this problem.

### Quaternion Filter

The state vector for the quaternion filter contains  $q_1, q_2, q_3$ , and the inertial angular velocity of the body. The fourth element of  $\mathbf{q}$ ,  $q_4$ , is included in the state propagation, but is not used in the measurement update or covariance. This is based on Lefferts, et al. [1982] and is described further in the following.

Similar to the Euler angle filter, the quaternion equations of motion (4.19) are numerically integrated to advance the state estimate to the current time, and the covariance matrix is propagated forward with the state transition matrix. The elements of

the dynamics matrix used to compute the state transition matrix are presented in Appendix B.

The best estimate of the transformation matrix from inertial to body coordinates  ${}^B\hat{C}_0^I$  is computed based on the quaternion state. The range difference prediction is then,

$$\Delta\hat{r}_{ij} = (\mathbf{b}_i^B)^T {}^B\hat{C}_0^I \mathbf{e}_j^I. \quad (4.58)$$

and the measurement residual is computed by subtracting this from the observed  $\Delta r_{ij}$ .

If we linearize about the current attitude estimate, an improved estimate of the transformation matrix can be modeled as,

$${}^B\hat{C}^I = (\mathbf{1} + 2\mathbf{Q}^\times) {}^B\hat{C}_0^I \quad (4.59)$$

where  $\mathbf{Q}^\times$  is the cross product matrix for a small correction rotation represented by the quaternion  $\delta\mathbf{q}$ . Thus the measurement gradient matrix,  $\mathbf{H}$ , for the quaternion states is

$$\mathbf{H}_{ij} = 2({}^B\hat{C}^I \mathbf{e}_j^I)^T \mathbf{B}_i^\times. \quad (4.60)$$

The elements of the gradient matrix corresponding to the velocity states are zero.

The Kalman gain calculation and covariance update follow Equations 4.55, but the state update is different. The first three elements of the correction quaternion  $\delta\mathbf{q}$  are computed by the filter. The fourth element,  $\delta q_4$ , is set to normalize the quaternion as follows,

$$\delta q_4 = \sqrt{1 - \delta q_1^2 - \delta q_2^2 - \delta q_3^2}. \quad (4.61)$$

The correction quaternion,  $\delta\mathbf{q}$ , is then combined with the apriori estimate,  $\hat{\mathbf{q}}_k^-$  according to the quaternion composition rule. The general form of the composition is given by [c.f. Shuster],

$$\mathbf{q}'' = \mathbf{q}' \otimes \mathbf{q} = \begin{bmatrix} q'_4 & q'_3 & -q'_2 & q'_1 \\ -q'_3 & q'_4 & q'_1 & q'_2 \\ q'_2 & -q'_1 & q'_4 & q'_3 \\ -q'_1 & -q'_2 & -q'_3 & q'_4 \end{bmatrix} \begin{bmatrix} q_1 \\ q_2 \\ q_3 \\ q_4 \end{bmatrix} \quad (4.62)$$

where  $\mathbf{q}$  is the first rotation expressed in the coordinates of the original frame;  $\mathbf{q}'$  is the second rotation expressed in the coordinates of the intermediate frame; and  $\mathbf{q}''$  is the combined rotation expressed in the final frame.

In our case,  $\hat{\mathbf{q}}_k^-$ , is the first rotation, and  $\delta\mathbf{q}$  is the second.

#### 4.8 Navigation Filter

The attitude filter needs information about the user satellite's position to calculate the inertial to local transformation. The gravity gradient torque also depends on the user's position. Usually only an estimate of the position is available, so an extended Kalman filter, like that used in the attitude filter, was considered. The state, containing the position and velocity, is propagated by integrating the orbit equations of motion (4.1) while the covariance matrix is propagated with the state transition matrix. Appendix B contains the non-zero elements of the dynamics matrix used to compute the state transition matrix.

For each pseudorange measurement,  $\rho$ , the residual,  $\delta\rho$ , is given by

$$\delta\rho = \rho - |\hat{\mathbf{r}}_{\text{rel}}| \quad (4.63)$$

where the current estimate of the relative distance between the GPS and user satellite is

$$\hat{\mathbf{r}}_{\text{rel}} = \begin{bmatrix} x_{\text{gps}} - \hat{x}_0 \\ y_{\text{gps}} - \hat{y}_0 \\ z_{\text{gps}} - \hat{z}_0 \end{bmatrix} \quad (4.64)$$

and where  $\hat{x}_0$ ,  $\hat{y}_0$ , and  $\hat{z}_0$  are the current estimates of the position coordinates. The measurement gradient matrix can be computed as follows,

$$\mathbf{H} = [\hat{\mathbf{e}}_1 \quad \hat{\mathbf{e}}_2 \quad \hat{\mathbf{e}}_3 \quad 0 \quad 0 \quad 0] \quad (4.65)$$

where  $\hat{\mathbf{e}} = \frac{\hat{\mathbf{r}}_{\text{rel}}}{|\hat{\mathbf{r}}_{\text{rel}}|}$ .

Similarly, the range rate measurement residual,  $\delta\dot{\rho}$ , is given by

$$\delta\dot{\rho} = \dot{\rho} - \hat{\mathbf{v}}_{\text{rel}} \cdot \hat{\mathbf{e}} \quad (4.66)$$

where the current estimate of the relative velocity between the GPS satellite and user is

$$\hat{\mathbf{v}}_{\text{rel}} = \begin{bmatrix} \dot{x}_{\text{gps}} - \hat{\dot{x}}_0 \\ \dot{y}_{\text{gps}} - \hat{\dot{y}}_0 \\ \dot{z}_{\text{gps}} - \hat{\dot{z}}_0 \end{bmatrix} \quad (4.67)$$

and where  $\hat{\dot{x}}_0$ ,  $\hat{\dot{y}}_0$ , and  $\hat{\dot{z}}_0$  are the current estimates of the velocity coordinates. The measurement gradient vector can be computed as

$$\begin{aligned}
 H_1 &= \frac{-\hat{v}_{rel_1}}{|\hat{r}_{rel}|} + \frac{\hat{v}_{rel} \cdot \hat{r}_{rel}}{|\hat{r}_{rel}|^3} \\
 H_2 &= \frac{-\hat{v}_{rel_2}}{|\hat{r}_{rel}|} + \frac{\hat{v}_{rel} \cdot \hat{r}_{rel}}{|\hat{r}_{rel}|^3} \\
 H_3 &= \frac{-\hat{v}_{rel_3}}{|\hat{r}_{rel}|} + \frac{\hat{v}_{rel} \cdot \hat{r}_{rel}}{|\hat{r}_{rel}|^3} \\
 H_4 &= \hat{e}_1 \\
 H_5 &= \hat{e}_2 \\
 H_6 &= \hat{e}_3.
 \end{aligned}
 \tag{4.68}$$

#### 4.9 Simulation

To study various attitude determination methods a simulation was developed implementing the models described in the previous sections. It is comprised of three main parts -- the truth models including the user attitude and orbital dynamics, the measurement models for observed range, range rate, and range differences, and finally the estimation models for both attitude and navigation. The main modules and data flow within the simulation are illustrated in Figure 4.5.

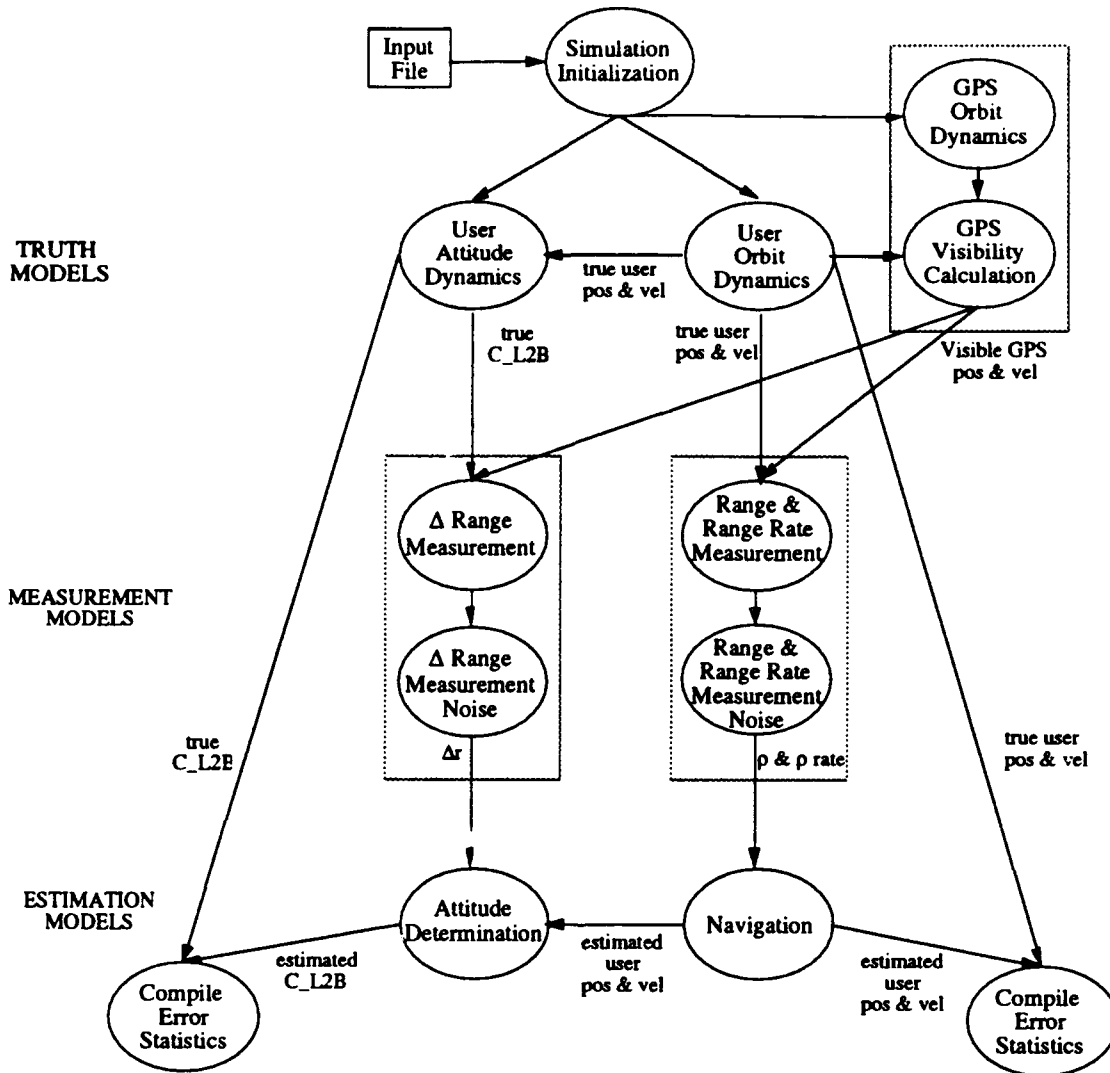


Figure 4.5. Simulation Data Flow

Care was taken to separate each model or major calculation into different modules. Coding in this manner affords a number of advantages. For example, changes and upgrades can be implemented with ease by just replacing the old subroutine with the new one. In addition, each subroutine can be independently tested which simplifies debugging and verification.

Initial orbit and attitude conditions, satellite configuration data, and filter parameters are defined in an input file. These values can then be easily be changed to see the effect that various parameters have on the results. For this study a nominal set of input parameters for the nadir pointing satellite are shown in Table 4.1.

Table 4.1 Nominal Simulation Initialization Parameters

Orbital elements for the user satellite

semimajor axis: 7000 km  
 eccentricity: 0.0  
 inclination: 60 deg  
 ascending node: 135 deg  
 argument of perigee: 292 deg  
 mean anomaly: 345 deg

Satellite Configuration

Moments of inertia:  $I_1 = 1000 \text{ kg m}^2$   
 $I_2 = 2000 \text{ kg m}^2$   
 $I_3 = 2010 \text{ kg m}^2$   
 Angular momentum wheel:  $h_w = 50 \text{ kg m}^2/\text{s}$   
 Baselines: 3 baselines along principal axes of body, each 1 meter long

Measurement Errors

Range difference:  $\sigma = 2 \text{ mm}$   
 inverse time constant  $\beta = 100/\text{sec}$  (~white noise)  
 Pseudorange:  $\sigma = 6 \text{ m}$  (white noise)  
 Pseudorange rate:  $\sigma = .025 \text{ m/s}$  (white noise)

Initial attitude

True:  $y_0 = r_0 = p_0 = 0.5 \text{ deg}$   
 $\dot{y}_0 = \dot{r}_0 = \dot{p}_0 = 0.001 \text{ deg / s}$   
 Estimated:  $y_0 = r_0 = p_0 = 0 \text{ deg}$   
 $\dot{y}_0 = \dot{r}_0 = \dot{p}_0 = 0 \text{ deg / s}$

Initial position

True: (calculated from orbital elements above)  
 Estimated: (expressed as a deviation from the truth)  
 $\delta x_0 = \delta y_0 = \delta z_0 = 1 \text{ m}$   
 $\delta \dot{x}_0 = \delta \dot{y}_0 = \delta \dot{z}_0 = 0.001 \text{ m / s}$

Quaternion filter parameters

quaternion state process noise =  $1 \times 10^{-9} \text{ (rad)}^2$   
 inertial velocity state process noise =  $1 \times 10^{-12} \text{ (rad/s)}^2$   
 measurement noise variance =  $4 \times 10^{-6} \text{ m}^2$

Euler angle filter parameters

angle state process noise =  $1 \times 10^{-8} \text{ (deg)}^2$   
 angle rate state process noise =  $1 \times 10^{-8} \text{ (deg/s)}^2$   
 measurement noise variance =  $4 \times 10^{-6} \text{ m}^2$

Each simulation was run for 200 minutes or approximately 2 orbital periods. The time between measurement updates was 10 seconds. A variable step integrator was used to propagate the state between epochs. This integrator is a 4th order Runge-Kutta library routine.

The SVD point solution, the Euler angle filter, and the quaternion filter were all executed with the above parameters. Modifications were then made to this nadir pointing scenario to illustrate the performance of various algorithms. For example, the initial attitude was changed so that the user satellite was not nadir pointing. Again, all three attitude determination methods were executed. Other cases studied include adding a multipath type error to the range difference measurements, defining a larger mask angle, and using a baseline configuration that is not optimal. In addition, the results from the navigation filter are presented below using 1) random measurement noise, and 2) selective availability.

#### 4.10 Results and Discussion

Summaries of the attitude determination and navigation results are presented below in Tables 4.2 and 4.3 respectively. Cases using the SVD point solution are denoted with SVD, those using the Euler angle filter are denoted with E, and those using the quaternion filter are denoted with Q.

Table 4.2 Attitude Determination Results

Case	Method	RMS of Errors in degrees x 10 <sup>-2</sup>			
		yaw	roll	pitch	3-axis
Nadir Pointing	SVD	4.76	4.85	4.78	8.31
Nadir Pointing	E	1.35	1.04	1.89	2.55
Nadir Pointing	Q	1.26	1.16	1.62	2.36
Off-Nadir Pointing	SVD	4.78	4.85	4.79	8.32
Off-Nadir Pointing	E	6.60	6.09	6.12	10.63
Off-Nadir Pointing	Q	1.25	1.16	1.62	2.35
Multipath Noise	Q	4.28	5.62	5.19	8.76
Multipath Noise	SVD	4.35	5.56	5.15	8.77
Non-optimal Baselines	Q	1.85	1.25	2.29	3.20
Equatorial Orbit	Q	1.25	1.06	1.50	2.22
Polar Orbit	Q	1.22	1.13	1.67	2.36
Larger Mask Angle	Q	2.11	1.75	2.39	3.63
Selective Availability	Q	1.10	1.08	1.11	1.90

Table 4.3 Navigation Filter Results

Case	RMS of Position Errors in meters			
	x	y	z	3-axis
Random Noise	0.70	0.69	0.66	1.19
Selective Availability	17.84	17.01	17.91	30.47

Case	RMS of Velocity Errors in m/s			
	$\dot{x}$	$\dot{y}$	$\dot{z}$	3-axis
Random Noise	$7.35 \times 10^{-3}$	$5.14 \times 10^{-3}$	$3.89 \times 10^{-3}$	$9.78 \times 10^{-3}$

### Nadir Pointing Case

The true yaw, roll, and pitch generated by the nadir pointing case described above are shown in Figure 4.6. A plot of the SVD point solution errors are presented in Figure 4.7. Since errors for all three of the Euler angles are similar, the root-sum-square (RSS) of the errors has been computed to give a 3-axis attitude error. The root-mean-square (RMS) of the 3-axis errors for the SVD point solution is 0.084 degrees.

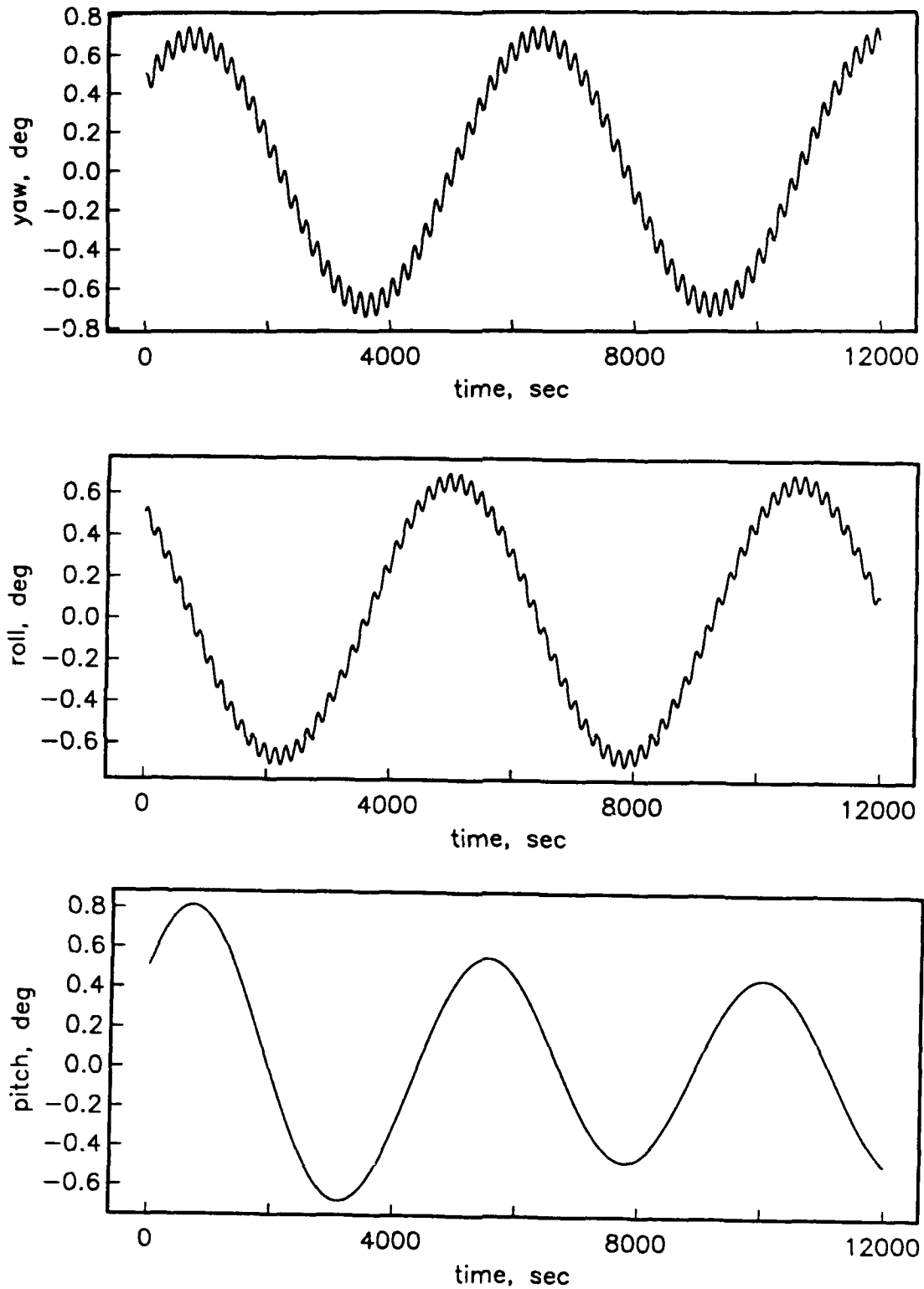


Figure 4.6 True Nadir Pointing Attitude Motion

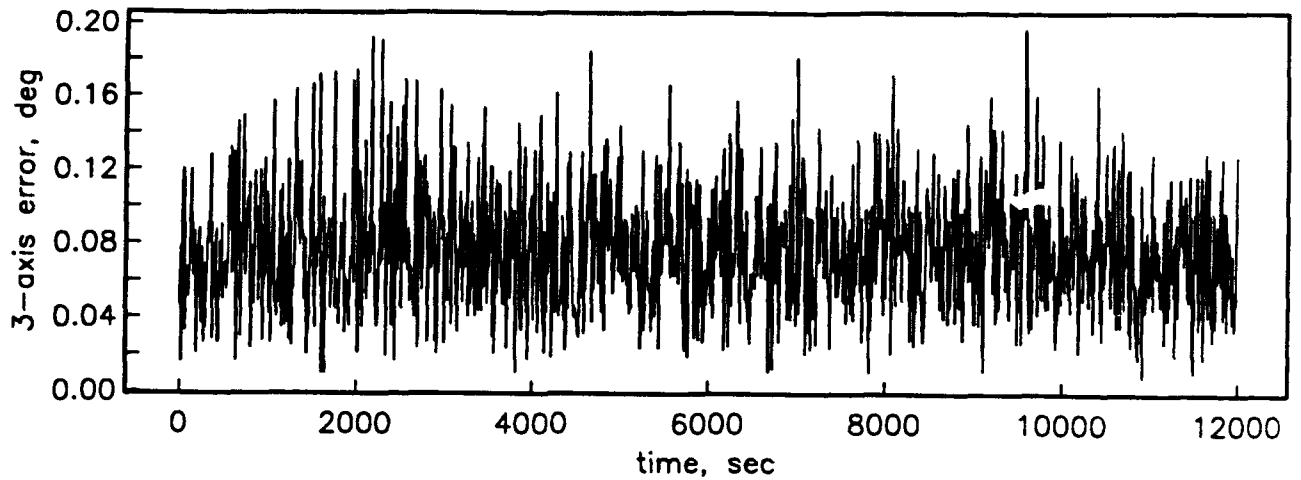


Figure 4.7 Nadir Pointing SVD Point Solution Errors. RMS = 0.084 deg

With a Kalman filter, however, this error can be improved since knowledge about the dynamics has been included. As we see in Figure 4.8, implementing the Euler angle filter lowers the RMS by a factor of three to 0.026 degrees. The quaternion filter results for this case are shown in Figure 4.9. (Although quaternions are used in the filter calculations, they have been converted to Euler angles on output for easier comparison.) As expected, the results are very similar to those generated by the Euler angle filter, the RMS being 0.0236 degrees.

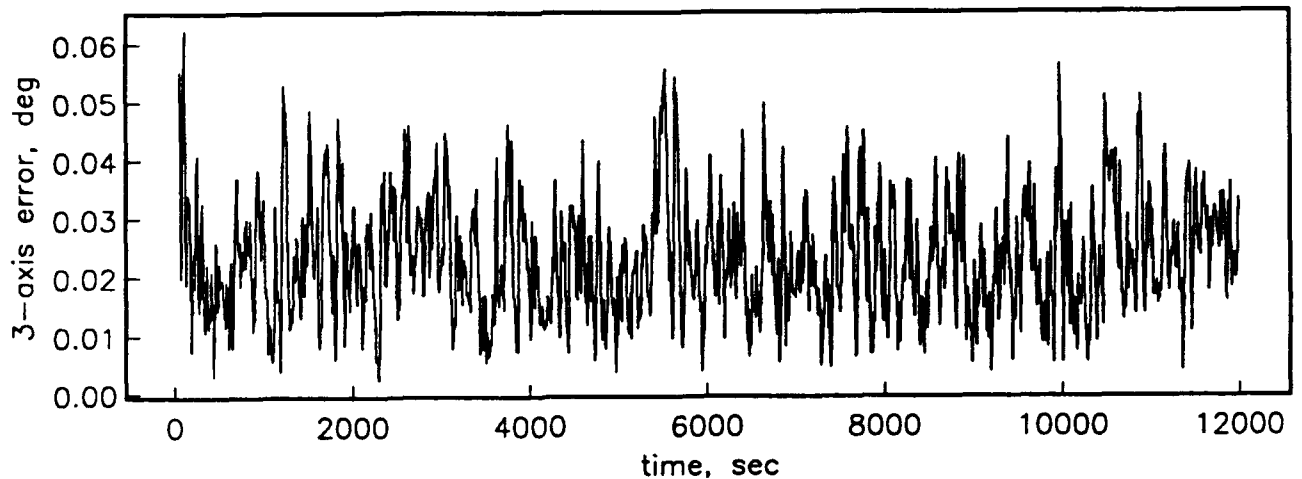


Figure 4.8 Nadir Pointing Euler Angle Filter Errors. RMS = 0.025 deg

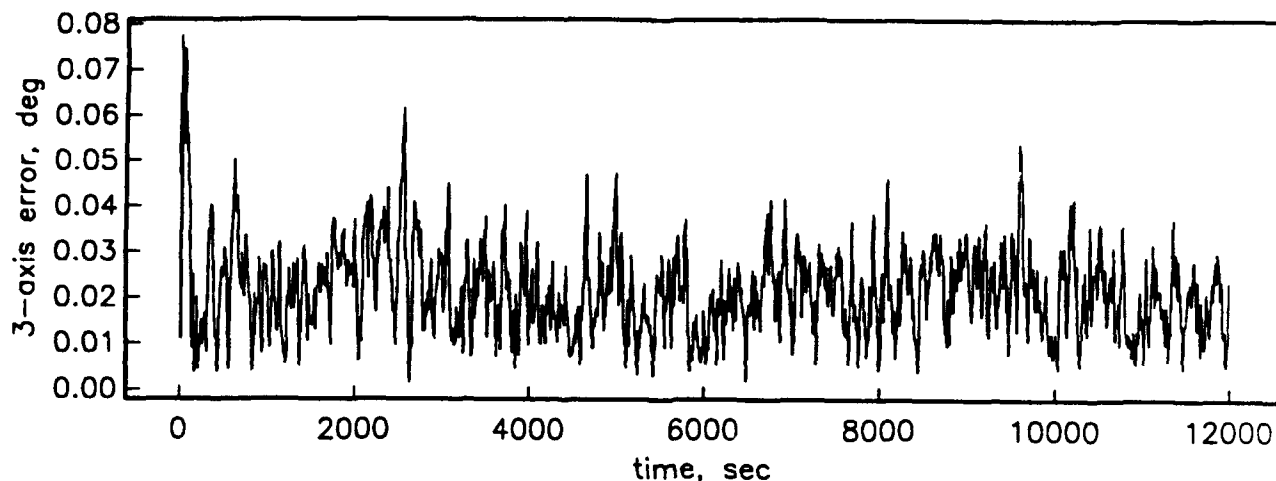


Figure 4.9 Nadir Pointing Quaternion Filter Errors. RMS = 0.0236 deg

#### Off-Nadir Pointing Case

The quaternion formulation is better than the Euler angle formulation in an off-nadir pointing scenario. For example, Figure 4.10 shows the true attitude motion using initial yaw, roll, and pitch angles of 3 degrees. With this scenario the RMS of the Euler angle filter 3-axis errors is 0.1064 degrees, while the RMS of the quaternion filter remains at 0.0235 degrees. The 3-axis errors resulting from this off-nadir pointing case are shown in Figures 4.11 and 4.12.

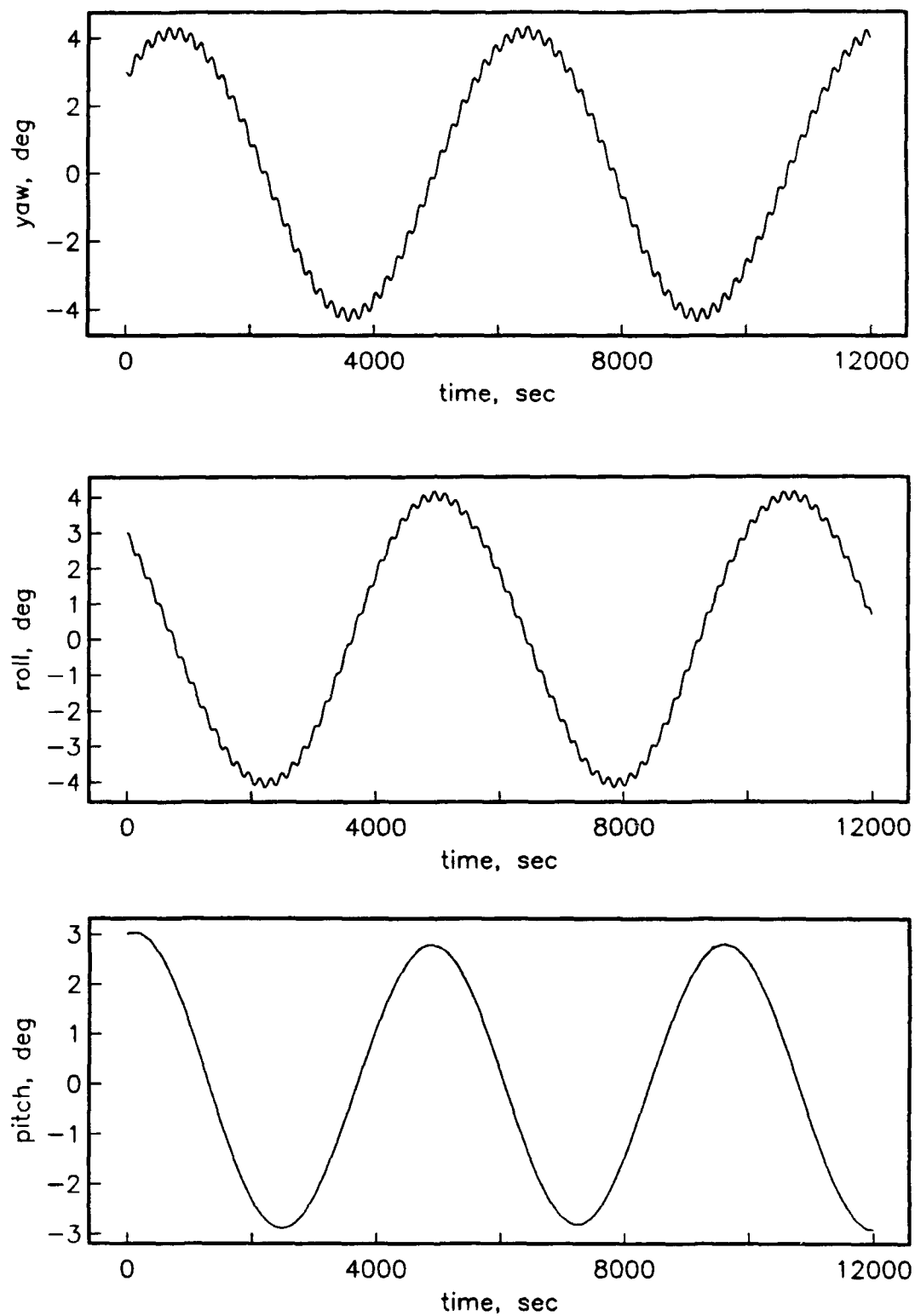


Figure 4.10 True Attitude Off-Nadir Pointing Case

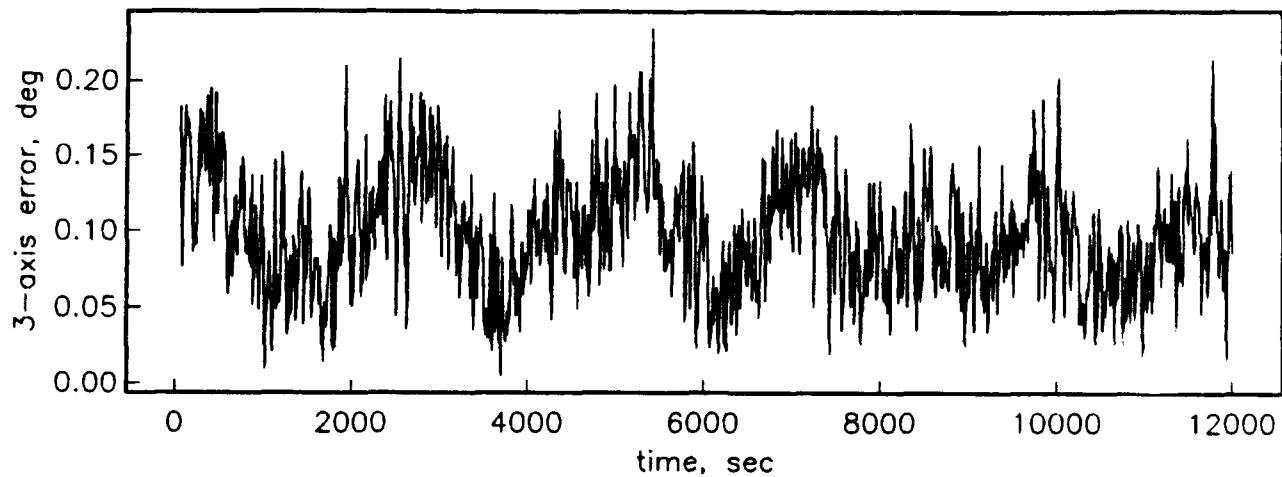


Figure 4.11 Off-Nadir Pointing Euler Angle Filter Errors. RMS = 0.1064 deg

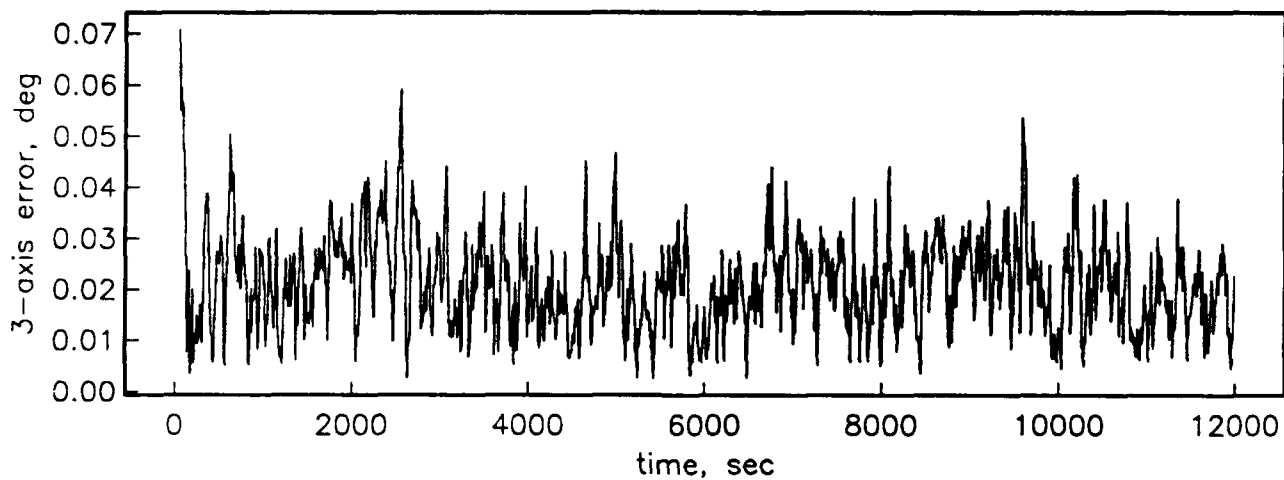


Figure 4.12 Off-Nadir Pointing Quaternion Filter Errors. RMS = 0.0235 deg

### Multipath Case

In the next case a multipath type error was added to the range difference measurements instead of adding only random noise. The inverse time constant was adjusted to  $1/300$  seconds<sup>-1</sup> corresponding to a time constant of 5 minutes. The RMS of the errors increases to 0.0876 degrees. Furthermore, in Figure 4.13 it is evident that the error is more structured in the multipath case than in the random noise case. In fact, the filter does not work much better than the SVD point solution as shown in Figure 4.14. This indicates that using this filter in a multipath environment has diminishing returns, and a better way of dealing with multipath is needed.

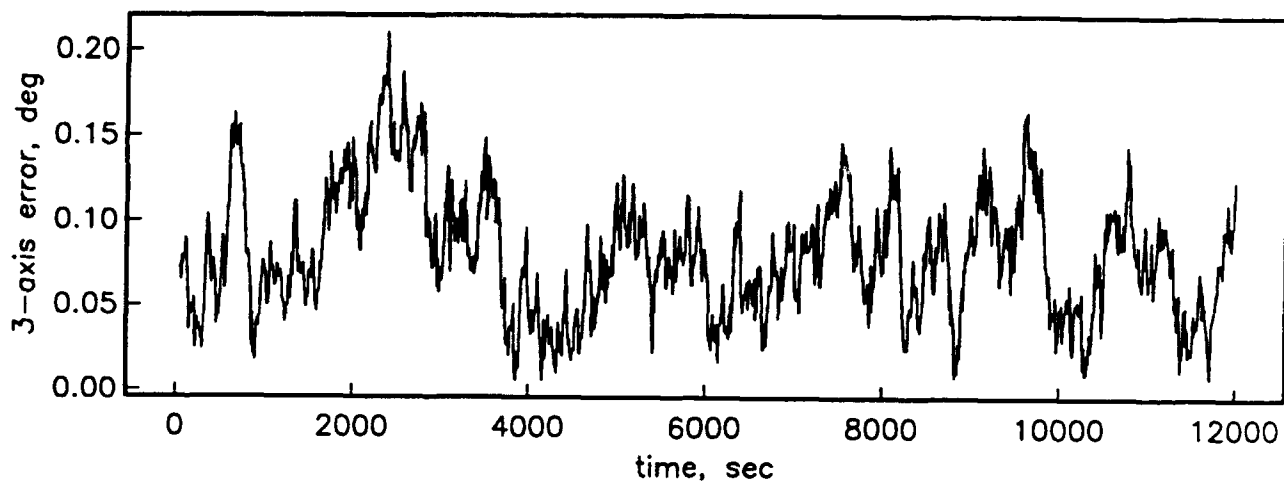


Figure 4.13 Multipath Environment Quaternion Filter Errors. RMS = 0.0876 deg

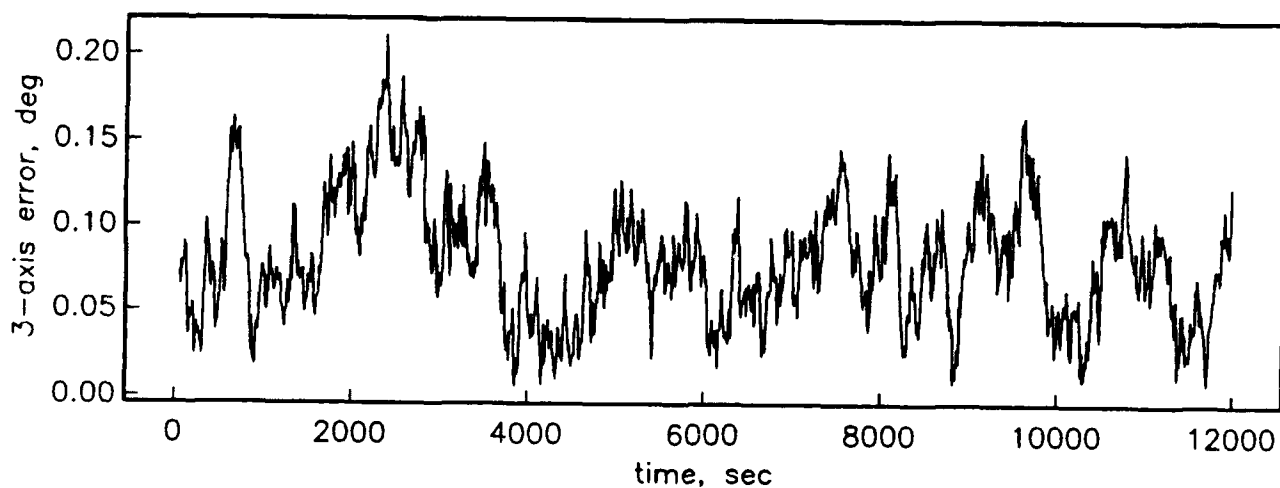


Figure 4.14 Multipath Environment SVD Point Solution Errors. RMS = 0.0877 deg

### Non-Optimal Baselines Case

Another factor which can degrade the performance of the attitude filter is poor antenna placement. In the nadir pointing case above the baselines are optimally placed in an orthogonal configuration. If the baselines are not optimally configured, the performance of the filter changes. Consider the baseline vectors illustrated in Figure 4.15 where  $b_1 = [1 \ 0 \ 0]^T$ ,  $b_2 = [0 \ 0 \ -0.5]^T$ , and  $b_3 = [0 \ 0 \ 0.5]^T$ . Using this baseline configuration we would expect the roll performance to be the best because it is observed by two baselines a 1 m and an 0.5 m baseline. The next best should be yaw which is observed by the two 0.5 m baselines. Finally the pitch axis is only seen by the long 1 m baseline. Figure 4.16 confirms this result. The RMS of the roll errors 0.0125 deg, while the RMS for the yaw and pitch errors are 0.0185 and 0.0229 , respectively. This was not a particularly bad configuration, but other more severe cases are certainly possible.

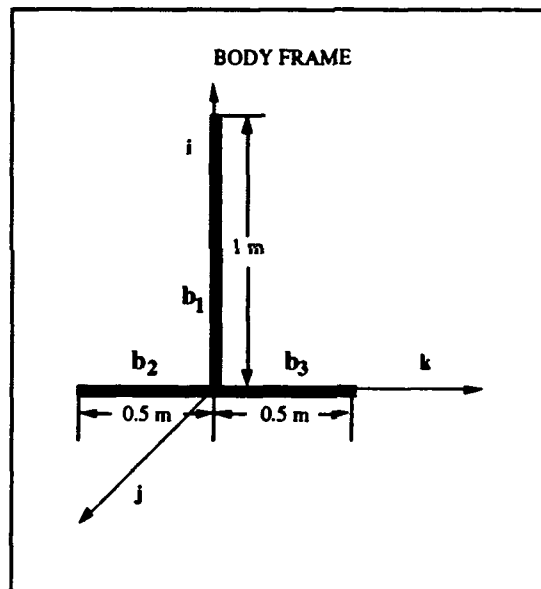


Figure 4.15 Non-Optimal Baselines

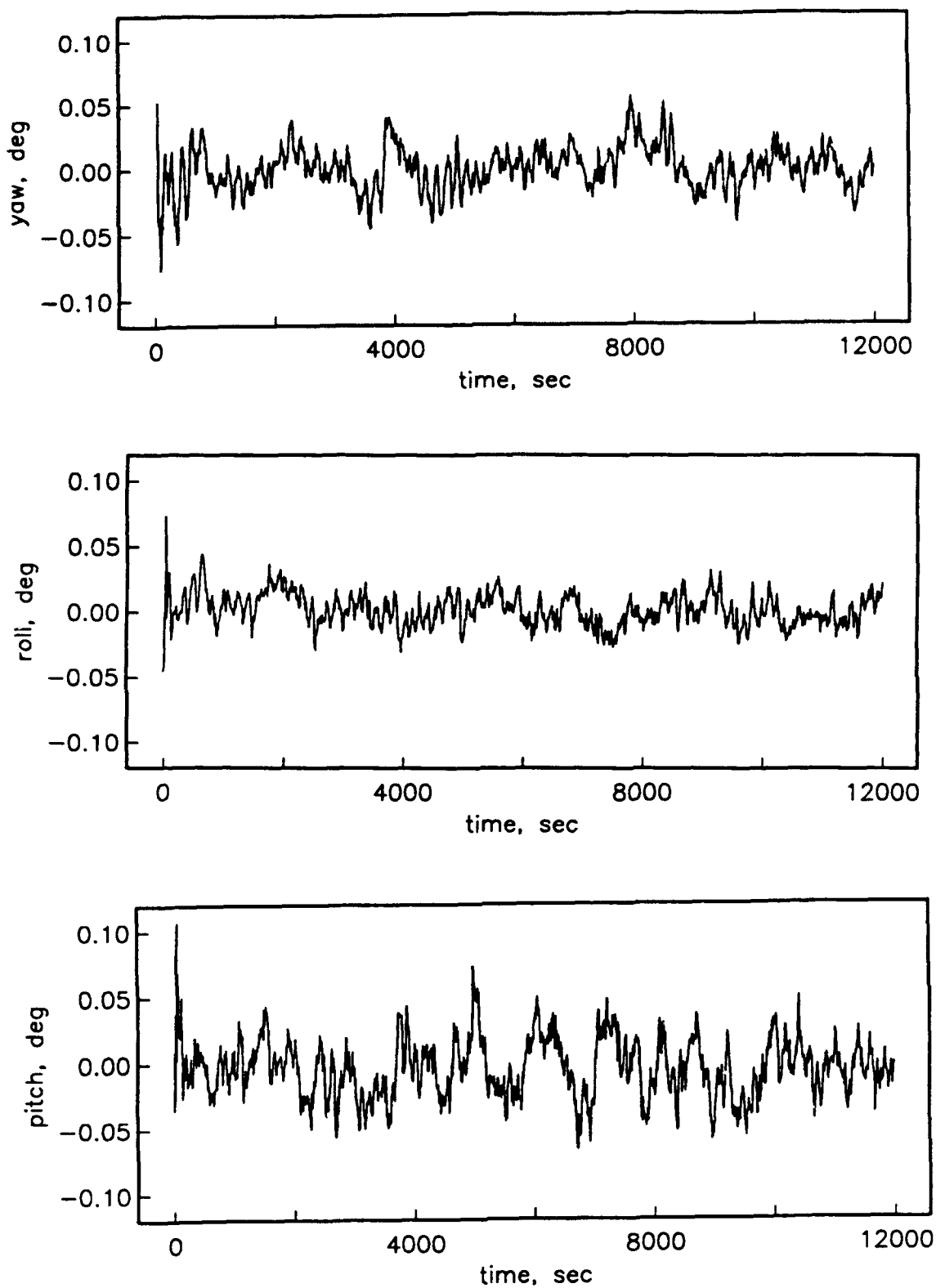


Figure 4.16 Non-optimal Baseline Configuration  
RMS(y) = 0.0185 deg; RMS(r) = 0.0125 deg; RMS(p) = 0.0229 deg

### Larger Mask Angle Case

The number of visible GPS satellites also affects the accuracy of the attitude solution. For instance, if the mask angle is increased to 15 degrees blocking off more of the GPS satellites, the RMS of the 3-axis error increases to 0.0363 degrees. We can see in Figure 4.17 that although spread of errors is greater than when the mask angle is zero, the character of result does not change.

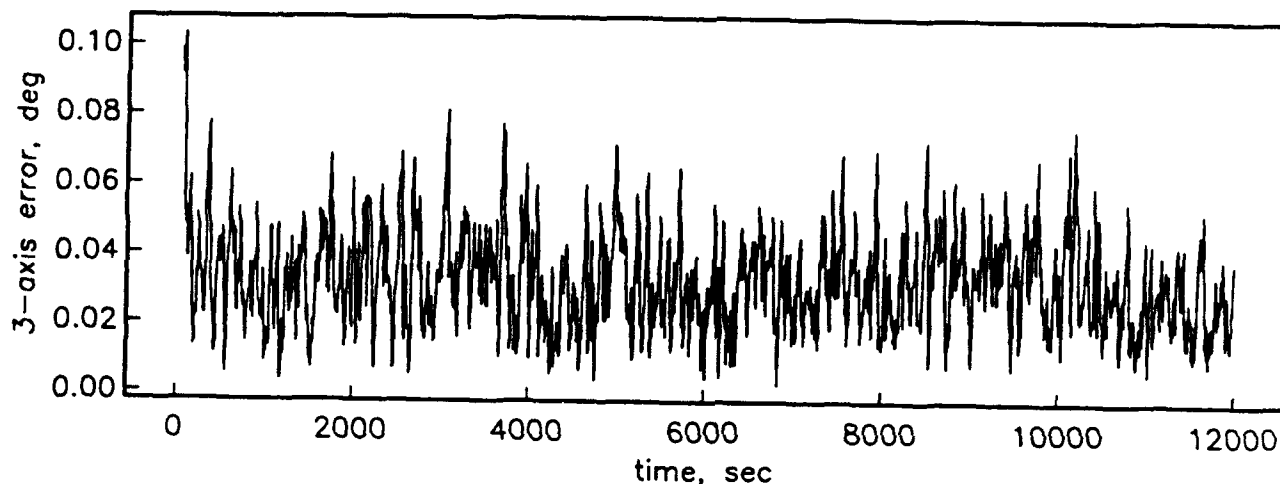


Figure 4.17 Larger Mask Angle. RMS = 0.0363 deg

### Navigation Filter with Random Noise

The results from the navigation filter for the nadir pointing case using random range measurement errors are presented in Figures 4.18 and 4.19. The  $x$ ,  $y$ , and  $z$  errors have been combined to give a 3-axis RSS position error and the  $\dot{x}$ ,  $\dot{y}$ , and  $\dot{z}$  errors have been combined to give a 3-axis velocity error. In this particular case the velocity measurements are better than the position measurements. Since the velocity and position states are coupled, the filter can rely more on the velocity measurements resulting in the apparent coloring of the position errors. The RMS of the position and velocity errors are 1.19 meters and  $9.78 \times 10^{-3}$  meters per second, respectively.

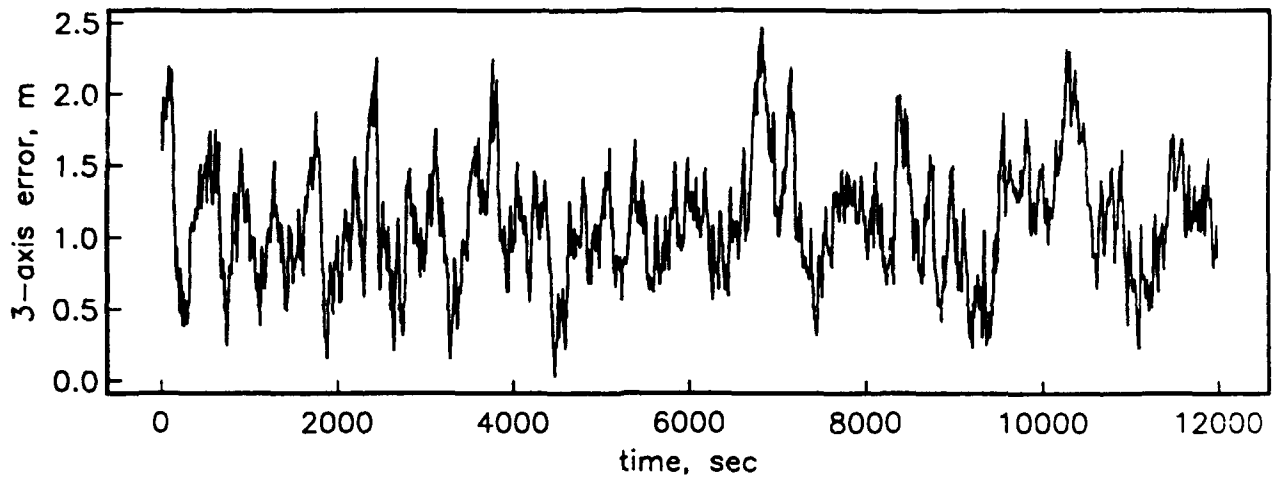


Figure 4.18 Random Noise Navigation Filter Position Errors. RMS = 1.19 m

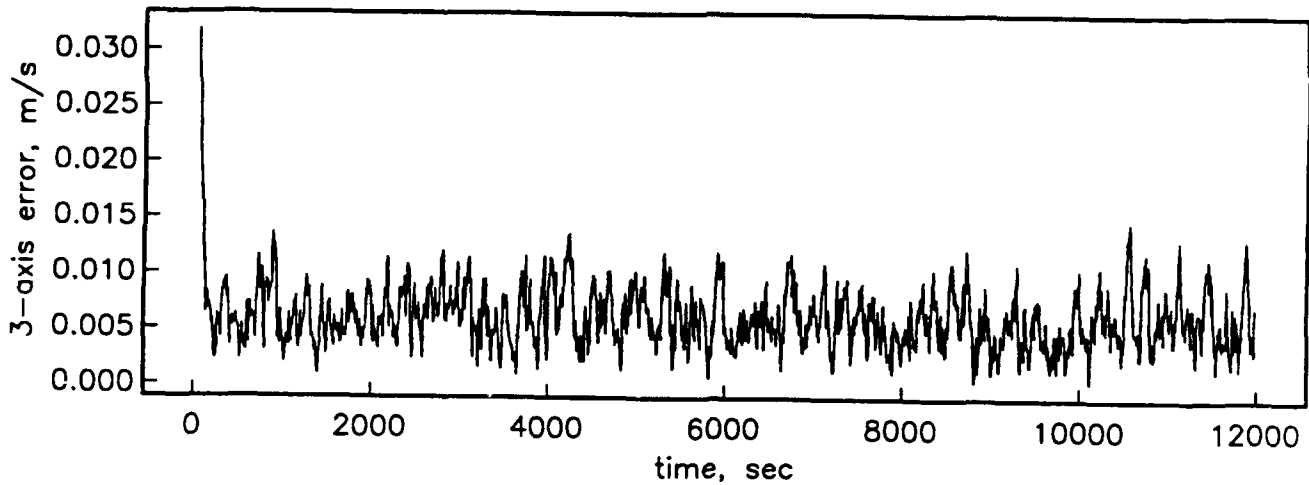


Figure 4.19 Random Noise Navigation Filter Velocity Errors. RMS =  $9.78 \times 10^{-3}$  m/s

### Navigation Filter with Selective Availability

If selective availability is included in the range measurement noise, the performance of the navigation filter worsens considerably. The average standard deviation of the errors for this case jumps to 30.5 meters, as demonstrated in Figure 4.20. But, even though the

position error is relatively high, the attitude solution can still be determined with accuracy as indicated by an RMS of the attitude errors of 0.019 degrees. To accommodate the 1 second interval ARIMA model, the measurement update interval here was changed to 1 second.

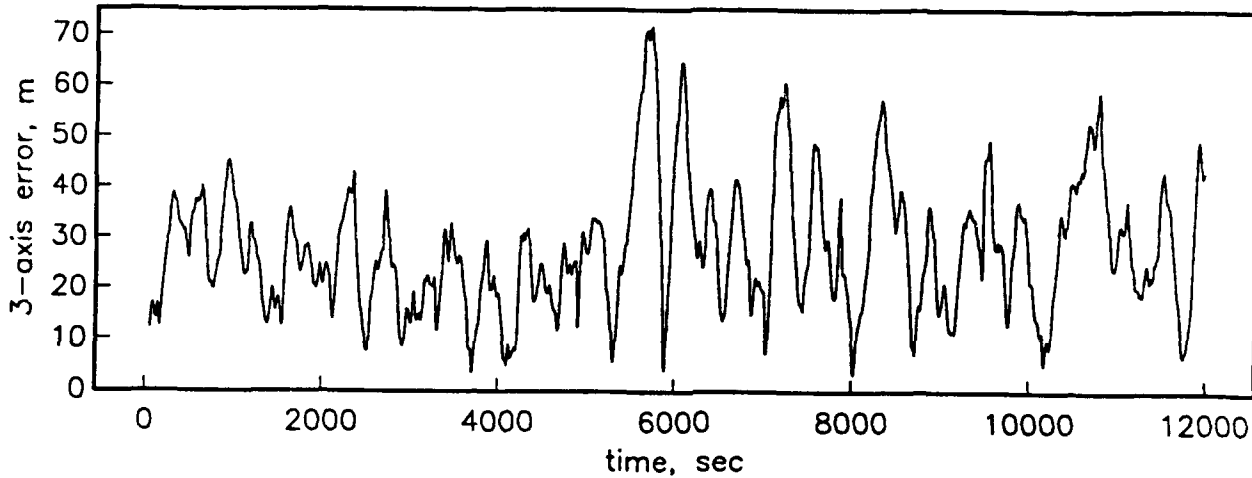
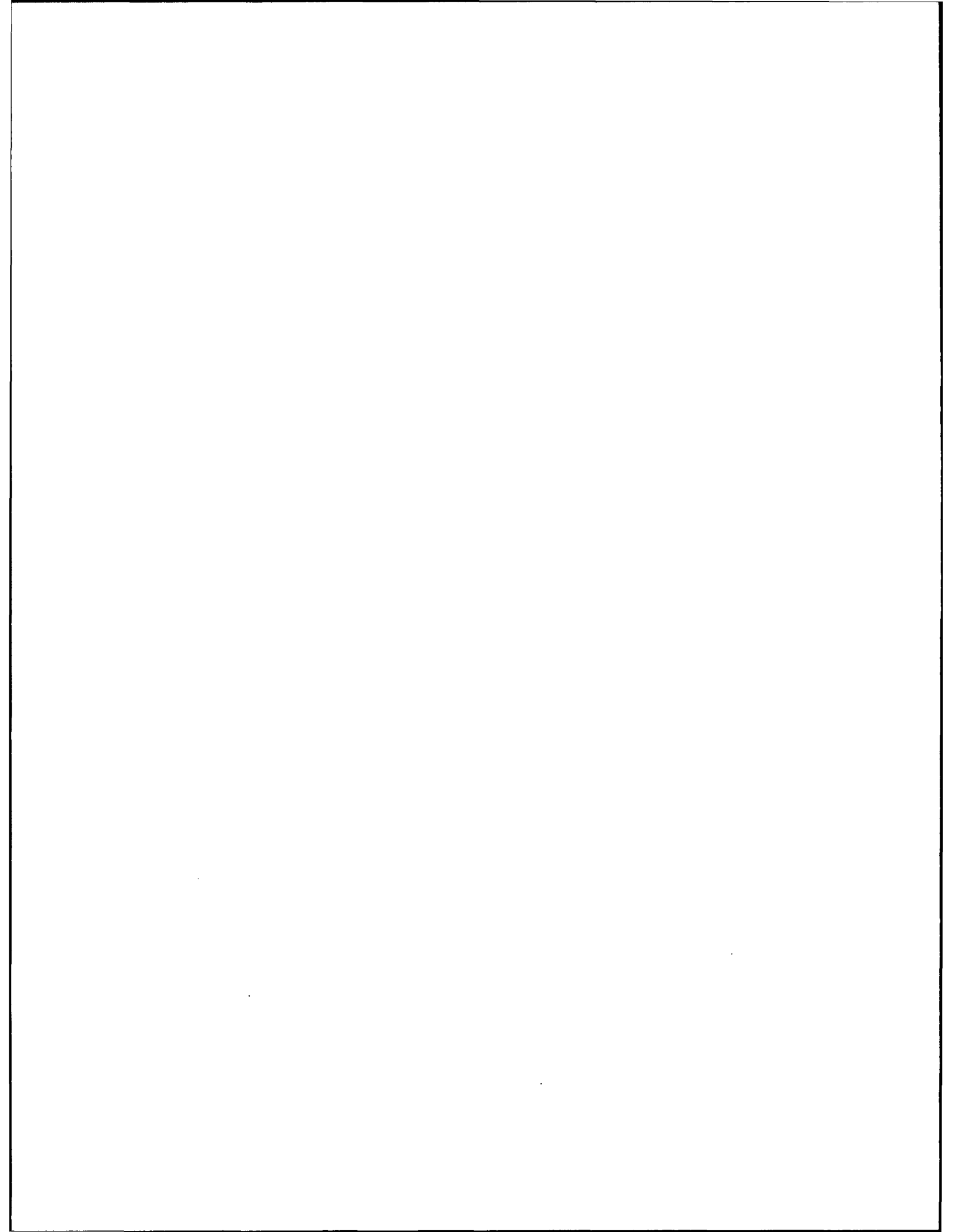


Figure 4.20 Navigation Filter Selective Availability Errors. RMS = 30.47 m

### Conclusions

Nominal instantaneous attitude accuracy was found to be at the level of 0.08 deg RMS for all three angles, based on the measurement models which we used. A factor of 3 improvement was gained by using a Kalman Filter in either implementation. The quaternion form was able to maintain this accuracy in off-nominal attitudes; however, thus far we have not considered changes in the satellite visibility due to changing vehicle attitude. This is certainly an area for future improvements.

The attitude filter solution degradation in the presence of even small multipath type reflections is worse than expected. In fact, it appears that there is no benefit to filtering in this case. We will continue to investigate both the assumptions and the models used, to make sure that the problem is accurately represented, and, if so, to try to develop techniques to improve performance.



## 5. Algorithms and Ground Testing

*Bruce C. Chesley*

This section describes algorithms, testing, and results for GPS based attitude determination on the ground. The algorithms and experiments address static attitude solutions, baseline survey, and integer ambiguity resolution. Before describing the ground algorithms and experiments, a summary of GPS attitude receivers and error sources is given. Note that many of the test descriptions and results have been previously presented by Axelrad and Chesley [1993].

### 5.1 Attitude Receiver Comparison

There is currently a great deal of interest in GPS based attitude determination in the navigation community. Several experiments have been conducted utilizing somewhat different approaches. The hardware configurations can be divided into two categories - those using multiple independent receivers (usually driven from a common oscillator), and implementations of a single receiver with multiple antennas. The single receiver versions have varying degrees of hardware integration.

Independent receivers - Currently, the most widely reported approach to GPS based attitude determination is to use two or more separate receivers to collect data from multiple antennas [c.f. Martin-Niera and Lucas, 1992; Lu, et al., 1993; Brown and Evans, 1990; Diefes, 1993]. The phase measurements from the receivers are processed together to eliminate common mode errors and solve for the antenna array orientation. Generally this requires an additional satellite to resolve the oscillator offsets between the receivers or to permit measurement double differencing to eliminate its effect.

The use of a common reference oscillator for all receivers may eliminate the need for an additional observation. However, depending on the design, the relative offset between the receivers is still subject to hardware dependent delays which can be a function of the receiver power up state or may vary due to differences in temperature or supply voltage. Thus, even in a common oscillator configuration, double differences are generally used for multiple receiver attitude determination.

Ashtech - The approach taken in the Ashtech 3DF receiver is to devote a separate hardware channel for each antenna baseline driven with a single oscillator. The hardware has been integrated into a single package, but the signal processing approach is essentially the same as the independent receiver approach described above. Sample testing of this receiver has been documented by Ferguson [1991], and Van Graas and Braasch [1991].

Texas Instruments - TI conducted several development tests of an attitude determination receiver that were reported by Brown and Ward [1990] and Brown and Evans [1992].

These tests used a modified AN/PSN-9 receiver, an off-the-shelf production model from TI. Their receiver used two identical units and a common local oscillator to provide time-aligned phase residuals. This is essentially the same approach adopted by Ashtech and various independent receiver attitude experiments.

**Adroit** - Adroit Systems Inc. has developed several versions of an attitude determination system for artillery alignment [Jurgens and Rodgers, 1991] and for land and marine vehicle heading determination [Diefes, 1993]. The original design was a set of three colinear antennas attached to a single receiver. Their newest product is composed of four independent receivers which collect data from antennas mounted on a small circular plate.

**Codeless Attitude Determination System** - Snyder and MacDoran [1993] at the University of Colorado have designed a single baseline yaw sensor for space applications based on codeless technology. The same approach could be extended to a full three axis system. The technique uses separate downconversion stages for each antenna driven by a common oscillator. In order to avoid multipath reflections from the vehicle, their design incorporates narrow beam antennas (about 100 deg field of view) rather than the typical hemispherical patch pattern.

**Trimble** - The Trimble Vector is currently the only receiver that employs a higher level of hardware integration than other approaches. The Trimble Vector is a six channel, C/A code, single frequency receiver which multiplexes among four antennas. The use of a single hardware processor and antenna multiplexing eliminates any changes introduced by independent hardware. Using shared hardware for all RF processing adds the complication of multiplexing antennas. This introduces difficulties in acquisition and integer tracking and reduces the effective signal to noise ratio of the received signal, but these issues have been adequately addressed in the receiver design.

The architecture for the Vector receiver is described in the Trimble Operations Manual [Trimble, 1993] and Cohen [1992]. The top-level design for the receiver is shown in Figure 5.1 [from Cohen, 1992, p.35]. The RF front end amplifies the signal from the antennas, down-converts the signal to an intermediate frequency of 4 MHz where it is digitally sampled and passed to the IQ correlator. Note that the signals from all four antennas are pass through the same RF section in the time-shared multiplexing scheme. From here the digital output for the master antenna and the three slave antennas are treated differently. The master antenna output drives the tracking loop filter which regulates the numerically controlled oscillator. All signals are referenced to this single local oscillator, and the oscillator runs open loop during the times when the slave antenna signals are being tracked. The outputs for the slave antennas are passed through a separate transfer function to produce the final differential phase output.

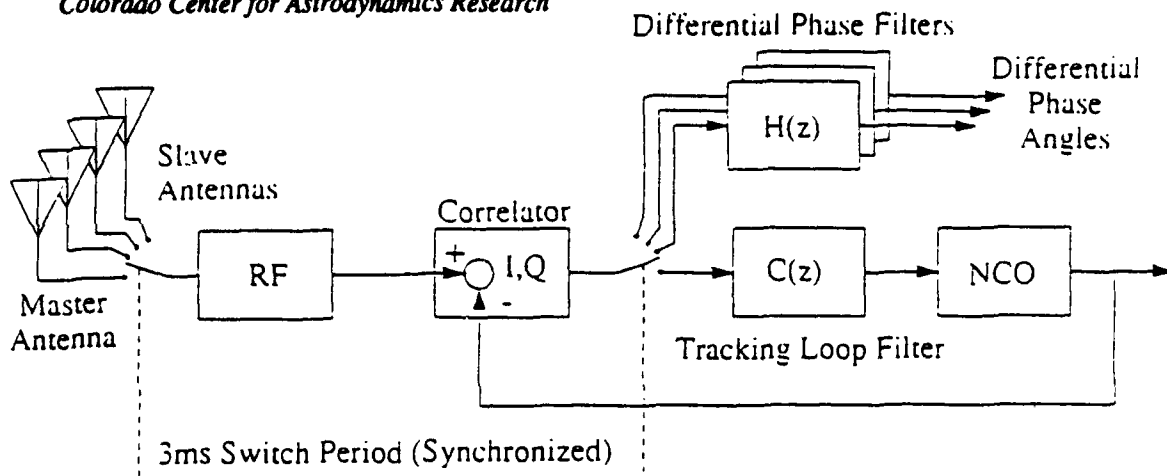


Figure 5.1. Top Level Receiver Architecture (from [Cohen, 1992, p. 35])

This receiver architecture is an effective signal processing design for measuring the differential phase residual. Nevertheless, errors are still present in the raw measurements. The principal sources of error for any multi-antenna GPS receiver are receiver biases, multipath, antenna cross-talk, antenna phase center motion. Receiver noise includes random measurement errors, tracking errors, antenna cross talk, and bias drifts due to temperature and voltage changes. Multipath and antenna phase center motion will be addressed further in Section 5.6. The receiver hardware design has been achieved such that the receiver errors are typically less than 2 mm while multipath errors can be as large as 5 mm [Braasch, 1992].

Trimble also manufactures an attitude receiver called Quadrex based on the same design as the Vector. The receivers are the same except that the Vector contains an additional internal board that generates attitude solutions without external processing. The Quadrex requires an external computer to form attitude solutions.

In summary, each approach has its own challenges. The use of independent receiver hardware is accomplished most efficiently with a single local oscillator, but there may be additional hardware biases introduced by temperature or voltage changes. The common hardware approach adopted by Trimble introduces additional complexities in the signal processing and reduces signal to noise ratio. Both these approaches have led to successful GPS based attitude determination systems with neither proving clearly superior to the other.

## 5.2 Least Squares Solution

The least squares algorithm generates a discrete, point solution (not filtered) for the optimal attitude at each measurement epoch. The Trimble Vector receiver can determine the vehicle attitude using a nonlinear least squares solution or the SVD solution for the Wahba problem, as discussed in Section 4.6. This section treats only the nonlinear least squares solution since this was the primary method used in subsequent ground tests.

The attitude solution relies on additional information that comes from an off-line baseline survey and resolution of the integer ambiguities. Once these quantities are known, the solution is found from the linear least squares equations,

$$H\delta\theta = \delta r \quad (5.1)$$

where

$$\delta r_{ij} = \Delta r_{ij} - \Delta \hat{r}_{ij},$$

$$H = \begin{bmatrix} \left( {}^B \hat{C}_0^N \ e_1^N \right)^T B_1^x \\ \vdots \\ \left( {}^B \hat{C}_0^N \ e_1^N \right)^T B_m^x \\ \left( {}^B \hat{C}_0^N \ e_2^N \right)^T B_1^x \\ \vdots \\ \left( {}^B \hat{C}_0^N \ e_n^N \right)^T B_m^x \end{bmatrix}$$

and  $\delta\theta = \left[ \delta\theta_1, \delta\theta_2, \delta\theta_3 \right]^T$

represents small angle rotations about the estimated body 1,2,3 axes.  $B^x$  is the baseline cross product matrix defined in Section 4. The attitude matrix estimate can be updated using  $\delta\theta$ , and the process is repeated until the changes get sufficiently small.

Recall, however, that the GPS attitude receiver measures the L-band phase difference between the master and each of the baseline antennas, rather than the range difference. If the range difference, phase difference, and baseline vectors are all described in cycles (1 cycle ~ 19 cm for the L1 frequency), the measured phase difference is just,

$$\Delta\phi_{ij} = \Delta r_{ij} - k_{ij} + \beta_i + v_{ij} \quad (5.2)$$

where  $k_{ij}$  is the integer ambiguity, or unknown number of whole cycles in the phase difference,  $\beta_i$  is a line bias associated with the receiver hardware, and  $v_{ij}$  represents measurement errors.

Thus, we can use Equation 5.2 to convert a GPS phase difference measurement to a range difference, if we know the line biases for each slave antenna ( $\beta_i$ , for  $i=1, \dots, m$ ) and the integer ambiguity for each satellite and slave antenna pair ( $k_{ij}$ , for  $i=1..m, j=1..n$ ). To use the range differences in an attitude solution we also require the baseline vectors in the body frame ( $b_i^B$ , for  $i=1, \dots, m$  baselines), and the line of sight vectors to the satellites in the navigation frame ( $e_j^N$ , for  $i=1, \dots, n$  satellites). The body frame and navigation frame are shown in Figure 5.2. The body frame has the x-axis along the velocity vector of the vehicle, z-axis pointing up, and y-axis perpendicular to both in a right-handed sense. The navigation frame is simply the earth-based local level frame expressed in East, North, Up components.

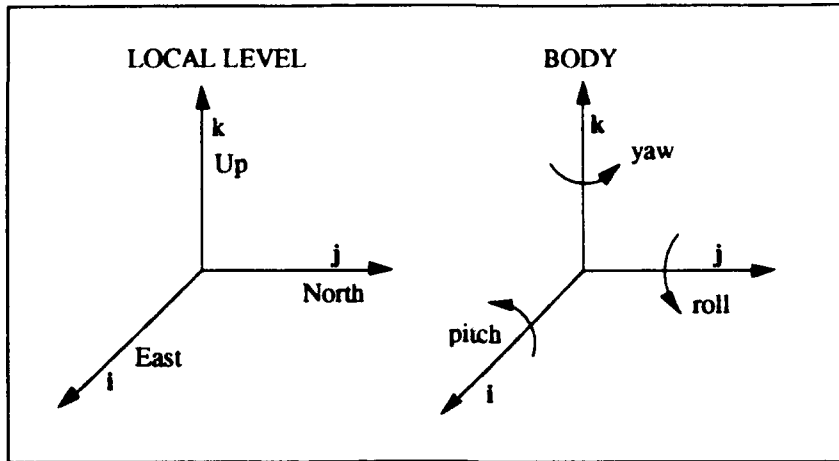


Figure 5.2 Navigation and Body Fixed Reference Frames for Ground Tests

Note that the least squares cost function in Equation 5.1 assumes the baseline vectors are known and that differential range measurements are available. The next section addresses how the baseline vectors and differential range values are derived. If the baseline vectors are known (and assumed fixed) and differential range measurements are available from the receiver (i.e., the integer ambiguities are resolved), then only two satellites are needed to form attitude solutions. This can be seen by examining the least squares equation,

$$H \delta \theta = \delta r \quad (5.3)$$

The size of  $H$  is  $mn \times 3$ ,  $\delta r$  is  $mn \times 1$ , and the size of  $\delta \theta$  is  $3 \times 1$ . For three non-coplanar baselines ( $m=3$ ) with at least two non-coincident satellites in view ( $n=2$ ), the system is overdetermined. If the baselines are coplanar, the system still can be overdetermined as long as the satellites do not lie in the plane of the baselines.

### 5.3 Baseline Survey

The current implementation of the solution algorithm for the Trimble receiver requires three distinct steps: 1) static baseline survey, 2) integer ambiguity resolution, and 3) real time attitude solutions. This section describes a static baseline survey and line bias solution technique.

The survey is required to define the baseline vectors in body coordinates ( $\mathbf{b}_i^B$ ) and to determine the line bias for each slave antenna ( $\beta_i$ ). The geometrical baseline vectors could be measured with a ruler; however, they are not necessarily coincident with the electrical baselines. In addition because of the need to determine the line bias, the GPS static survey is a convenient means for establishing both the vectors and line biases. To perform a survey, the vehicle must be static while data is collected from several satellites over about 6-10 hours. Long satellite arcs are required to separate the line bias from the baseline components.

If the satellite line of sight vectors used in the survey are expressed in East, North, Up (ENU) components, the survey will solve for coordinates of each slave antenna relative to the master in a local level or navigation frame. To transform them to the body frame, the vehicle must be aligned in a known (or defined) direction relative to the local level. The transformation matrix relating the two frames may be defined by calibration or by assuming that the vehicle is aligned in a given direction.

The Vector survey software\* takes the latter approach. It assumes that the vehicle is level, i.e. roll and pitch are zero, with baseline 2 serving as the heading reference. Thus, once the baseline vectors are determined in the local level frame, the transformation to body coordinates corresponds to a single rotation (yaw) about the vertical to align baseline 2 with true North.

Each master-slave baseline may be solved independently. The number of unknowns which must be determined is  $(N+3) - 3$  baseline components of the vector,  $\mathbf{b}_i$ , and one (ambiguity+line bias) for each of the satellites tracked. The ambiguities are not really of interest, but the common fractional part determines the hardware line bias. The normal equations are formed by stacking differential phase measurements to each of the satellites over time. Of course, the sequence of the equations does not matter so they can be grouped conveniently by satellite as follows,

$$\mathbf{Ax} = \delta\mathbf{r}$$

where for  $n$  satellites,

$$\mathbf{A} = \begin{bmatrix} \begin{matrix} e_1^T(t_0) & 1 & 0 & \dots & 0 \\ e_1^T(t_1) & 1 & 0 & \dots & 0 \\ \vdots & & & & \\ e_1^T(t_{N_1}) & 1 & 0 & \dots & 0 \end{matrix} \\ \vdots \\ \begin{matrix} e_n^T(t_0) & 0 & 0 & \dots & 1 \\ e_n^T(t_1) & 0 & 0 & \dots & 1 \\ \vdots & & & & \\ e_n^T(t_{N_n}) & 0 & 0 & \dots & 1 \end{matrix} \end{bmatrix}, \quad \mathbf{x} = \begin{bmatrix} b_{i1} \\ b_{i2} \\ b_{i3} \\ (k_1 + \beta) \\ \vdots \\ (k_n + \beta) \end{bmatrix}, \quad \delta\mathbf{r} = \begin{bmatrix} \Delta\phi_1(t_0) \\ \vdots \\ \Delta\phi_1(t_{N_1}) \\ \vdots \\ \Delta\phi_n(t_0) \\ \vdots \\ \Delta\phi_n(t_{N_n}) \end{bmatrix} \quad (5.4)$$

where  $N_i$  is the number of measurements collected for satellite  $i$ .

Each row of the  $\mathbf{A}$  matrix contains a line of sight vector to one of the satellites and a "1" in the column corresponding the integer+bias for the particular satellite. The hardware or line bias,  $\beta$ , is defined to be between 0 and 1, and is taken to be the mean (on a unit circle) of the fractional parts of  $(k_1 + \beta)$  through  $(k_N + \beta)$ .

\* The prototype version which runs on an external computer is called "SRVYTEST". It stores a file called survey.ram which contains the baselines and line bias values.

In the current implementation, several hours of phase measurements are typically processed to allow enough satellite motion to reliably estimate the fractional hardware delay. We hope that future implementations of this algorithm will estimate the baseline vectors and possibly the line biases in real time, eliminating the need for an off-line self survey. This would be valuable for spacecraft applications since antenna configurations computed from a pre-launch survey could change slightly due to stress and vibrations encountered during launch and deployment. Furthermore, line biases may drift in the space environment in ways not accounted for in a pre-launch survey. Another advantage of estimating the baseline vectors in real time is that baselines might deliberately change if antennas are placed on articulating appendages such as solar panels. In this case, it may be possible to estimate parameters related to vehicle configuration as well as vehicle attitude. This topic is highlighted as an area for future research.

### 5.4 Integer Ambiguity Resolution

Computing the integer ambiguities associated with each antenna and satellite is a challenging problem. The software provided with the Trimble Vector implements a motion based approach, as described in Cohen [1992] and Cohen and Parkinson [1992a]. The algorithm for integer ambiguity resolution based on large angle motion requires the changes in the baseline vectors be accumulated to solve for the baseline vectors. A single baseline change for an arbitrary number of baselines is shown in Figure 5.3. The large angle motion approach is based on the observation of changes in the differential range between antennas expressed as:

$$(\Delta r_{ij} - \Delta r_{ij0}) = \hat{e}_j^T \Delta \mathbf{x}_i \quad (5.5)$$

At each epoch  $\Delta \mathbf{x}_i$  must be solved for each of the  $m$  baselines by forming a solution using a minimum of three satellites in view and assuming the line of sight vectors are constant for the short time period considered. This can be expressed in matrix form as:

$$\begin{bmatrix} \Delta r_{1i} - \Delta r_{1i0} \\ \vdots \\ \Delta r_{ji} - \Delta r_{ji0} \end{bmatrix} = \begin{bmatrix} \hat{e}_1^T \\ \vdots \\ \hat{e}_j^T \end{bmatrix} \Delta \mathbf{x}_i \quad (5.6)$$

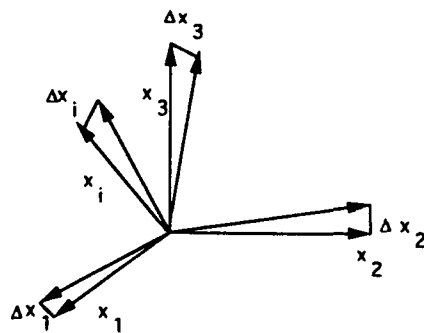


Fig. 5.3. Baseline Changes for Ambiguity Resolution

Cohen [1992] points out that the constraint on the entire baseline structure can be used to resolve the integer ambiguities. Since the baselines are fixed (both in length and relative orientation),

$$\mathbf{x}_i(t_1)^T \mathbf{x}_j(t_1) = \mathbf{x}_i(t_0)^T \mathbf{x}_j(t_0) \quad (5.7)$$

for each pair of  $i$  and  $j$ .

If we express baseline  $i$  at  $t_1$  as  $\mathbf{x}_i(t_1) = \mathbf{x}_{i0} + \Delta\mathbf{x}_i(t_1)$ , then

$$\begin{aligned} \mathbf{x}_i(0)^T \mathbf{x}_j(0) &= [\mathbf{x}_i(0) + \Delta\mathbf{x}_i(t_1)]^T [\mathbf{x}_j(0) + \Delta\mathbf{x}_j(t_1)] \\ \Delta\mathbf{x}_i(t_1)^T \mathbf{x}_j(0) + \Delta\mathbf{x}_j(t_1)^T \mathbf{x}_i(0) &= \Delta\mathbf{x}_i(t_1)^T \Delta\mathbf{x}_j(t_1) \end{aligned} \quad (5.8)$$

We need to find  $\mathbf{x}_i(t_0)$  and  $\mathbf{x}_j(t_0)$  in order to solve for the integer ambiguities. We have computed  $\Delta\mathbf{x}_i$  from Equation 5.5, so we can combine  $N$  measurements from 20-60 epochs in matrix form to solve

$$\begin{bmatrix} \Delta\mathbf{x}_l^{(1)T} \\ \vdots \\ \Delta\mathbf{x}_l^{(N)T} \end{bmatrix} \mathbf{x}_m + \begin{bmatrix} \Delta\mathbf{x}_m^{(1)T} \\ \vdots \\ \Delta\mathbf{x}_m^{(N)T} \end{bmatrix} \mathbf{x}_l = - \begin{bmatrix} \Delta\mathbf{x}_l^{(1)T} \Delta\mathbf{x}_m^{(1)} \\ \vdots \\ \Delta\mathbf{x}_l^{(N)T} \Delta\mathbf{x}_m^{(N)} \end{bmatrix} \quad (5.9)$$

where superscripts in parenthesis denote each epoch. These equations can be combined into a single linear least squares equation of the form  $Ax=B$  to solve for the baseline vectors,  $x$ . The specific formulation of this single equation depends on the number of baselines used.

Once the initial baseline vectors are known each of the  $k_{ij}$  terms can be found using  $\Delta r_{ij}$  and the precomputed  $\beta_i$  from Equation 5.2.

$$\Delta\phi_{ij} \approx \Delta r_{ij} - k_{ij} + \beta_i$$

where the noise term  $v_{ij}$  has been assumed to be zero.

The ambiguities are then rounded to integers and the standard solution algorithm can begin.

The Trimble Vector receiver uses the large angle integer resolution approach based on the information from the static self survey to initiate the attitude solution. During normal operation, the integers are regularly recomputed to enable new satellites to be brought into the solution and to verify the current integer values. If the residuals are found to be too large, the algorithm will "bump" them to reduce the residuals to an acceptable level.

### 5.5 Ground Testing Configuration

Ground testing of the Trimble Vector receiver was conducted under both static and dynamic (spinning) conditions. The tests focused on measurement quality, static self-survey, static attitude solution accuracy, and dynamic performance on a spinning platform. Before addressing the specific experiments, the test beds will be described. Each test bed consisted of a site, an antenna platform, and known reference points to verify accuracy.

#### Test locations

Two locations were used for ground testing --the roof of the Engineering Center, and Table Mountain. The roof of the Engineering Center at the University of Colorado consists of a flat area approximately 60 x 100 m (see Figure 5.4). The view of the sky is partially obstructed to the southwest by the tower of the Engineering Center and adjacent buildings. Many antennas and metal structures are co-located on the roof, making it a very noisy environment for multipath. (However, it was quite convenient.)



Fig. 5.4. Engineering Center Roof and x Structure

The other test location used was Table Mountain, shown in Figure 5.5. Table Mountain is a large flat mesa north of Boulder, Colorado, controlled by the U.S. Department of Commerce. The area used was largely free of multipath reflectors and contained surveyed reference points.

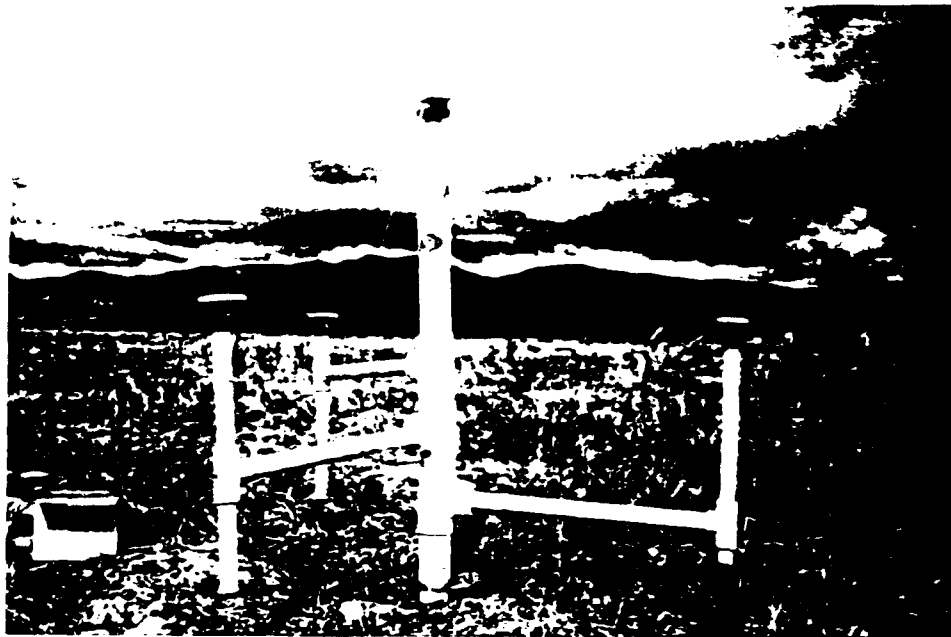


Fig. 5.5 Table Mountain Site and Tree Structure

### Antenna Platforms

Four antenna platforms were used for receiver testing. Each platform was tailored for a particular purpose in the testing program. The platforms will be referred to as the x structure, the tree structure, the one-armed spinner, and the wooden pallets.

The x structure is constructed from two aluminum cross members, each 1-m long as shown in Figure 5.4. The master antenna is raised on spacers that are approximately 10 cm long to prevent all four antennas from being coplanar. A small diode laser can be mounted at the center of the two cross members for absolute accuracy tests. The x structure was used in early tests, but it suffered from several shortcomings --the baselines were too short; the antennas were too close to coplanar; the arms were too flexible; and the structure itself was a multipath reflector.

The tree structure shown in Figure 5.5 was designed to address the problems with the x structure. It has a center mounting pole for the master antenna and three one-meter arms for the slave antennas. The center pole and baseline 2 define the body coordinate system. The arms can be moved to change the relative height and orientation of the slave antennas. The structure is fabricated using Schedule 40 PVC pipe. This material was chosen because it was thought to have several advantages [Comp, et al., 1993] -- greater rigidity, preventing significant flexure during the tests; lighter weight, permitting easy relocation and storage; and transparency to L-band GPS signals. The small diode laser was mounted below the baseline 2 antenna for absolute accuracy tests. Note that the three antenna baselines shown in the photograph are nearly orthogonal with the master antenna at the vertex of the orthogonal set. This nearly orthogonal configuration provides the best sensitivity to changes in attitude for all three axes. Field experience showed that the tree structure was not as rigid as originally hoped, thus suggesting the area of attitude determination for non-rigid structures as an area for future research.

The one-armed spinner structure was designed to mount on an existing spinning platform. The structure consists of a single master-slave antenna pair mounted on a PVC center pipe and a single 1 meter long PVC pipe arm. The arm was fitted to a cylinder mounted on the spin table. The table is driven by a DC motor which has a variable power supply that can be used to regulate spin rate. The receiver, power supply, and data collection computer are all stored inside the cylinder during testing. The configuration is shown in Figure 5.6.

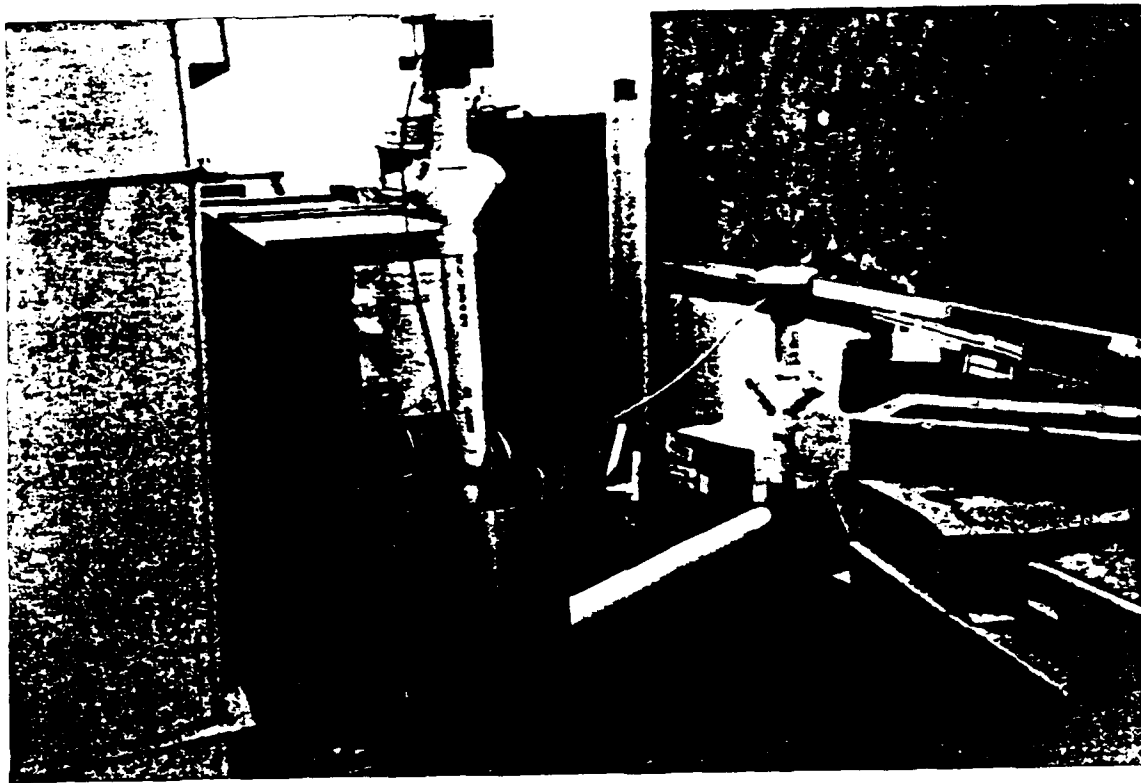


**Fig. 5.6 One-Armed Spinner Structure**

The wooden pallets were used for tests where antenna location and orientation had to be maintained precisely from one day to the next. Two wooden pallets were placed approximately 3 m apart on the flat roof of a low building at Table Mountain. This eliminated any structural flexure that may have been present in the other test structures. The master antenna was mounted to one of the pallets with C-clamps, and two slave antennas were mounted to the other pallet. Figure 5.7 shows the pallet configuration at Table Mountain.

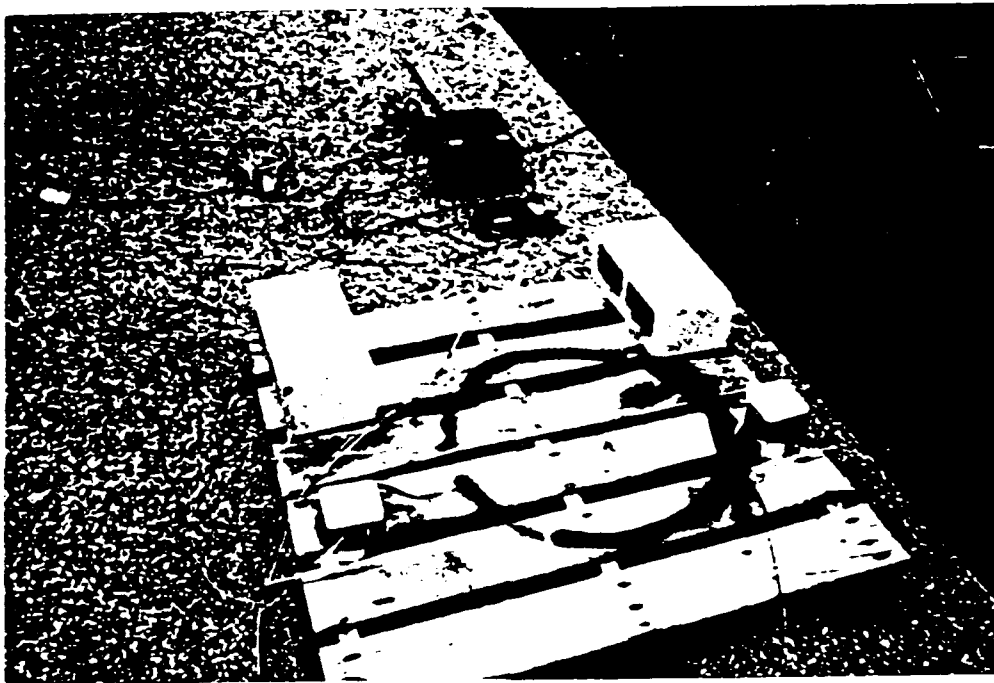


**Fig. 5.7 Wooden Pallet Structure**

**Reference Points**

Known control points at the Table Mountain test site provided a ground truth reference for attitude tests. Table Mountain has been used by UNAVCO for training personnel in GPS surveying techniques [Roberts, 1990; UNAVCO, 1993]. The vectors connecting the control points establish known directions in an Earth fixed or local level coordinate system. Absolute attitude determination accuracy using GPS may be evaluated by centering the structure on one control point and aligning it with another. For the relative and absolute accuracy tests described below, the antenna structure was placed at the base point shown in Figure 5.8. The coordinates of the other points relative to the base point are shown in Table 5.1.

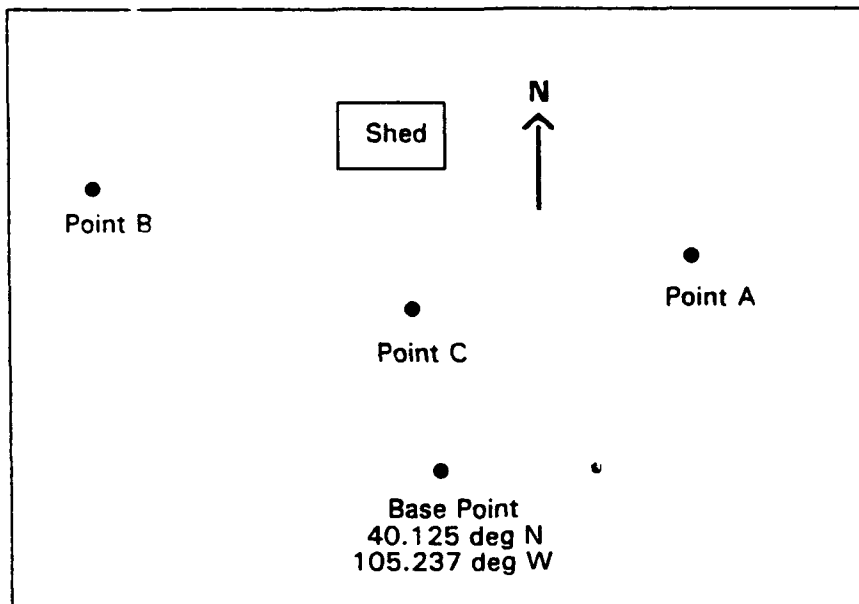


Fig. 5.8 Table Mountain Control Points

Table 5.1 - Relative Positions of Control Points from Mount (from [UNAVCO, 1993]).

SITE	EAST (m)	NORTH (m)	UP (m)	AZ (deg)	EL (deg)	RHO (m)
A	35.667	36.451	-0.544	44.376	-0.612	51.001
B	-41.922	55.465	1.029	322.917	0.842	69.533
C	-3.551	34.879	0.273	354.186	0.446	35.061

### Basic Operations

To initialize attitude operation, the equipment is set up as shown in Figure 5.9. The equipment consists of the Trimble receiver, power supply, computer, and an appropriate antenna mounting structure. Receiver initialization commands are issued from the computer. The structure is then rotated by about 90 degrees to resolve the integer ambiguities, and the attitude solutions are then initialized. Data files are stored containing the raw differential phase information, direction cosines for each of the tracked satellites, and attitude, position, and velocity solutions. The time interval for storage is internally set to 0.5 seconds by the receiver, but this value may be adjusted by the user.

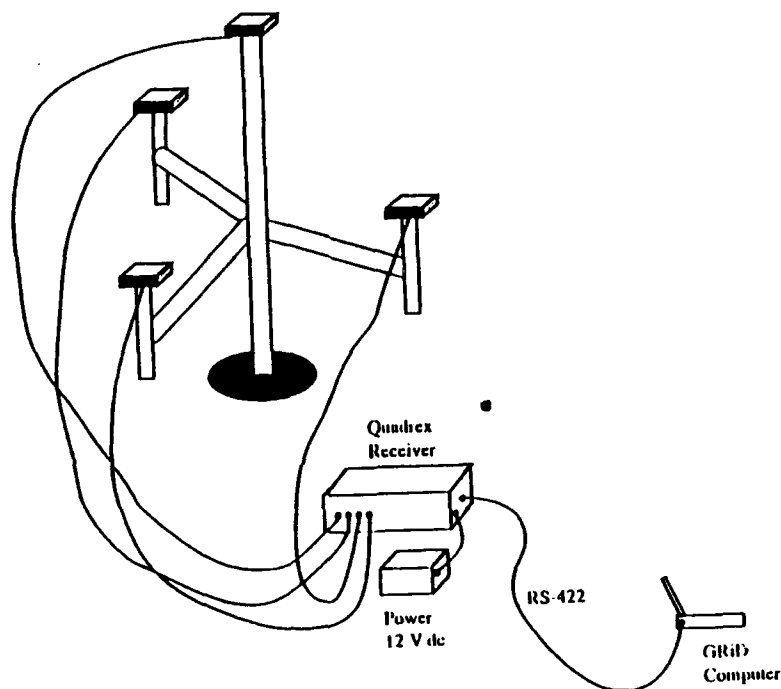


Fig. 5.9. GPS Receiver and Test Structure Configuration

### 5.6 Phase Measurement Quality

The characteristics of the phase residuals were examined to determine the quality of the raw measurements. Multipath and antenna phase center migration, potentially the two largest error sources, were considered separately in assessing overall measurement quality. Multipath effects were studied through both experiments and modeling.

The quality of the raw differential phase observations can be assessed by removing the effect of satellite motion leaving only the "phase residual". If the location and orientation of the baseline is known, the effect of the satellite motion can be computed based on this information and the transmitted satellite ephemerides. This predicted phase difference is subtracted from the observed phase difference to form the residual. If the orientation is not known, a polynomial of second or third order (depending on the length of the data

set) may be removed to detrend the data. The latter method was used in most of the results presented here.

### Multipath Testing

Figure 5.10 shows the satellites in view for a data set collected on May 9, 1993. The test was conducted at Table Mountain using the tree structure. Figure 5.11 illustrates measurement residuals for GPS satellite 2 from each of the three baselines. As shown in the figure, the random, or noise-like error in the observed residuals was on the order of 2 mm,  $1-\sigma$ . Over the 1.4 meter baseline used in the tree structure, this would produce a pointing error of less than 0.1 degrees. These extremely good results can be attributed to the high elevation (shown in Figure 5.10) for this satellite.

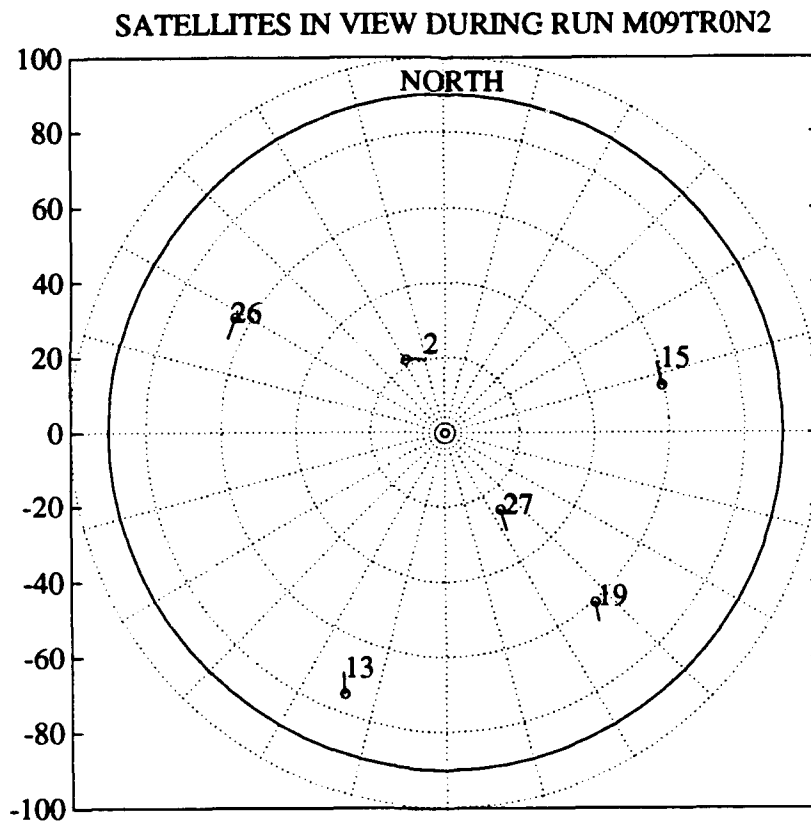


Fig. 5.10. Azimuth-Elevation Plot of Satellites in View for Test at Table Mountain, 9 May 1993. Radial distance represents satellite zenith angle ( $90 \text{ deg} - \text{elevation}$ ). Shaded hemisphere indicates the position of a large metal dome.

Systematic errors can also be observed in some of the phase residual data. Figure 5.12 illustrates the results for satellite 13 during the same May 9, 1993 test. From Figure 5.10 it can be seen that satellite 13 was at an elevation angle of only about 15-20 degrees. In addition, it was in the direction of a large metal dome at the test site. Systematic errors such as these are probably due to multipath reflection of satellite signals from nearby objects or variations in the phase center of the microstrip antennas.

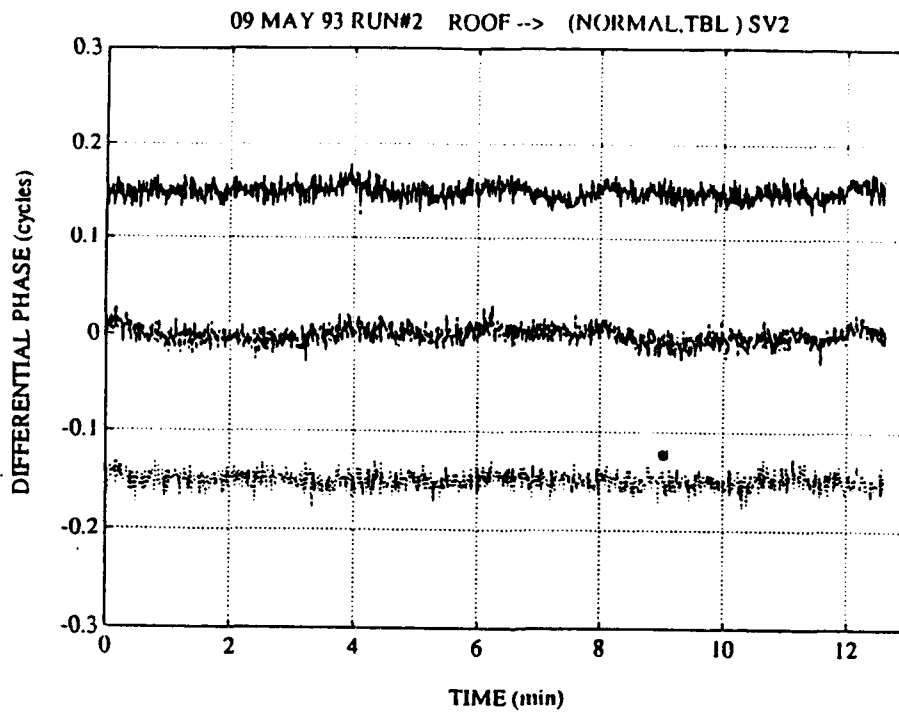


Fig. 5.11. Phase Difference Residuals for PRN 2, 9 May, 1993. *Solid line shows baseline 1 residuals offset by 0.15 cycles; dotted line shows baseline 2 residuals; dashed line shows baseline 3 residuals offset by -0.15 cycles.*

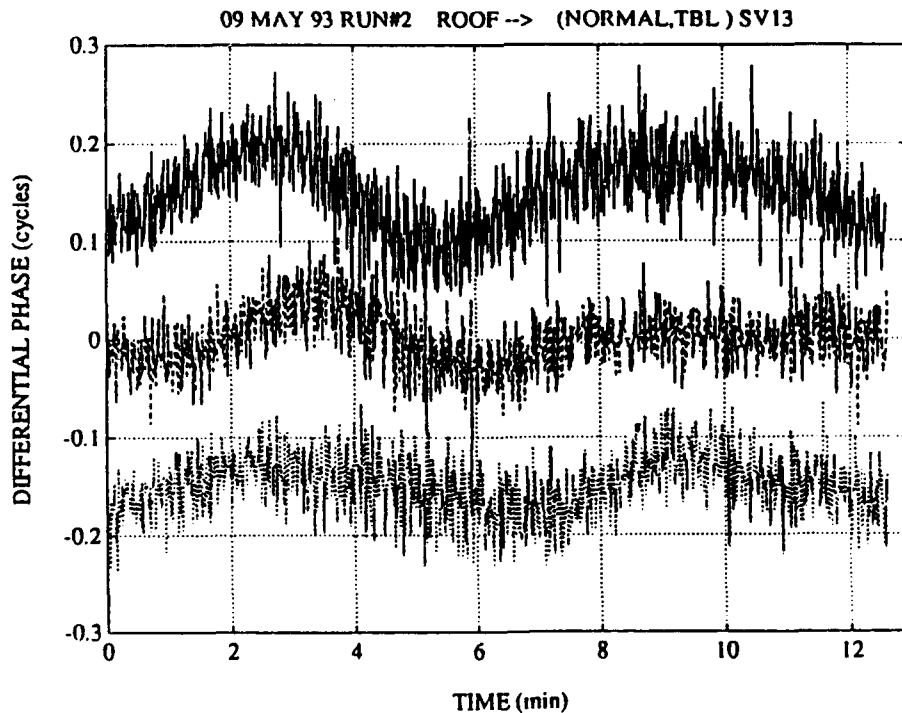


Fig. 5.12. Phase Difference Residuals for PRN 13, 9 May, 1993. *Solid line shows baseline 1 residuals offset by 0.15 cycles; dotted line shows baseline 2 residuals; dashed line shows baseline 3 residuals offset by -0.15 cycles.*

Systematic errors may be repeatable for certain aerospace applications. For example, a satellite in orbit may closely repeat its orientation with respect to the GPS constellation. Several tests were conducted to see if the repeatable multipath similar to those reported by Cohen and Parkinson [1991a] and Braasch [1992] could be observed in the raw phase data.

Tests for multipath repeatability were conducted on the roof of the Engineering Center using the x structure. Phase residuals were collected on several dates with 5 Feb 93 taken as a reference. Data from the following days were shifted by 4 minutes per day to compensate for the advance of the satellite ground tracks. Line of sight vectors to the satellites in view were compared to confirm that the same satellite alignment was achieved for the various data sets. Figure 5.13 shows phase residuals for SV 15 collected two weeks apart. Satellite motion has been removed from the residuals by a quadratic fit and the data for the three baselines was offset to display on the same graph. The satellite was fairly low on the horizon during these tests ( $\sim 25$  degrees), and it was setting behind the tower of the Engineering Center. Comparison of the results from 5 Feb and 19 Feb 93 shows a very strong repeatability of the multipath effect for all three antenna baselines.

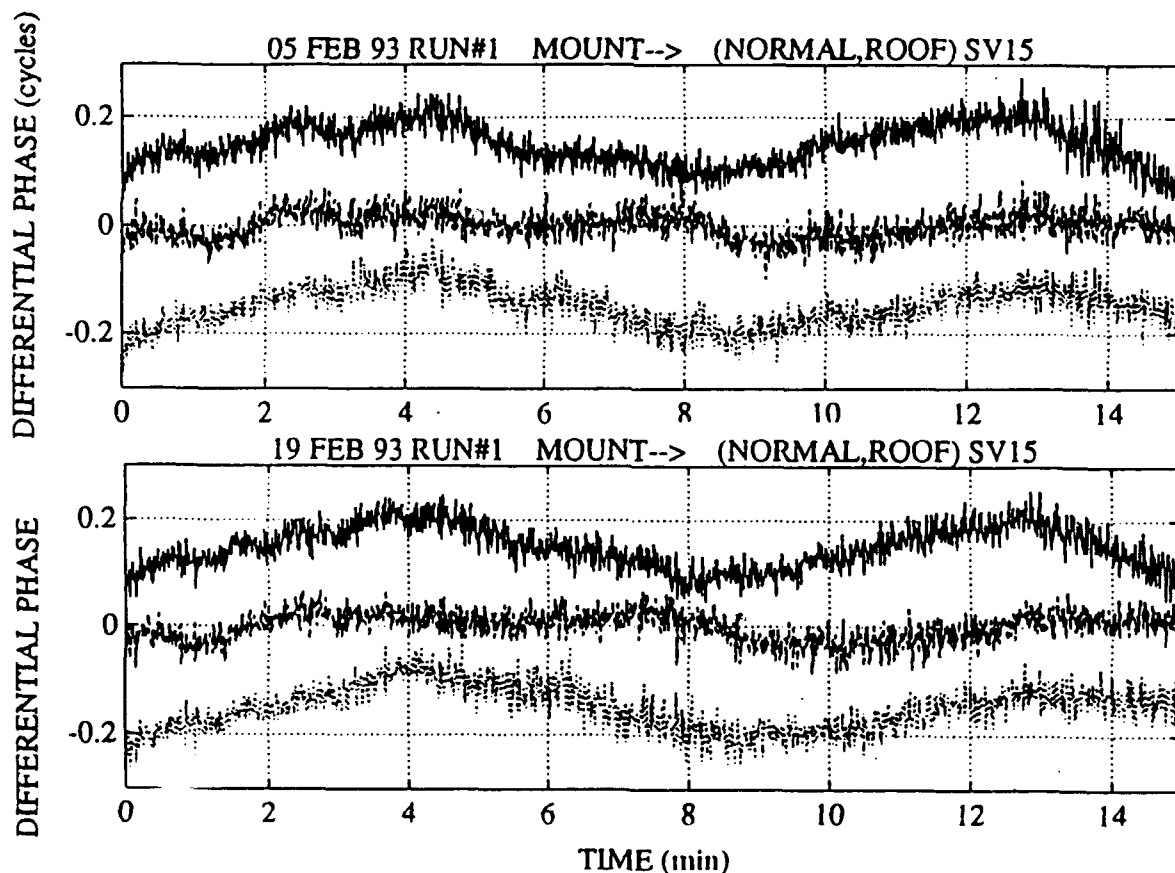


Fig. 5.13. Phase Difference Residuals for PRN 15. (a) is for 5 Feb 1993, (b) is for 19 Feb 1993. Solid line shows baseline 1 residuals offset by 0.15 cycles; dotted line shows baseline 2 residuals; dashed line shows baseline 3 residuals offset by -0.15 cycles.

Repeatability of multipath effects for these tests was also analyzed in the frequency domain by examining the power spectrum of each of the runs. The raw phase data from two different days were aligned to have the same satellite geometry, as before. A Fast Fourier Transform (FFT) was used to generate power spectra for the two cases. Figure 5.14 shows the power spectral densities for 30-minute runs on 5 and 19 Feb. Frequencies are normalized to the sampling rate of 2 Hz. Energies at specific frequencies are not evident from these plots and there is no obvious correlation between the two dates. This lack of clearly defined frequency content is probably due to Doppler broadening of the characteristic multipath frequencies due to satellite motion. Analysis of shorter time segments was then used to minimize the effect of satellite motion.

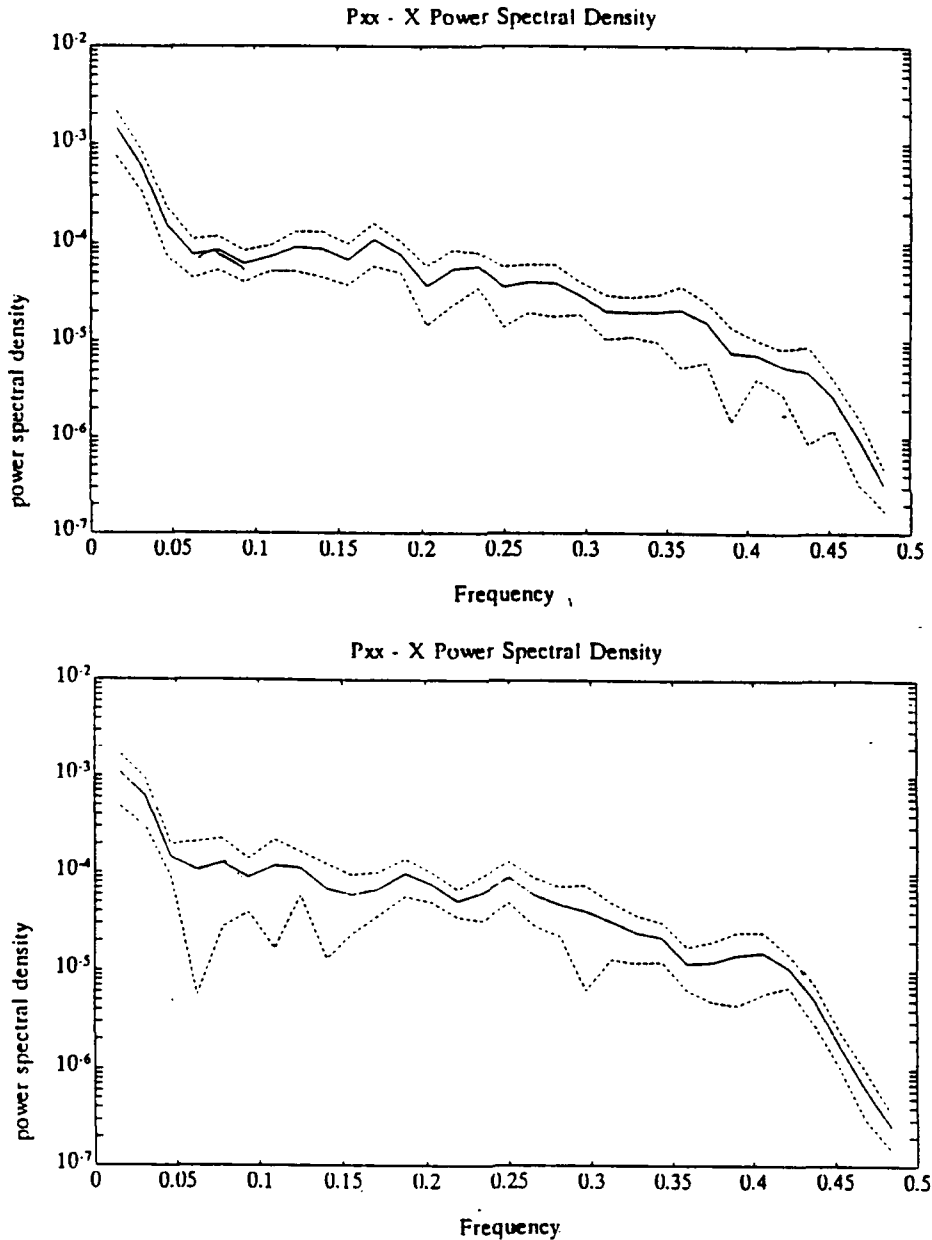


Fig. 5.14. Power Spectrum for 30-minute Run on 19 Feb 1993. (a) is for 5 Feb 1993, (b) is for 19 Feb 1993. Frequency is normalized to the sample rate of 2 Hz.

Figure 5.15 shows power spectra for a shorter (5 min.) portion of the same data set. Note that there are more "peaks" in the graphs, indicating energies at discrete frequencies. Also, the arrows show peaks that seem to be repeated for the two runs, possibly indicating a frequency contribution from a specific multipath reflector. This indicates some repeatable frequency components of the multipath effect which could be due to specific combination of multipath reflectors, however, the results are certainly not conclusive.

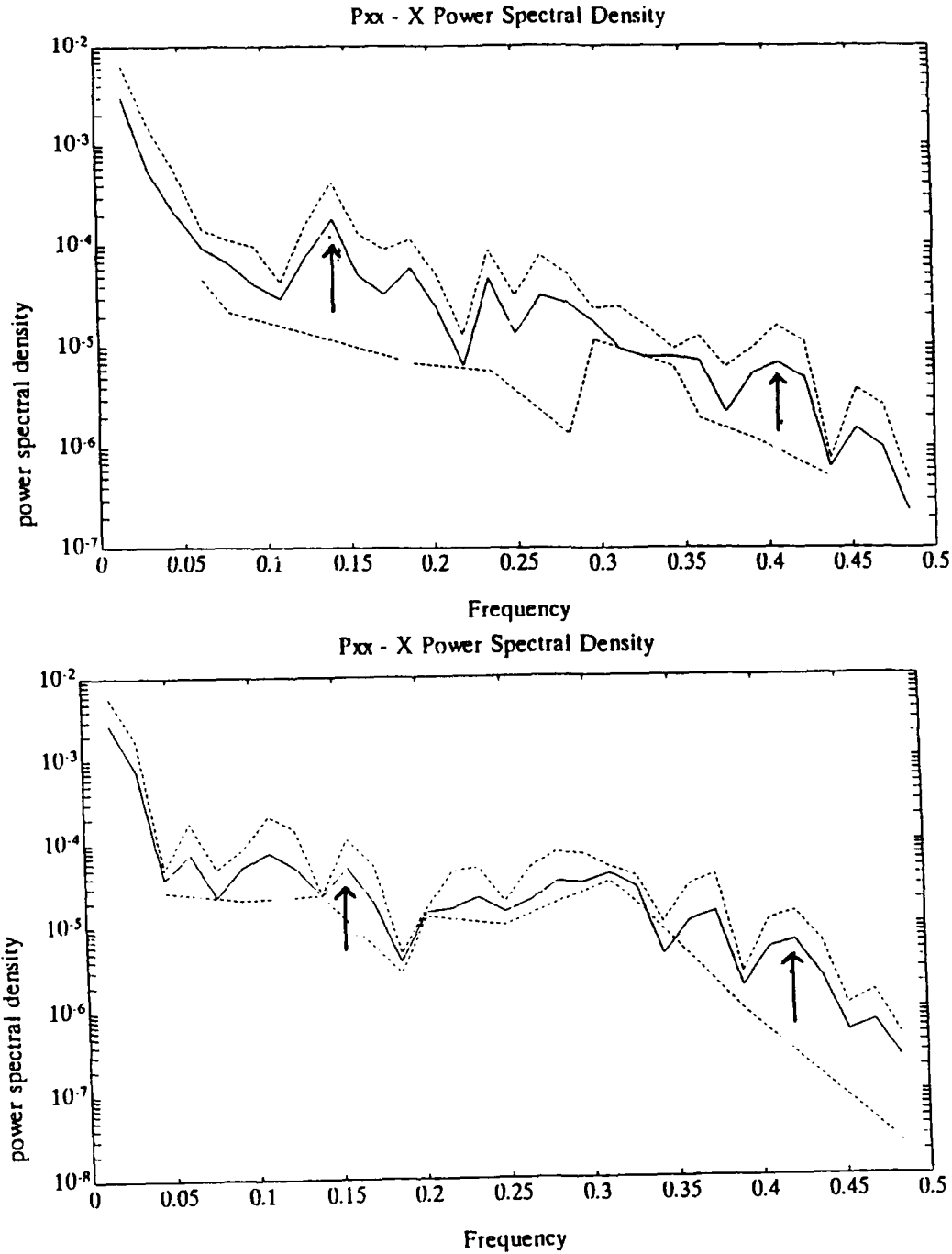


Fig. 5.15. Power Spectrum for 5-Minute Run on 5 Feb 1993. (a) is for 5 Feb 1993, (b) is for 19 Feb 1993. Frequency is normalized to the sample rate of 2 Hz.

### Multipath Modeling

Analytical modeling of multipath was used to try to identify the effects of single reflectors of the GPS signal based on geometric optics. Geometric optics consists of ray tracing for each reflector in the multipath environment.

Expressions for the composite carrier phase error due to a single multipath reflector and a fixed satellite geometry have been derived in Braasch [1992]. These expressions essentially account for a fixed frequency disturbance in the carrier phase that depends on the distance from the reflector to the receiver and the relative magnitudes of the direct and reflected signals. Figure 5.16 shows the power spectrum for simulated phase residuals from a single multipath reflector using the expressions found in Braasch [1992]. The elbow in the spectrum at a (normalized) frequency of about 0.08 is the energy due to the multipath reflector.

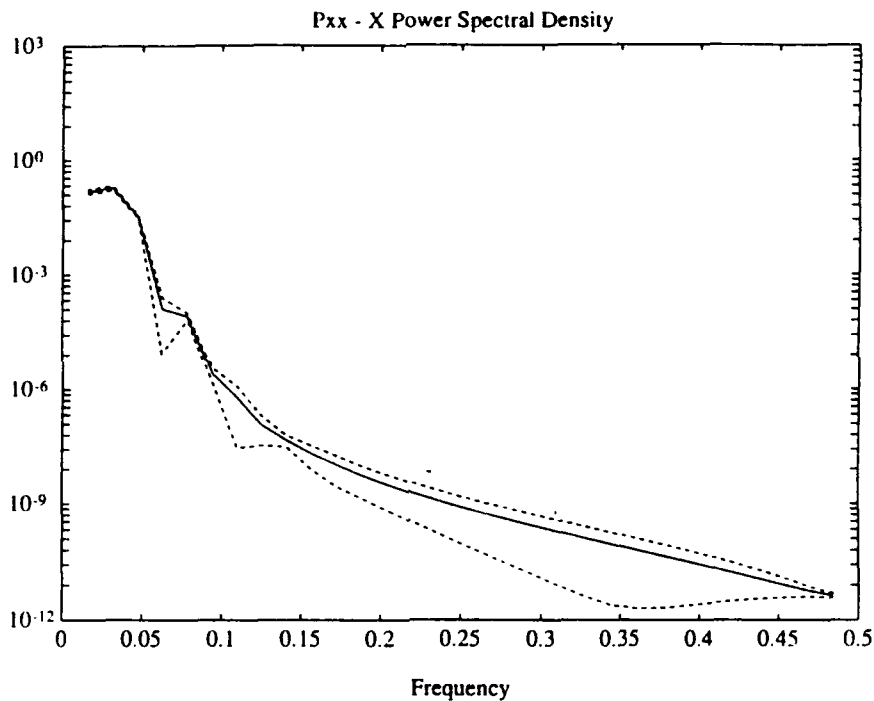


Fig. 5.16. Power Spectrum for Simulated Phase Residuals Using Static Model

The difficulty with this model is that it does not account for changes in the path difference due to satellite motion. An analytical model for a single multipath reflector was developed that does account for changing geometry due to satellite motion. The basic geometry is shown in Figure 5.17. The equations for path length difference between the direct and reflected signals for a reflector placed a distance  $d$  from the antenna can be shown to be:

$$\theta = \nu - \sin^{-1} \left[ \frac{r_e}{r} \sin \left( \frac{\pi}{2} - \nu \right) \right]$$

$$r = \sqrt{r_{sv}^2 + r_e^2 - 2r_{sv} r_e \cos \left( \frac{\pi}{2} - \nu \right)}$$

$$b = \sqrt{r^2 + d^2 - 2rd \cos \theta}$$

$$\Delta\lambda = b + d - r \tag{5.10}$$

where,  $\Delta\lambda$  is the path length difference,  $r$  is the path length for the direct signal,  $r_e$  is the radius of the earth,  $r_{sv}$  is the satellite orbit radius,  $\theta$  is the satellite look angle, and  $\nu$  is the satellite mean motion. All lengths are expressed in L1 carrier wavelengths.

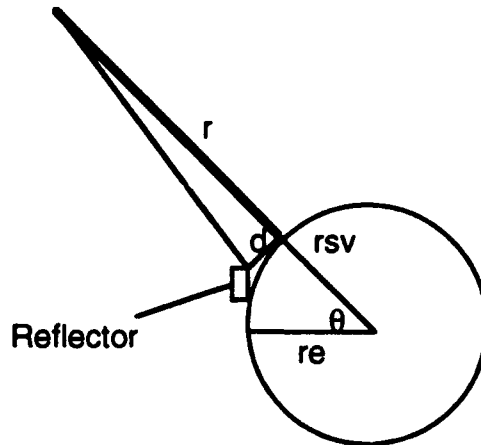


Figure 5.17 - Dynamic Multipath Model Geometry

The time difference between the arrival of the direct and reflected signal varies as the spacecraft travels overhead. The delay attains a minimum (zero) when the reflector is between the satellite and the receiver and all three are collinear, and reaches a maximum when all three are collinear with the satellite and receiver on opposite sides of the receive antenna.

Simulated multipath errors based on this model were compared with experimentally obtained phase residuals. These attempts to correlate ray tracing techniques with experimental results proved frustrating. Experimental results represent a composite of all multipath reflectors in the local environment, making it nearly impossible to isolate the effects of a single reflector (or even a few reflectors). Thus, although geometric optics is a useful tool for illustrating the basic mechanism of multipath, we were not able to use it to evaluate experimental results.

Another way of gaining insight into this effect that has been proposed by Cohen [1992, and Cohen and Parkinson, 1991a] is a spherical harmonic expansion of the multipath environment derived from empirical results. Although this appears to work well under some test conditions, it requires that multipath be exactly repeatable for a given satellite geometry. This may not be realistic if multipath reflectors change their reflective

characteristics under different temperature or moisture conditions or they change their configuration with respect to the antennas, as seen in the next experiment.

### Antenna Phase Center Migration

Another source of systematic error that must be considered is the migration of the electrical center of the antenna depending on the direction of the incoming signal. This effect could introduce a slowly varying error in the results that depends on the properties of the particular antennas used. The magnitudes reported for these errors range from about 0.8 cm [Lightsey, et al., 1993] to as much as 2 cm [Davis, et al., 1993]. A test designed to isolate antenna phase center motion for our antennas was conducted at Table Mountain using the wooden pallet antenna platform.

The basic approach for isolating antenna phase center motion was to design a field test where all conditions would repeat from day to day with the exception of antenna orientation. By comparing these results, all effects other than antenna phase center motion would cancel from the collected phase residuals. The tests were conducted with one baseline (Red-Blue) fixed as a control for all four runs of the experiment on 13-16 July 1993. The antenna for the other baseline (Red-Green) was rotated on successive days as shown in Figure 5.18.

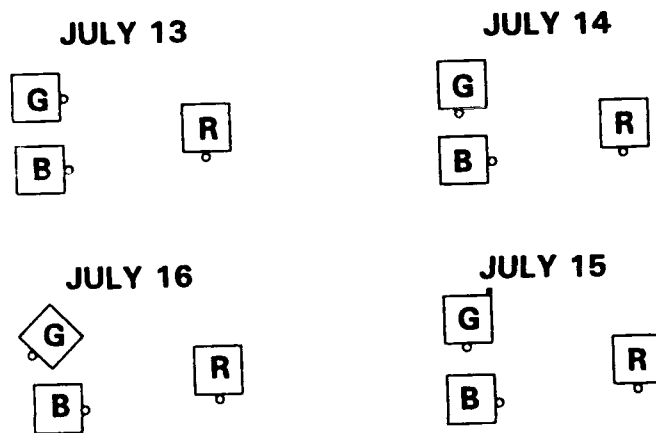


Fig. 5.18. Antenna Configurations for Phase Center Migration Tests. *Small circle indicates position of the cable connector. The red "R" antenna is the master; the blue "B" antenna is the control slave; the green "G" antenna is the slave antenna under test.*

The recorded phase residuals were shifted by four minutes per day to account for satellite motion. The data was then low-pass filtered to reduce the high frequency receiver noise. Satellite line of sight vectors stored every 30 seconds were interpolated to the one second measurement epochs. The phase residuals from July 16, 1993 were taken as the reference data set, and these were differenced with the phase residuals from the other days.

Unfortunately the results were not very conclusive because of the difficulty in achieving sub-centimeter repeatability of multipath effects in a less than ideal outdoor environment. For example, multipath reflectivity of the ground and other objects can change due to

differing moisture levels. Thus, it is possible that the results from July 13 and 14 were substantially different from July 15 and 16 because of rain showers on the earlier two days and dry weather during the latter.

Figure 5.19 shows the phase residuals for July 16 subtracted from July 15. The top graph (Figure 5.19(a)) shows the baseline with the rotated antenna configuration on the two days. Figure 5.19 (b) shows the results for the baselines with antennas fixed in the same position on both days. Note that the top graph for the rotated antenna baseline shows more systematic features and apparently larger deviations from zero. The standard deviation for the rotated antenna baseline is 3.7 mm while the standard deviation for the fixed baseline is 2.9 mm.

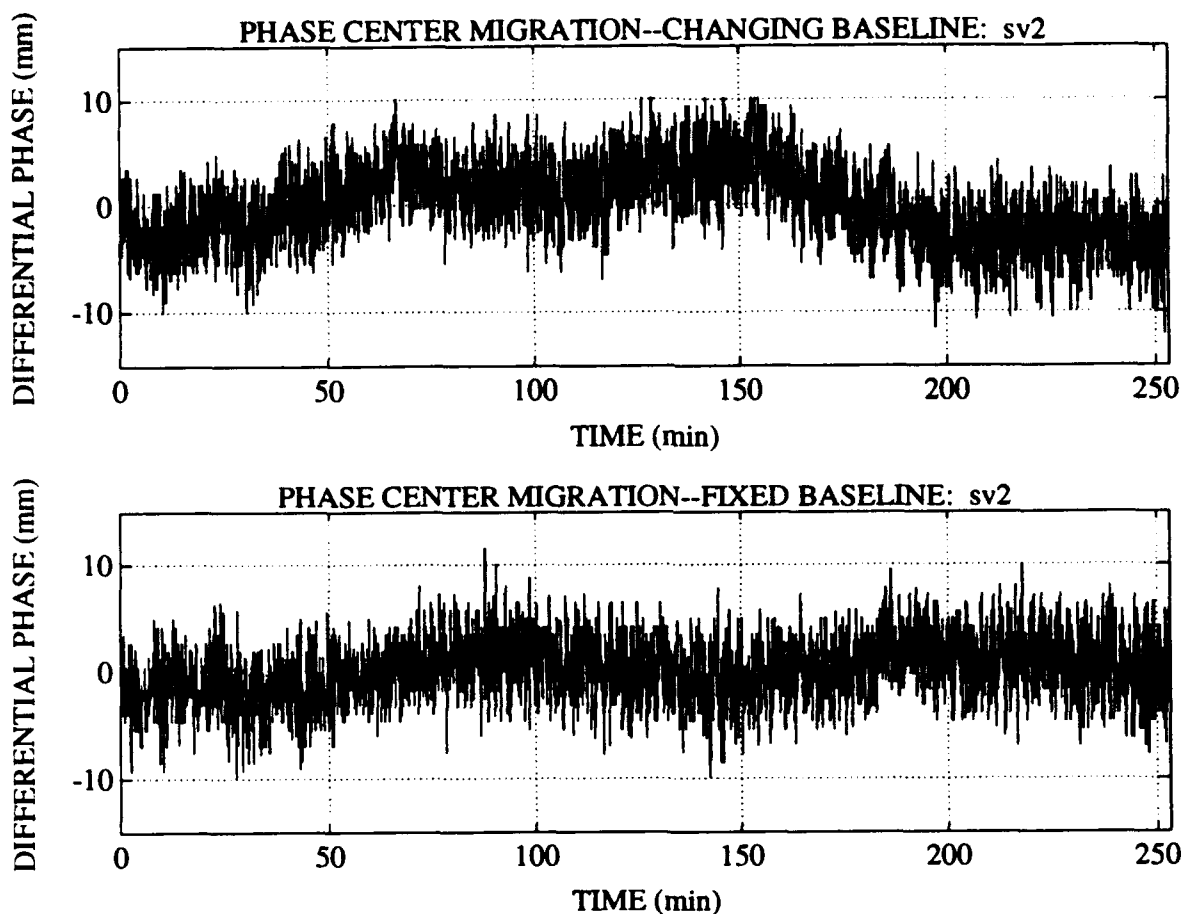
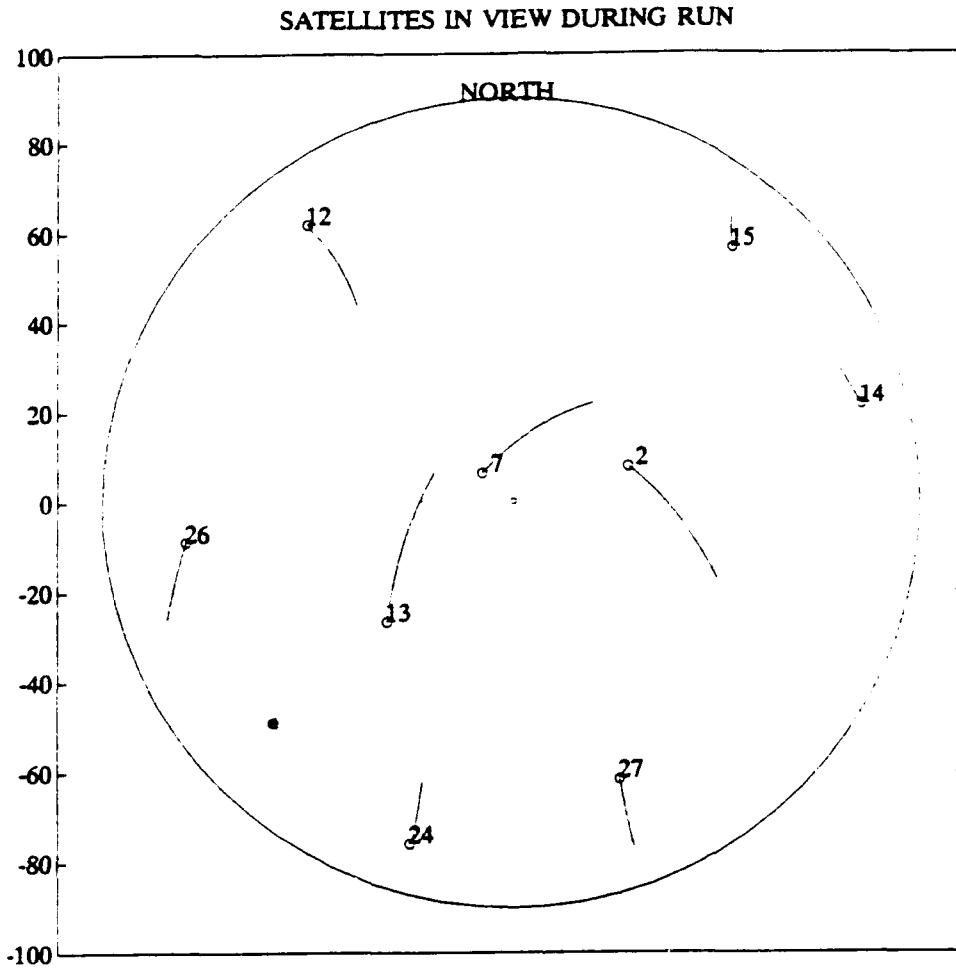


Fig. 5.19. Antenna Phase Center Migration Test Results for PRN 2 Comparing 15 Jul 1993 and 16 Jul 1993. (a) is for baseline with rotated antenna configuration, (b) is for baseline with fixed antenna configuration.

For all satellites in view during this test, the difference in standard deviation between the rotated and the fixed antenna baselines ranged from 0.1 mm to 1.6 mm. The satellites in view during the test are shown in Figure 5.20. Typically, the rotated antenna baseline standard deviation is about 0.6 - 0.7 mm larger than the fixed baseline. The smaller differences would indicate a small phase center migration for the particular satellite motion encountered, while the larger differences indicate larger migrations for that combination of antenna rotation and satellite motion.



5.20. Azimuth-Elevation Plot Satellites in View During Antenna Phase Center Motion Tests at Table Mountain. *Radial distance represents satellite zenith angle (90 deg - elevation).*

The important result from this test is that the rotated baseline exhibited larger standard deviations, and the graphs typically show more systematic effects than the fixed baseline. This strongly suggests that antenna phase center migration is being detected with this test. Note, however, that antenna phase center migration is not generally as large as multipath effects. These results also show that antenna phase center migration for our equipment is much smaller than the 20 mm for the test configuration used in Davis, et al. [1993]. Further tests could be used to calibrate antenna phase center migration for extremely accurate attitude solution processing, but this should not be a top priority until multipath errors have been reduced through some means to the same order of magnitude as the antenna phase center migration.

### 5.7 Baseline Survey Test

Static tests of the off-line survey were conducted to verify repeatability of baseline vector and line bias calculations. The goal of these tests was to identify the issues that will need to be resolved for real time implementation of the baseline survey.

### Equipment and Procedure

Testing was conducted using the wooden pallet structure on the roof of the engineering center. The pallets ensured that structural vibration and antenna motion could be eliminated during the baseline surveys. Two separate surveys of a single antenna baseline, were conducted on 27 Sep 93. They will be referred to as Survey 1 and Survey 2, and they each lasted more than 6 hours. The baseline and antenna orientation remained fixed throughout both surveys. The data was post processed using the algorithm discussed in Section 5.3 to provide an initial estimate of the baseline. Data outliers were then discarded by reprocessing the data using only points with differential range residuals less than 2 cm. The line bias for the baseline was then determined using the data set with outliers removed.

### Results

Table 5.2 shows the least squares baseline solutions for the two surveys. (Note that measurement outliers were removed.) The agreement in each component between the runs is 6 mm or better. The baseline lengths agree to better than 2 mm.

Table 5.2. Baseline Results for Survey 1 and Survey 2

	Survey 1	Survey 2
East Component	4.0189 m	4.0194 m
North Component	1.2837 m	1.2820 m
Up Component	-1.3748 m	-1.3800 m
Length	4.4373 m	4.4389

Table 5.3 shows the least squares solutions for the integer + line bias values for each satellite used in the solution. These results were also calculated with anomalous data points removed. The integers differ from survey to survey, as expected, since their value is run dependent. However, the line bias calibration should remain constant between surveys. Note from Table 5.3 that six satellites were used in Survey 1 while only four were used for Survey 2.

Table 5.3. Integer Plus Line Bias Results for Survey 1 and Survey 2. Integer plus bias values are given in units of L1 carrier wavelengths.

Survey 1	Survey 2
16.895	13.899
5.885	0.877
22.893	11.883
15.888	21.900
20.901	
-3.010	

The average line bias for survey 1 was 0.912 cycles, and the average for survey 2 was 0.890 cycles.

The surveys showed sub-centimeter repeatability in each of the baseline vector component directions, and the average line biases agree within about 0.02 cycles (less than 4 mm). This excellent repeatability provides confidence in the results; however the survey algorithm is not completely automated. To get reliable results we were required to manually identify outliers and eliminate satellites which were only tracked for a short arc. This does not present a problem for off-line, post-processed solutions, but treating such issues on-line will be more difficult.

Algorithms for real time implementation of the baseline survey must overcome these challenges. Anomalous data points must be discarded as they are collected, and cycle slips corrected as they occur. Since the duration of the runs is long (over 5 hours) many satellites enter and leave the field of view during the survey. Satellites which are only tracked for a short arc cannot be used to determine the line bias. For example, consider the last row in Table 5.3 for survey 1. This integer plus line bias value corresponds to a satellite that was rising less than 2 hours before the survey was terminated, resulting in fewer data points being available to generate this value. If this value is discarded from the average, then the average line bias for survey 1 is 0.892 cycles, a difference of only 0.002 cycles from survey 2.

On the other hand, discarding too many data points or eliminating satellites from the algorithm can quickly lead to underdetermined solutions for the baselines and integer plus bias values. Automating these trade-offs in a robust real-time algorithm will be a major challenge in future research.

### **5.8 Relative Pitch Accuracy Test**

The next experiment performed was designed to compare the change in pitch reported by the receiver to an independent measure of the angular change determined by the motion of the laser.

#### **Equipment and Procedure**

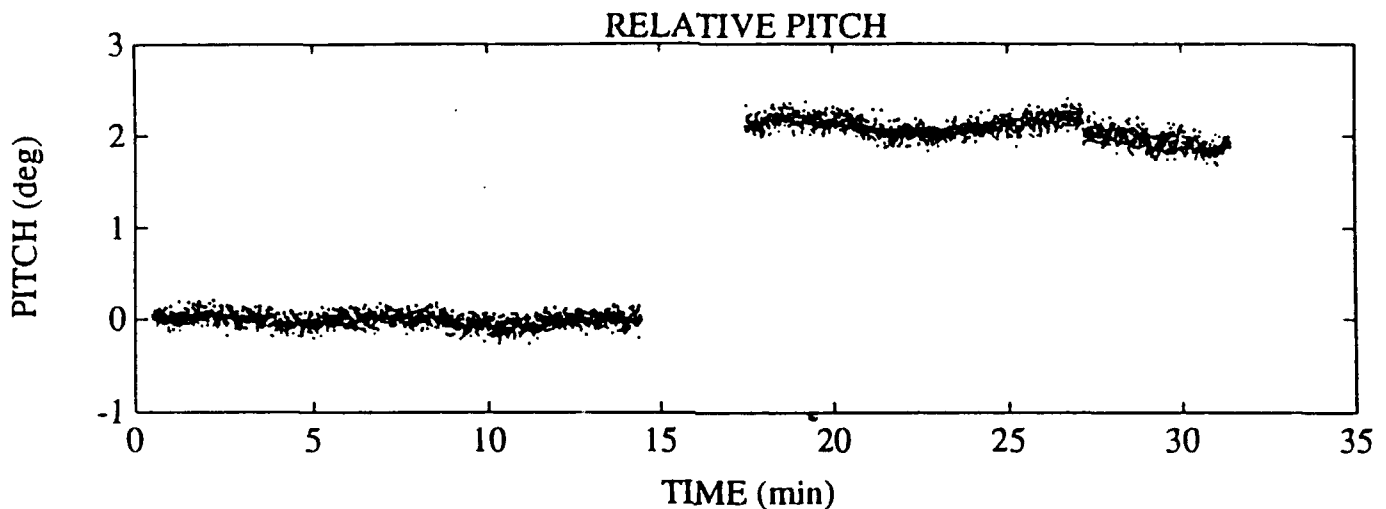
The test structure is fitted with the laser mounted below the baseline 2 slave antenna. The laser is initially pointed at the wall of a small storage shed approximately 50 meters away. The laser image on the wall (approximately 4 cm in diameter) is marked and the GPS based attitude solutions are collected for about 15 minutes. The structure is then pitched upward until the laser is aligned with a point higher on the wall. The higher spot is marked, and data is again collected for about 15 minutes. Finally, the structure is removed from the control point and replaced with a Wild T2 Theodolite to perform an independent measure of the angular distance between the center of the marks. The estimated precision of the laser image marks is about 1 cm, producing an angular error of 0.012 degrees on a 50 meter baseline. The precision of the theodolite measurement is better than 0.001 degrees. Thus, the pitch reference angle is good to about 0.012 degrees.

### Results

Figure 5.21 shows the GPS based relative pitch angle estimates. The pitch values are offset so that the mean for the first 15 minutes is zero degrees.

The measured relative change in pitch during the test was 2.07 deg. Using a Wild T2 Theodolite the angular separation of the marks was measured at 1.96 degrees, indicating a relative accuracy of approximately 0.11 deg for this test. The T2 Theodolite optical measurement is accurate to better than 0.001 deg.

This result is consistent with our expectations based on the measurement quality and the baseline length.



5.21. Real Time Relative Pitch Estimates, 10 May 1993

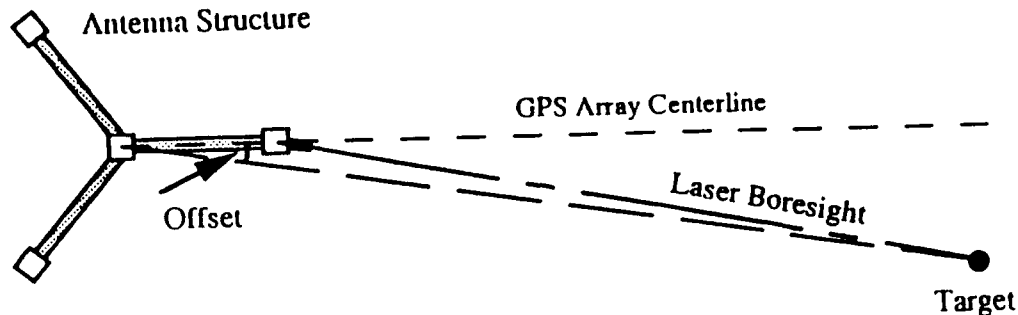
### 5.9 Absolute Heading Accuracy Test

The primary goal of the performance tests was to determine the accuracy of the real time attitude solutions as compared to the known pointing direction. Because of the configuration of our test range and structure, it was most straightforward to determine the absolute accuracy of the GPS heading indication.

#### Equipment and Procedure

To evaluate absolute heading accuracy, the tree structure is set up in a known orientation as follows. The structure is centered on the base point. A survey pole mounted in a tripod is centered on one of the control points using a plumb line. The structure is then rotated until the laser image appears on the survey pole. GPS attitude solution data is collected for approximately 15 minutes. The procedure is repeated for other control points. Errors in positioning the structure, the survey poles, and aligning the laser, are estimated to contribute no more than 3 cm of systematic error. The survey error contributions are negligible in comparison. Thus, over the survey baselines of 30-70 m the total error in the "known" orientation of the structure is less than 0.06 degrees.

Since the laser is not precisely aligned with the electrical centerline of the GPS antenna array, a calibration must be performed each time it is mounted. The actual misalignment involves both an offset and a rotation of the laser boresite from the structure centerline, as shown in Figure 5.22. However, because the laser image is viewed from at least 30 meters away, only the rotational misalignment is important.



5.22. Laser Misalignment from Antenna Centerline

### Results

The absolute accuracy of the receiver was tested by aligning the structure with survey poles at the control points using a laser as described in Section 5.5. These tests were performed on May 10, 12, 18, and 20, 1993. Data was collected with the structure pointed at various sites.

The laser misalignment was determined by computing the difference between the known heading and the mean measured heading, and a correction based on this misalignment was applied to correct the measured heading. Details of the laser misalignment calibration are found in [Axelrad and Chesley, 1993]. Excluding Point A, for which the absolute heading was not reliable, the best agreement was  $\pm 0.07$  degrees. The poorest agreement for the tests was  $\pm 0.20$  degrees. Changes in satellite geometry, signal strength, multipath effects, and integer bumps account for the differences between sessions. Integer bumps will be discussed in the next subsection.

Typical heading results from the pointing tests are shown in Figure 5.23 when the structure was aligned with points B and C. The mean measured heading differs from the true heading by  $-0.16$  degrees for Point B and by  $+0.20$  degrees for Point C. Figure 5.24 summarizes the heading errors for all the absolute pointing tests.

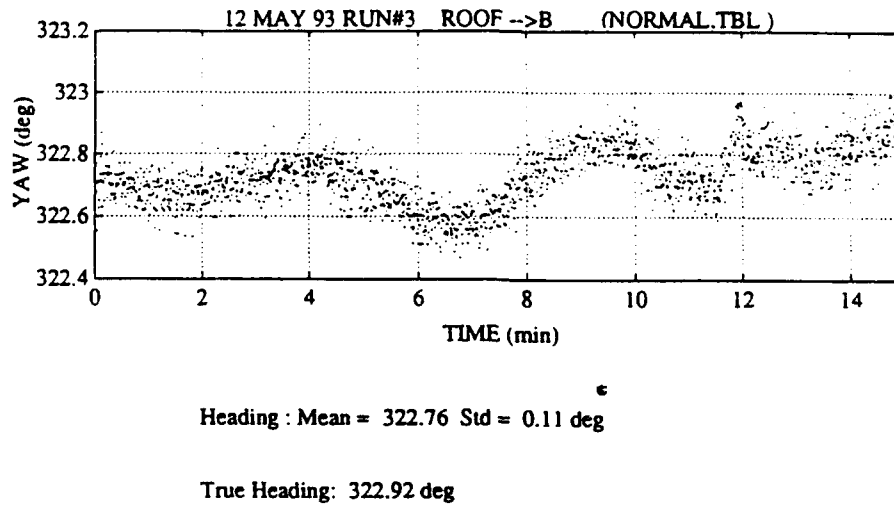


Fig. 5.23. Adjusted Heading Results for Tree Structure, 12 May 1993

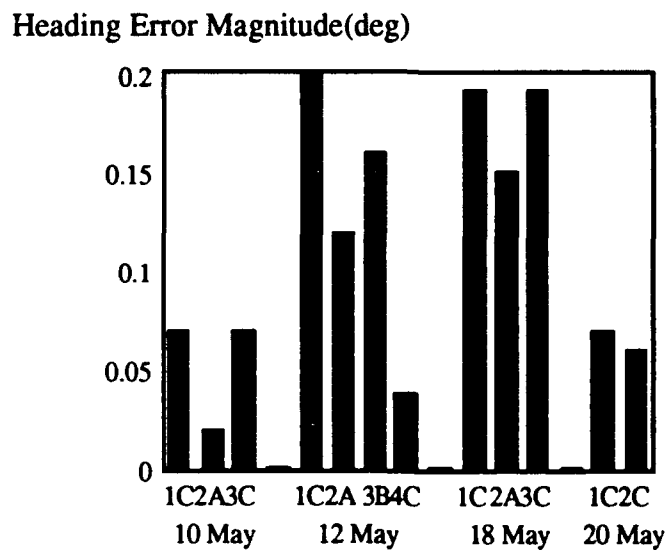


Fig. 5.24. Summary of Adjusted Heading Errors for Absolute Tests.

We compared the real time heading reported by the receiver to the known value for a nearly orthogonal antenna array with baselines of 1.4 m. The mean error for each test was 0.2 deg or less. The standard deviation was approximately 0.1 deg.

The accuracy of the receiver is limited primarily by systematic errors, which are probably due to multipath and antenna phase center motion as described above. For these tests, the reference was provided by a diode laser mounted to the structure. This laser can be thought of as representative of a spacecraft instrument which is to be pointed at a target. The offset or misalignment of the GPS antenna array centerline to the boresite of interest must be calibrated. In our tests, a new calibration was required for each day. However, this is very impractical. For spacecraft applications and for our future ground tests, we plan to perform this calibration in conjunction with the structure baseline self survey.

### **5.10 Degraded Test Structure**

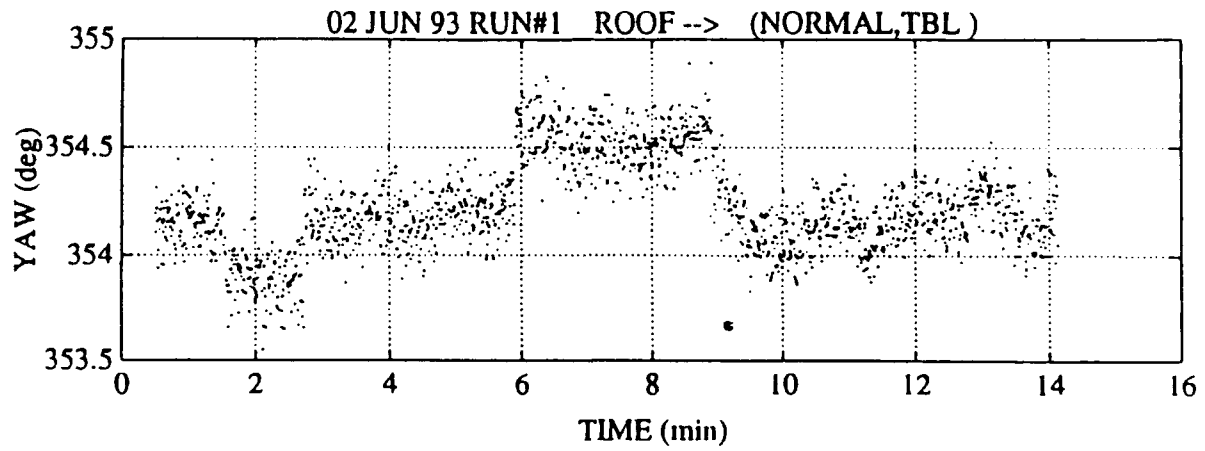
An alternate antenna configuration was used to compare pointing accuracy results for different antenna baseline configurations. If the baselines are orthogonal, then attitude accuracy is enhanced. If the baselines are coincident, then attitude determination is degraded. The objective of this test was to gain a qualitative sense for how much degradation could be expected for the tree structure.

#### **Equipment and Procedure**

The arms of the tree structure were modified so that all the slave antennas were roughly in the same direction relative to the master and all four antennas are more coplanar. This was done to *decrease* the sensitivity of the antenna geometry to changes in heading. So rather than being orthogonal, the maximum angular separation of antenna baselines was 15 degrees. Attitude data were then collected in using the same procedure used for the absolute accuracy tests.

#### **Results**

Test results using the structure with poor geometry confirm that antenna placement is an important limiting factor in attitude solution accuracy. Not only should the baselines be as long as practically possible, but they should also be configured as nearly orthogonal as possible. Sample test results for the geometrically degraded structure are shown in Figure 5.25.

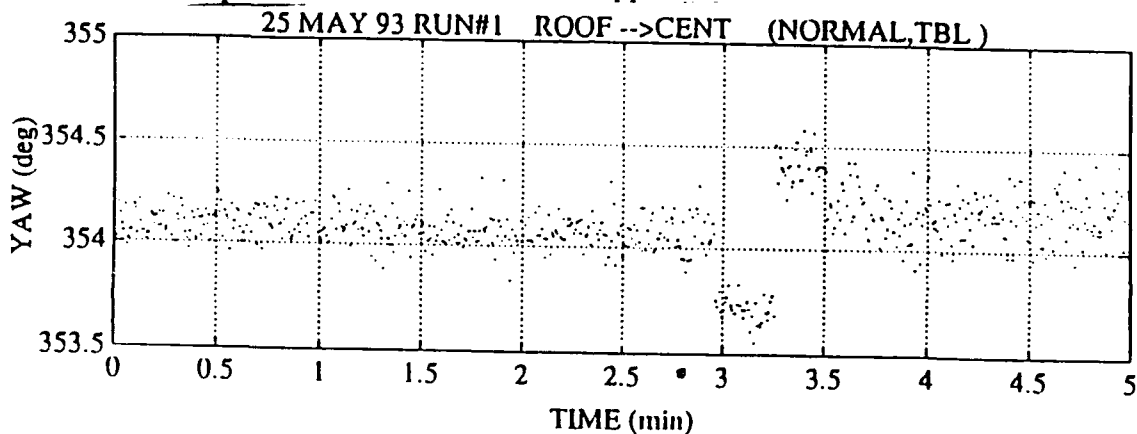


Heading : Mean = 354.2270 Std = 0.21 deg

5.25. Adjusted Heading Results for Degraded Test Structure, 2 Jun 1993

The standard deviation in heading for the degraded structure is approximately double that for the optimal structure, and the heading solution suffers many jumps due to integer bumps in the solution algorithm. This indicates that the integer number of wavelengths between the antennas was not well resolved due to the poor structure geometry, and limits the usefulness of this structure geometry for determining accurate attitude results.

The key to accurate GPS based attitude determination is correctly determining the integer ambiguities. The receiver Trimble automatically monitors the validity of these integers and corrects them if that becomes necessary. A faulty integer bump would temporarily degrade the attitude solution until the monitoring algorithm detected it and returned it to the correct value. An example of this can be seen in Figure 5:26. Note the downward jump in the yaw value at about 3 minutes into the run corresponding to an integer bump. The integer is bumped back again after about 15 seconds, and the heading returns toward the correct value. The entire episode lasts about 30 seconds, and the largest excursion is approximately 0.5 degrees. These effects tend to average out for long static runs, but they could introduce problems in critical real time applications.



Heading : Mean = 354.1084 Std = 0.15 deg

ACTUAL HEADING: 354.1864 deg

Fig. 5.26 Adjusted Heading Results for Tree Structure Showing Incorrect Integer Bump

### 5.11 Dynamic Tests

Initial tests have been conducted on the roof of the Engineering Center using the one-armed spinner. The objective of these tests was to gain preliminary experience using the receiver in a dynamic environment. The single baseline of the one-armed spinner was surveyed, and differential phase data has been collected while the platform was rotating. At the time of this writing, no attitude solutions have been generated using the spinning platform.

## **6. Future Work**

In this first year project, good progress was made in establishing the tools and expertise for research in GPS based spacecraft attitude determination. In the process, we have identified several key areas which we plan to pursue. The objective of this continuing research is to develop new algorithms which are more accurate, reliable, and robust for real time, on-orbit operation.

The first task ahead is to validate the existing algorithms using data collected on-orbit. We have just received a set of raw data files collected from the RADCAL satellite. Some preliminary results based on this data were presented by C. Cohen and G. Lightsey [1993] at the recent ION conference in Salt Lake City. There are several challenges to working with the RADCAL data. Unfortunately, a reliable static survey of the baselines was not performed prior to launch; thus, the baselines and line biases must be determined from the on-orbit data. Second, the multipath environment on the spacecraft is expected to be poor because of the many structures located near the GPS antennas. To try to reduce this effect, the antennas were canted away from the vehicle centerline. However, this means that there may not be as many satellites visible to all antennas, as in the ideal case where the antennas are oriented opposite nadir. Finally, the geometry is also not ideal in that the three antenna baselines are coplanar. Of course, these are all realistic considerations in implementation of GPS for onboard attitude determination; thus they provide a good test for our algorithms.

Our planned approach to processing the RADCAL data is as follows:

- Process the pseudorange data through the navigation filter to solve for the vehicle orbit.
- Store the computed satellite-to-GPS line of sight vectors to a file.
- Batch process the phase data for the entire 5 hour pass to solve for the baseline coordinates, line biases, and integer ambiguities.
- Repair observed cycle slips in the data.
- Fix the baselines and line biases and pass the phase data through the attitude filters to solve for the vehicle orientation.

Unfortunately, to our knowledge, there is no external attitude reference with which to compare our results. However, as a check, we do plan to compare both intermediate and final results with those being generated by Lightsey at Stanford University.

Once we are able to achieve reliable results with this multi-stage process we will begin investigating enhancements to the filter to permit real time estimation of the baseline configuration and line biases. Improvements in our current method are needed to perform the integer ambiguity resolution and both detection and correction of cycle slips. The new method can be evaluated with both the RADCAL data and simulated data. We will also continue to explore other opportunities for obtaining data collected on-orbit to further validate this work.

The computer simulation needs to be upgraded to account for alternate vehicle dynamics such as an inertially pointing spacecraft, and more realistic baseline configurations and visibilities. We are also interested in investigating the effects of vehicle flexure on the performance of the existing algorithms and enhancing them to permit some changes in the structure or antenna configuration.

In the ground test area we are continuing to work with the data collected on the one armed spinner. We hope to extract some useful information from these tests and to use the experience gained in this experiment to guide the upgrade of the test bed. We are planning to improve the dynamic test platform and to conduct more systematic tests in a similar configuration. In particular, the new structure will be considerably stiffer than those used thus far, and an external "truth" reference will be provided by a platform encoder.

One feature that was evident in both the simulation studies and ground tests is the detrimental effect of multipath on the attitude solutions. We propose to conduct an experiment using narrow beam antennas (similar to those used on the codeless attitude determination system designed by MacDoran and Snyder) with the Vector receiver. The performance of the receiver with the narrow beam versus standard patch antennas can be compared in a ground test on Engineering Center roof. Another possibility is to try to accurately simulate the performance of such an antenna on orbit to evaluate the potential benefits for spacecraft applications.

During the next year we hope to continue to learn more about GPS performance both on the ground and in orbit, and to develop reliable attitude determination algorithms which could be tested in real-time onboard a near Earth spacecraft. If we are successful, the next step will be perform closed-loop onboard attitude control based on GPS feedback.

## References

- Axelrad, P. and B.W. Parkinson, "Closed Loop Navigation and Guidance for Gravity Prove B Orbit Insertion," *Navigation*, Vol. 36, Spring 1989.
- Axelrad, P. and B.C. Chesley. "Performance Testing of a GPS Based Attitude Determination System," AIAA-93-3787, AIAA GN&C, Monterey, California, August 9-11, 1993.
- Braasch, M.S. "On the Characterization of Multipath Errors in Satellite-Based Precision Approach and Landing Systems," Ph.D. Dissertation, Ohio University, June 1992.
- Bertiger, W., Y. Bar Server, B. Haines, R. Ibanez-Meier, P. Abusali, R. Mullerschoen, T. Munson, H.J. Rim, B. Schutz, P. Willis, S. Wu, and T. Yunck, "The First Low Earth Orbiter with Precise GPS Positioning: Topex/Poseidon," Preprint of paper to be published in the Proceedings of ION GPS-93, Salt Lake City, UT, Sept. 22-24, 1993.
- Brown, R.A. "Instantaneous GPS Attitude Determination," Proceedings of the IEEE PLANS, Las Vegas, NV, 1992.
- Brown, R.A. and A.G. Evans, "GPS Pointing System Performance," Proceedings of ION GPS-90, Colorado Springs, CO, September 1990.
- Brown, R.A. and P. Ward. "A GPS Receiver with Built-in Precision Pointing Capability," Proceedings of the IEEE Plans, Las Vegas, NV, 1990.
- Cohen, C.E. and B.W. Parkinson, "Mitigating Multipath in GPS-Based Attitude Determination," AAS Guidance and Control Conference, Keystone, CO, Vol. 74, Univelt, San Diego, 1991a.
- Cohen, C.E. and B.W. Parkinson. "Expanding the Performance Envelope of GPS-Based Attitude Determination," Proceedings of ION GPS-91, Albuquerque, NM, September 11-13, 1991b.
- Cohen, C.E. and B.W. Parkinson, "Integer Ambiguity Resolution of the GPS Carrier for Spacecraft Attitude Determination," AAS 92-015, AAS Guidance and Control Conference, Keystone Colorado, February 8-12, 1992a.
- Cohen, C.E. and B.W. Parkinson. "Aircraft Applications of a GPS-Based Attitude Determination," Proceedings of ION GPS 92, Albuquerque, New Mexico, Sept. 16-18, 1992b.
- Cohen, C.E., H.S. Cobb, and B.W. Parkinson. "Generalizing Wahba's Problem for High Output Rates and Evaluation of Static Accuracy Using a Theodolite," Proceedings of ION GPS 92, Albuquerque, New Mexico, Sept. 16-18, 1992.
- Cohen, C.E. *Attitude Determination Using GPS*, Ph.D. Dissertation, Department of Aeronautics and Astronautics, Stanford University, December 1992.
- Cohen, C.E. and G.E. Lightsey, Presentation on RADCAL GPS Results - (Paper not yet available.), at ION GPS-93, Salt Lake City, UT, Sept. 22-24, 1993.

- Comp, C.S., C. Brown, D. Kubitschek, and L. Reeder, "Optimal Antenna Configuration for GPS Based Attitude Determination," Final Report, ASEN 4028, University of Colorado, May 1992.
- Davis, E.S., et al, "TOPEX/POSEIDEN GPS-Based Precision Orbit Determination Experiment Final Review," Jet Propulsion Laboratory Document D-10764, May 1993.
- Diefes, D. "GPS Based Attitude Determining System for Marine Navigation," Presentation at ION GPS-93, Salt Lake City, UT, Sept. 22-24, 1993.
- Ferguson, K., et al., "Three-Dimensional Attitude Determination with the Ashtech 3DF 24-Channel GPS Measurement System," Proceedings of the ION National Technical Meeting, Phoenix, AZ, Jan. 1991.
- Gelb, A., *Applied Optimal Estimation*, MIT Press, 1984.
- Gold, K., W. Bertiger, S. Wu, T. Yunck, R. Muellerschoen, and G. Born, "GPS Orbit Determination for the Extreme Ultraviolet Explorer," preprint of paper to be published in the Proceedings of ION GPS-93, Salt Lake City, UT, Sept. 22-24, 1993.
- Green, G.B., P.D. Massatt, and N.W. Rhodus, "The GPS 21 Primary Satellite Constellation," *Navigation*, Vol. 36, Spring 1989.
- Jurgens, R.D. and C. Rodgers. "Advances in GPS Attitude Determining Technology as Developed for the Strategic Defense Command", Proceedings of ION GPS-91, Colorado Springs, CO, Sept., 1991.
- Larson, W.J. and J.R. Wertz, Ed., *Space Mission Analysis and Design*, Second Edition, Kluwer Academic Publishers, 1992.
- Lear, W. M. Montez, L. Rater, and L. Zyla, "The Effect of Selective Availability on Orbit Space Vehicles Equipped with SPS GPS Receivers", Proceedings of ION GPS-92 , Albuquerque, New Mexico, Sept. 16-18, 1992.
- Lefferts, E.J., F.L. Markley, and M.D. Shuster, "Kalman Filtering for Spacecraft Attitude Estimation", *Journal of Guidance, Control, and Dynamics*, AIAA Paper 82-0070, AIAA 20th Aerospace Sciences Meeting, Orlando, FL, January 1982.
- Levenson, M., et al, "ACS Spacetask," Naval Research Laboratory Report, 1992.
- Lightsey, E.G., C.E. Cohen, and B.W. Parkinson. "Application of GPS Attitude Determination to Gravity Gradient Stabilized Spacecraft," AIAA-93-3788, AIAA GN&C, Monterey, California, August 9-11, 1993.
- Lu, G., M.E. Cannon, G. Lachapelle, and P. Kielland. "Attitude Determination in a Survey Launch Using Multi-Antenna GPS Technologies," ION National Technical Meeting, San Francisco, California, 20-22 January 1993.
- Madden, C., S. Lee, and H. Tran, "Near Term GPS Application for Shuttle," Proceedings of ION GPS 92, Albuquerque, New Mexico, Sept. 16-18, 1992.

- Markley, F.L., "Attitude Determination using Vector Observations and the Singular Value Decomposition", *Journal of the Astronautical Sciences*, Vol. 36, No. 3, 1988, pp. 245-258.
- Martin-Niera, M. and R. Lucas, "GPS Attitude Determination of Spin Stabilized Satellites," Proceedings of ION GPS 92, Albuquerque, New Mexico, Sept. 16-18, 1992.
- Melvin, P. J., "A Kalman Filter for a Gravity Gradient Satellite", Paper No. AAS 91-483, 1991 AAS/AIAA Astrodynamics Conference August 19-22, 1991.
- Milliken, R.J. and C.J. Zoller. "Principle of Operation of NAVSTAR and System Characteristics," ION Redbook on the Global Positioning System, Vol. I, 1980.
- Munjjal, P., W. Feess, and M. Ananda, "A Review of Spaceborne Applications of GPS," Proceedings of ION GPS 92, Albuquerque, New Mexico, Sept. 16-18, 1992.
- Rath, J. and P. Ward, "Attitude Estimation Using GPS," ION National Technical Meeting, San Mateo, California, January 1989.
- Roberts, D. "Radial Base Line Comparisons between Conventional Surveying Techniques and Global Positioning System's Quick Static Method," UNAVCO internal report, August 1990.
- Saunders, Penny, Personal communication September 22, 1993.
- Shuster, M.D., Preliminary Notes for "Spacecraft Attitude Determination and Control, Chapter 5.", 1989.
- Trimble Navigation, "TANS Vector Specification and User's Manual," July 1992.
- UNAVCO, GPS Test Network Survey Results, UNAVCO internal memo, 1 April 1993.
- Van Graas, F. and Braasch, M. "GPS Interferometric Attitude and Heading Determination: Initial Flight Test Results," *Navigation*, Vol. 38, No. 4, Winter 1991-92, pp. 297-317.

## Appendices

### A. Calculating a Transformation Matrix from Quaternions and Euler angles

The transformation matrix,  $C$ , can be expressed in terms of Euler angles. Let  $\theta_1$  be the rotation about the 1-axis,  $\theta_2$  be the rotation about the 2-axis, and  $\theta_3$  be the rotation about the 3-axis. Perform these rotations in 3-2-1 order where  $\theta_3$  is the first rotation,  $\theta_2$  is the second rotation, and  $\theta_1$  is third rotation. This gives

$$C_{321}(\theta_1, \theta_2, \theta_3) = \begin{bmatrix} \cos\theta_2\cos\theta_3 & \cos\theta_2\sin\theta_3 & -\sin\theta_2 \\ \sin\theta_1\sin\theta_2\cos\theta_3 - \cos\theta_1\sin\theta_3 & \sin\theta_1\sin\theta_2\sin\theta_3 - \cos\theta_1\cos\theta_3 & \sin\theta_1\cos\theta_2 \\ \cos\theta_1\sin\theta_2\cos\theta_3 + \sin\theta_1\sin\theta_3 & \cos\theta_1\sin\theta_2\sin\theta_3 - \sin\theta_1\cos\theta_3 & \cos\theta_1\cos\theta_2 \end{bmatrix} \quad (\text{A-1})$$

The transformation matrix,  $C$ , can also be expressed in terms of quaternions as follows,

$$C(\mathbf{q}) = (q_4^2 - |\bar{\mathbf{q}}|^2)\mathbf{I} + 2\bar{\mathbf{q}}\bar{\mathbf{q}}^T + 2q_4\bar{\mathbf{q}}^x$$

$$\text{or, } C(\mathbf{q}) = \begin{bmatrix} q_1^2 - q_2^2 - q_3^2 + q_4^2 & 2(q_1q_2 + q_4q_3) & 2(q_1q_3 - q_4q_2) \\ 2(q_2q_1 - q_4q_3) & -q_1^2 + q_2^2 - q_3^2 + q_4^2 & 2(q_2q_3 + q_4q_1) \\ 2(q_3q_1 + q_4q_2) & 2(q_3q_2 - q_4q_1) & -q_1^2 - q_2^2 + q_3^2 + q_4^2 \end{bmatrix} \quad (\text{A-2})$$

$$\text{where } \bar{\mathbf{q}} = \begin{bmatrix} q_1 \\ q_2 \\ q_3 \end{bmatrix} \text{ and } \mathbf{q} = \begin{bmatrix} \bar{q} \\ q_4 \end{bmatrix}.$$

## B. Dynamics Matrices

The non-zero elements of the dynamics matrix derived from the linearized angle equations of motion (4.20) and used in the Euler angle filter equation (4.54) are

$$\begin{aligned}
 F_{14} &= F_{25} = F_{36} = 1 \\
 F_{41} &= [-nh_w - (I_3 - I_2)n^2] / I_1 \\
 F_{45} &= [-h_w + (I_1 + I_2 - I_3)n] / I_1 \\
 F_{52} &= [-nh_w - 4(I_3 - I_1)n^2] / I_2 \\
 F_{54} &= [h_w - (I_1 + I_2 - I_3)n] / I_2 \\
 F_{63} &= -3(I_2 - I_1)n^2 / I_3.
 \end{aligned} \tag{B-1}$$

The elements of the dynamics matrix derived from the quaternion equations of motion (4.19) and used in the quaternion filter in equation (4.54) are

$$\begin{aligned}
 F_{11} &= 0 & F_{21} &= -\frac{1}{2}(\omega_3 + \dot{f}) & F_{31} &= -\frac{1}{2}\omega_1 \\
 F_{12} &= \frac{1}{2}(\omega_3 + \dot{f}) & F_{22} &= 0 & F_{32} &= -\frac{1}{2}\omega_2 \\
 F_{13} &= -\frac{1}{2}\omega_2 & F_{23} &= \frac{1}{2}\omega_1 & F_{33} &= -\frac{1}{2}(\omega_3 + \dot{f}) \\
 F_{14} &= \frac{1}{2}q_4 & F_{24} &= \frac{1}{2}q_3 & F_{34} &= -\frac{1}{2}q_1 \\
 F_{15} &= -\frac{1}{2}q_3 & F_{25} &= \frac{1}{2}q_4 & F_{35} &= -\frac{1}{2}q_2 \\
 F_{16} &= \frac{1}{2}q_2 & F_{26} &= -\frac{1}{2}q_1 & F_{36} &= -\frac{1}{2}q_3
 \end{aligned} \tag{B-2}$$

$$\begin{aligned}
 F_{41} &= -12K_1\Omega^2(2q_1q_2q_3 + q_2^2q_4 - q_3^2q_4) \\
 F_{42} &= -12K_1\Omega^2(2q_1q_2q_4 + q_1^2q_3 - q_3q_4^2) \\
 F_{43} &= -12K_1\Omega^2(-2q_1q_3q_4 + q_1^2q_2 - q_2^2q_4) \\
 F_{44} &= 0 \\
 F_{45} &= K_1\omega_3 - h_w / I_1 \\
 F_{46} &= K_1\omega_2
 \end{aligned}$$

$$\begin{aligned}
 F_{51} &= -6K_2\Omega^2(q_3 - 2q_2^2q_3 - 2q_3^3) \\
 F_{52} &= -6K_2\Omega^2(q_4 - 4q_1q_2q_3 - 6q_2^2q_4 - 2q_3^2q_4) \\
 F_{53} &= -6K_2\Omega^2(q_1 - 4q_2q_3q_4 - 6q_1q_3^2 - 2q_1q_2^2) \\
 F_{54} &= K_2\omega_3 + h_w / I_2 \\
 F_{55} &= 0 \\
 F_{56} &= K_2\omega_1
 \end{aligned}$$

$$\begin{aligned}
 F_{61} &= -6K_3\Omega^2(q_2 - 2q_2q_3^2 - 2q_2^3) \\
 F_{62} &= -6K_3\Omega^2(q_1 - 4q_2q_3q_4 - 6q_1q_2^2 - 2q_1q_3^2) \\
 F_{63} &= -6K_3\Omega^2(-q_4 - 4q_1q_2q_3 + 6q_3^2q_4 + 2q_2^2q_4) \\
 F_{64} &= K_3\omega_2 \\
 F_{65} &= K_3\omega_1 \\
 F_{66} &= 0
 \end{aligned}$$

where  $K_1 = \frac{I_2 - I_3}{I_1}$ ,  $K_2 = \frac{I_3 - I_1}{I_2}$ ,  $K_3 = \frac{I_1 - I_2}{I_3}$ ,

and  $\Omega^2 = \mu / r^3$ .

The non-zero elements of the dynamics matrix derived from the orbit equations of motion (4.1) and used in the navigation filter in equation (4.54) are

$$\begin{aligned}
 F_{14} &= F_{25} = F_{36} = 1 \\
 F_{41} &= -\frac{\mu}{r^3} \left[ 1 - \frac{3}{2} J_2 \left( \frac{R_e}{r} \right)^2 \left( \frac{5z^2}{r^2} - 1 \right) \right] + \frac{3\mu x^2}{r^5} \left[ 1 - \frac{5}{2} J_2 \left( \frac{R_e}{r} \right)^2 \left( \frac{7z^2}{r^2} - 1 \right) \right] \\
 F_{42} &= \frac{3\mu xy}{r^5} \left[ 1 - \frac{5}{2} J_2 \left( \frac{R_e}{r} \right)^2 \left( \frac{7z^2}{r^2} - 1 \right) \right] \\
 F_{43} &= \frac{3\mu xz}{r^5} \left[ 1 - \frac{5}{2} J_2 \left( \frac{R_e}{r} \right)^2 \left( \frac{7z^2}{r^2} - 3 \right) \right]
 \end{aligned} \tag{B-3}$$

$$\begin{aligned}
 F_{51} &= \frac{3\mu xy}{r^5} \left[ 1 - \frac{5}{2} J_2 \left( \frac{R_e}{r} \right)^2 \left( \frac{7z^2}{r^2} - 1 \right) \right] \\
 F_{52} &= -\frac{\mu}{r^3} \left[ 1 - \frac{3}{2} J_2 \left( \frac{R_e}{r} \right)^2 \left( \frac{5z^2}{r^2} - 1 \right) \right] + \frac{3\mu y^2}{r^5} \left[ 1 - \frac{5}{2} J_2 \left( \frac{R_e}{r} \right)^2 \left( \frac{7z^2}{r^2} - 1 \right) \right] \\
 F_{53} &= \frac{3\mu yz}{r^5} \left[ 1 - \frac{5}{2} J_2 \left( \frac{R_e}{r} \right)^2 \left( \frac{7z^2}{r^2} - 3 \right) \right] \\
 F_{61} &= \frac{3\mu xz}{r^5} \left[ 1 - \frac{5}{2} J_2 \left( \frac{R_e}{r} \right)^2 \left( \frac{7z^2}{r^2} - 3 \right) \right] \\
 F_{62} &= \frac{3\mu yz}{r^5} \left[ 1 - \frac{5}{2} J_2 \left( \frac{R_e}{r} \right)^2 \left( \frac{7z^2}{r^2} - 3 \right) \right] \\
 F_{63} &= -\frac{\mu}{r^3} \left[ 1 - \frac{3}{2} J_2 \left( \frac{R_e}{r} \right)^2 \left( \frac{5z^2}{r^2} - 3 \right) \right] + \frac{3\mu z^2}{r^5} \left[ 1 - \frac{5}{2} J_2 \left( \frac{R_e}{r} \right)^2 \left( \frac{7z^2}{r^2} - 5 \right) \right].
 \end{aligned}$$

The wooden pallets were used for tests where antenna location and orientation had to be maintained precisely from one day to the next. Two wooden pallets were placed approximately 3 m apart on the flat roof of a low building at Table Mountain. This eliminated any structural flexure that may have been present in the other test structures. The master antenna was mounted to one of the pallets with C-clamps, and two slave antennas were mounted to the other pallet. Figure 5.7 shows the pallet configuration at Table Mountain.

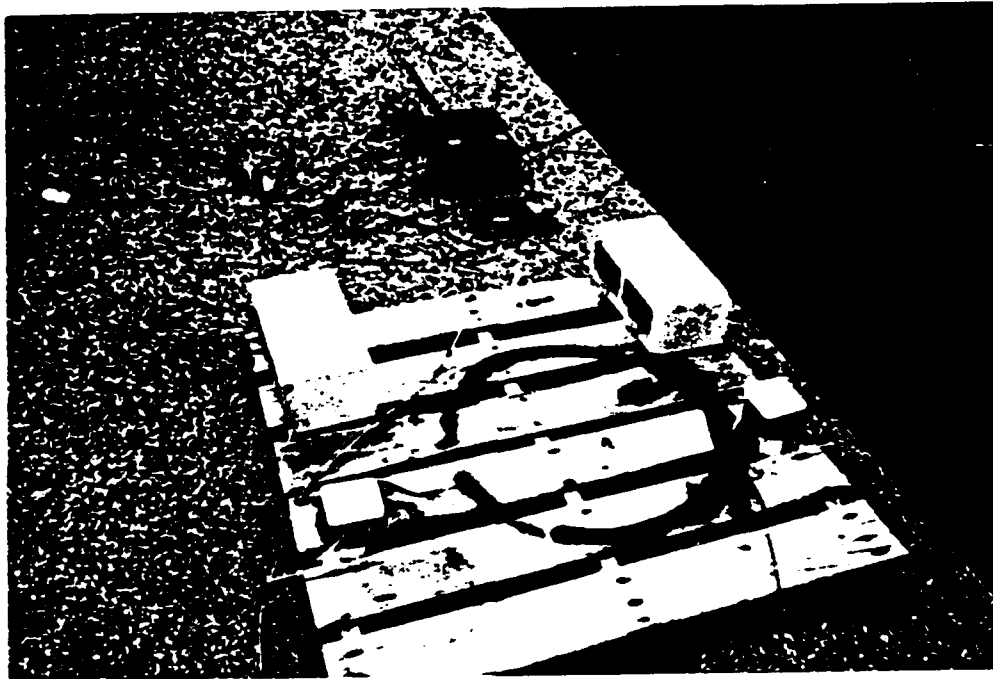


**Fig. 5.7 Wooden Pallet Structure**

The one-armed spinner structure was designed to mount on an existing spinning platform. The structure consists of a single master-slave antenna pair mounted on a PVC center pipe and a single 1 meter long PVC pipe arm. The arm was fitted to a cylinder mounted on the spin table. The table is driven by a DC motor which has a variable power supply that can be used to regulate spin rate. The receiver, power supply, and data collection computer are all stored inside the cylinder during testing. The configuration is shown in Figure 5.6.

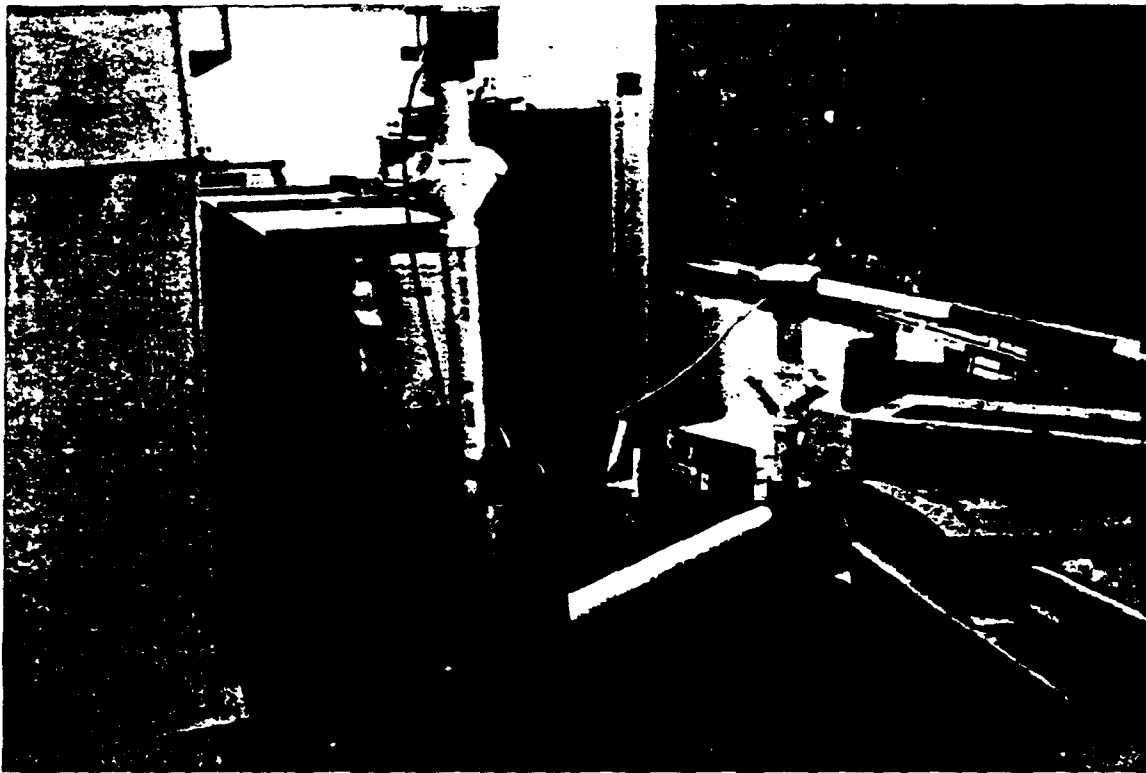


**Fig. 5.6 One-Armed Spinner Structure**

### **5.5 Ground Testing Configuration**

Ground testing of the Trimble Vector receiver was conducted under both static and dynamic (spinning) conditions. The tests focused on measurement quality, static self survey, static attitude solution accuracy, and dynamic performance on a spinning platform. Before addressing the specific experiments, the test beds will be described. Each test bed consisted of a site, an antenna platform, and known reference points to verify accuracy.

#### **Test locations**

Two locations were used for ground testing --the roof of the Engineering Center, and Table Mountain. The roof of the Engineering Center at the University of Colorado consists of a flat area approximately 60 x 100 m (see Figure 5.4). The view of the sky is partially obstructed to the southwest by the tower of the Engineering Center and adjacent buildings. Many antennas and metal structures are co-located on the roof, making it a very noisy environment for multipath. (However, it was quite convenient.)

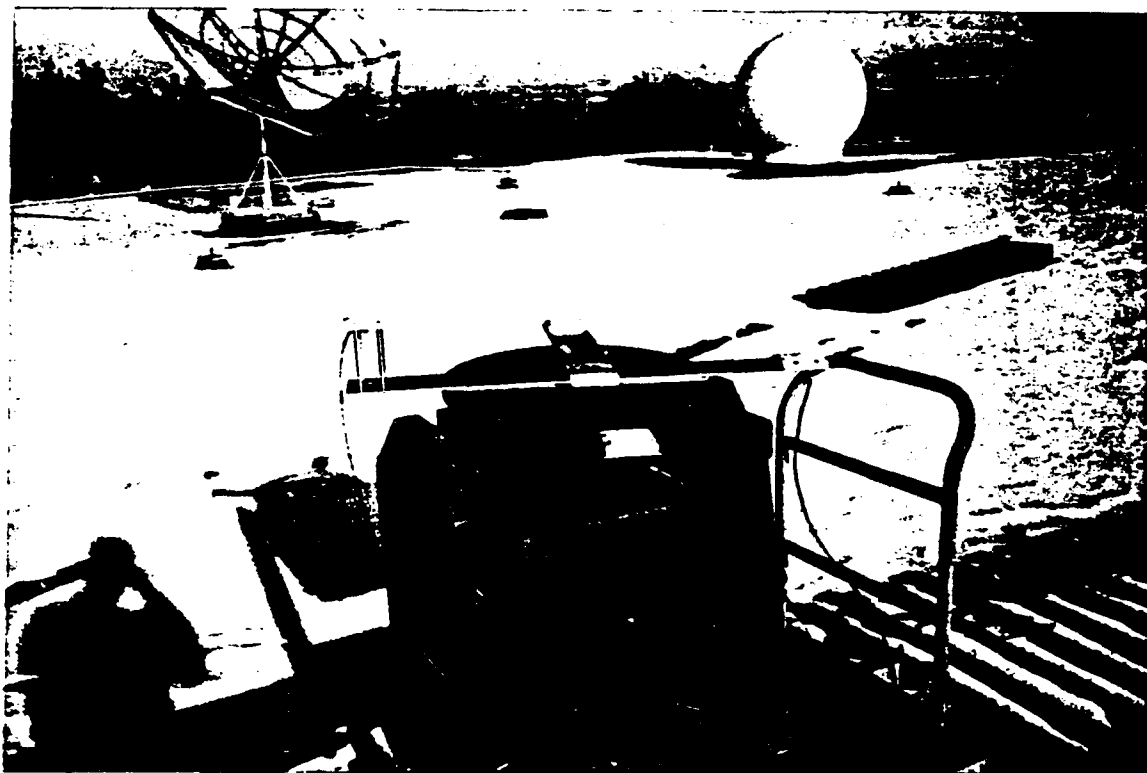


**Fig. 5.4. Engineering Center Roof and x Structure**

The other test location used was Table Mountain, shown in Figure 5.5. Table Mountain is a large flat mesa north of Boulder, Colorado, controlled by the U.S. Department of Commerce. The area used was largely free of multipath reflectors and contained surveyed reference points.

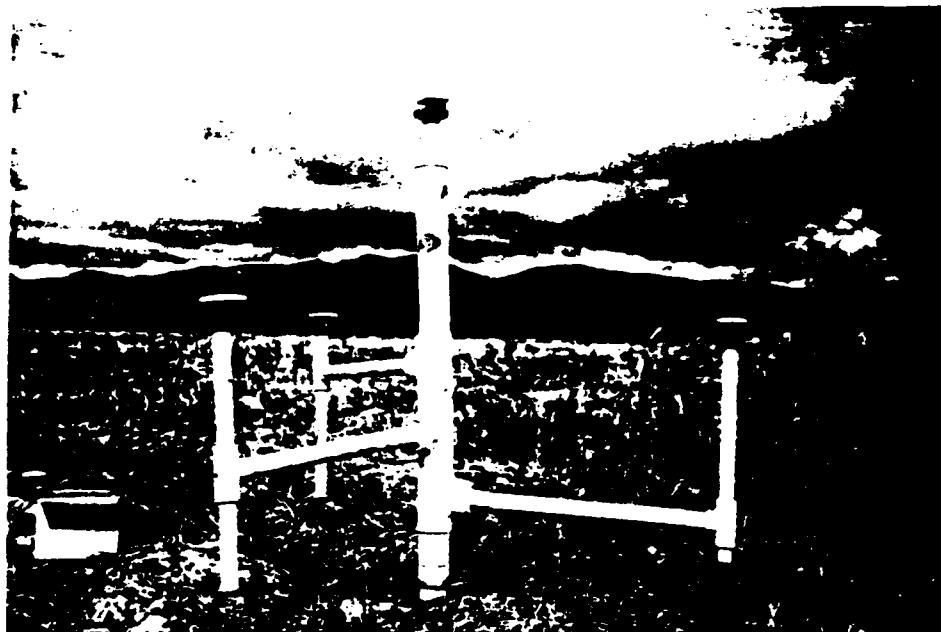


Fig. 5.5 Table Mountain Site and Tree Structure

#### **Antenna Platforms**

Four antenna platforms were used for receiver testing. Each platform was tailored for a particular purpose in the testing program. The platforms will be referred to as the x structure, the tree structure, the one-armed spinner, and the wooden pallets.

The x structure is constructed from two aluminum cross members, each 1-m long as shown in Figure 5.4. The master antenna is raised on spacers that are approximately 10 cm long to prevent all four antennas from being coplanar. A small diode laser can be mounted at the center of the two cross members for absolute accuracy tests. The x structure was used in early tests, but it suffered from several shortcomings --the baselines were too short; the antennas were too close to coplanar; the arms were too flexible; and the structure itself was a multipath reflector.

The tree structure shown in Figure 5.5 was designed to address the problems with the x structure. It has a center mounting pole for the master antenna and three one-meter arms for the slave antennas. The center pole and baseline 2 define the body coordinate system. The arms can be moved to change the relative height and orientation of the slave antennas. The structure is fabricated using Schedule 40 PVC pipe. This material was chosen because it was thought to have several advantages [Comp, et al., 1993] -- greater rigidity, preventing significant flexure during the tests; lighter weight, permitting easy relocation and storage; and transparency to L-band GPS signals. The small diode laser was mounted below the baseline 2 antenna for absolute accuracy tests. Note that the three antenna baselines shown in the photograph are nearly orthogonal with the master antenna at the vertex of the orthogonal set. This nearly orthogonal configuration provides the best sensitivity to changes in attitude for all three axes. Field experience showed that the tree structure was not as rigid as originally hoped, thus suggesting the area of attitude determination for non-rigid structures as an area for future research.